Dual Polarized And Balanced Receivers At Millimeter And Submillimeter Wavelengths

Thesis by

Goutam Chattopadhyay

In Partial Fulfillment of the Requirements

for the Degree of

Doctor of Philosophy

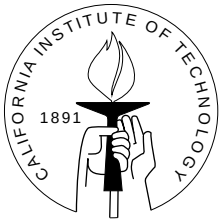

California Institute of Technology

Pasadena, California

2000

(Submitted September 17, 1999)

This thesis is dedicated to my parents.

Acknowledgments

First and foremost, I would like to express my heartiest thanks and sincere gratitude to my advisor, Jonas Zmuidzinas, for his guidance, support, encouragement, and patience. Jonas is a great scientist, the best I have ever met, and he is a wonderful person too. I feel both honored and privileged to have been his student.

I would also like to thank John E. Carlstrom, who urged me to come to Caltech in the first place. John was my advisor for the first two years of my stay here at Caltech before he left for Chicago, and I would always remain grateful to him for his support and encouragement.

I am grateful to Rick LeDuc of JPL for fabricating all the complicated yet wonderful SIS devices. Rick makes the best SIS devices and the results in this thesis will prove that.

It is with great pleasure that I thank the members of the millimeter and submillimeter group. I am grateful to David Miller for his help with the antenna beam pattern measurements. His knowledge and expertise in IF electronics, data acquisition systems, and mechanical designs were of great help to me in this endeavor. I also thank Jacob Kooi for all the stimulating discussions on SIS mixers, LNA designs, scalar model measurements, stability analysis, and much more. If I ever needed any components or any other help, I knew that I could always count on Jacob. Special thanks to my office mate Frank Rice for helping me with the SuperMix simulations and for all the discussions on a wide variety of topics. Frank was a great office mate and I will always cherish the memories of my association with him. I am indebted to our computer "guru" John Ward who kept the computers and the networks up and running, so that I could spend hours reading news from dozens of web-sites, follow cricket scores and soccer results, and occasionally do some simulations. I am also thankful to Jonathan

Kawamura and Jian Chen for their helpful discussions and suggestions. I wish to thank Ricardo Paniagua of the physics workshop for machining the parts and various other components that I needed. Sincere thanks to Susan McCurdy, Linda Dozsa, and Rena Becerra-Rasti for their help and support.

It has been a great pleasure to work on the Bolocam and the Polatron project with Jason Glenn, Byron Philhour, and Andrew Lange. I thank them for giving me the opportunity to work on those projects which helped me learn the HFSS simulation package in further detail. I would also like to thank Todd Gaier of JPL for allowing me to use his network analyzer. I wish to thank John Yamasaki of the astronomy department for making my stay memorable during my days in the Robinson building. Special thanks go to my "Red Door friends" – Sandeep Sane and Sujoy Mukhopadhyay, who showed up almost everyday at 3:00 PM at the Red Door Cafe to talk about anything and everything over a cup of coffee, from politics and sports to scientific and not so scientific topics, in the quest to save the planet earth! I am also grateful to all those who took the occasional break from their laboratory to join me in playing cricket, soccer, tennis, racket ball, and badminton.

Finally, I thank my parents, my brother and sisters, for always being there. For their love and encouragement I will always be grateful. And above all, I would like to thank my wife – my best friend, Sulekha Chattopadhyay, who has been a constant source of strength and inspiration, and without whom I would have lost my way.

Dual Polarized and Balanced Receivers At Millimeter and Submillimeter Wavelengths

Abstract

Dramatic advances in millimeter and submillimeter wave receivers in recent years have resulted from the development of superconductor insulator superconductor (SIS) mixers, which now offer unsurpassed performance from 70 GHz to 1 THz. To increase the sensitivity of the receivers further at these frequencies, one needs to use dual-polarized and balanced receivers. When both the polarizations are received simultaneously, there is a $\sqrt{2}$ improvement in the signal to noise ratio (SNR). Balanced mixers improve the sensitivity of receivers by suppressing local oscillator (LO) amplitude modulation (AM) noise and rejecting LO thermal noise. This thesis describes the design, fabrication and performance of mixers and components for low noise dual-polarized and balanced receivers at millimeter and submillimeter wavelengths both in quasi-optical and waveguide configurations. The quasi-optical receiver utilizes a novel cross-slot antenna on a silicon hyperhemispherical lens, two junction tuning circuits, niobium trilayer junctions, and an IF circuit containing a lumped element 180° hybrid. The antenna has four feed points, two for each polarization; and each feed point is coupled to a two-junction SIS mixer. For dual polarization operation, the mixer is mounted in such a way that a single LO can pump the junctions for both the polarizations. For the balanced receiver, the LO and the RF signals are coupled to the mixer in orthogonal polarizations using a wire-grid polarizer. For waveguide dual polarization receivers, a moderately broadband septum ortho-mode transducer (OMT) is designed and experimental results are presented at millimeter wavelengths. Broadband finline OMTs are investigated for possible use at millimeter wavelengths, and experimental results of a finline OMT is presented at X-band.

Contents

List of Figures

List of Tables

Chapter 1

Introduction

Millimeter and submillimeter wave systems are becoming increasingly important in many scientific applications like radio astronomy, remote sensing, plasma diagnostics, radar, and communication systems. In fact, submillimeter wave band (300 GHz – 3000 GHz) region of the electromagnetic spectrum remains one of the newest and least explored areas of astronomy today.

Traditionally, commercial applications have accounted for only a very small fraction of millimeter and submillimeter wave (30 GHz – 3000 GHz) market. Over the past few years, however, this has changed with emerging applications in cellular communications, interactive multimedia networks, intelligent vehicle highway systems with collision avoidance radars, passive millimeter wave imaging for aircraft landing, and commercial and military radar systems [1], [2].

Millimeter and submillimeter waves have significant advantages over microwave and infrared frequencies. One is the size advantage: shorter wavelengths compared to microwave allow smaller structures and antennas, thus allowing fabrication of millimeter and submillimeter wave systems using integrated circuit techniques. Higher antenna gain (narrow beamwidth) for a given aperture size at these frequencies is an added advantage, since antenna gain scales in proportion to the operating frequency squared. Larger bandwidths, higher resolution, and low attenuation in some bands are also the advantages over microwave systems which make them traditionally attractive for military and scientific applications like remote sensing and imaging. Millimeter waves can penetrate many atmospheric conditions like fog, smoke, and dust which are opaque to infrared and optical wavelengths. This property of millimeter waves makes it attractive for high resolution sensors operating in reduced visibility conditions.

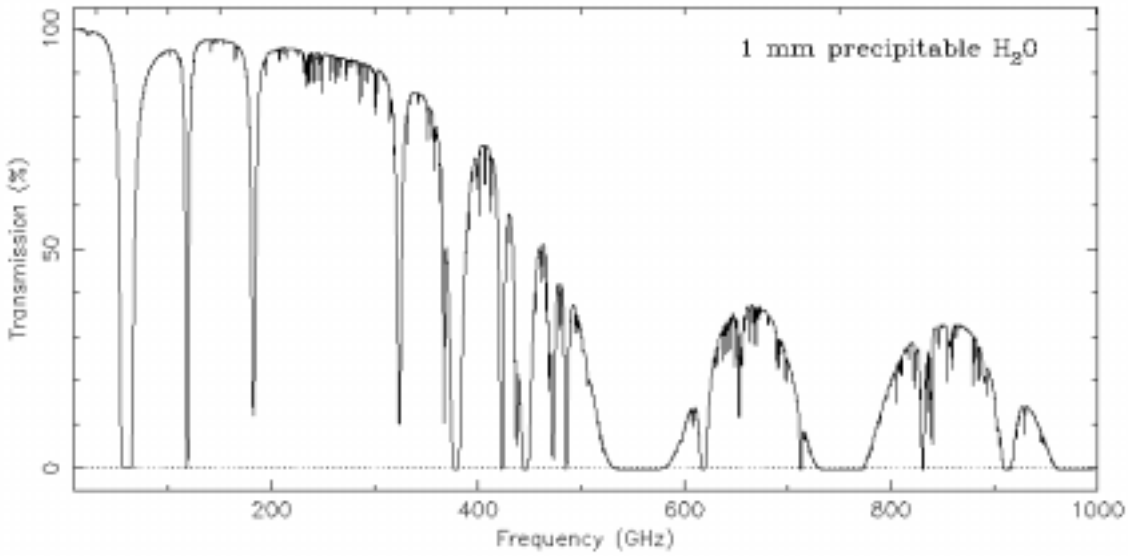

Figure 1.1 Model of the zenith atmospheric transmission on Mauna Kea, site of Caltech Submillimeter Observatory (CSO), at an altitude of 4200 m for the case of 1 mm of precipitable H_2O.

Millimeter and submillimeter waves do have their limitations. Compared to microwave systems, millimeter and submillimeter wavelengths have greater atmospheric opacity limiting their range of operation; for instance, ground based astronomical observations can only be carried out in windows defined by the atmospheric transmission, as shown in Figure 1.1. Millimeter and submillimeter waves are attenuated by significant levels of precipitation, have higher scattering losses, and are absorbed in the atmosphere by water vapor and oxygen. Other drawbacks have been the relatively high cost of millimeter and submillimeter wave technology and the lack of reliable, high power solid-state local oscillator sources at these frequencies. Although electron tube sources and far-infrared lasers can provide ample RF power in this frequency range, size, power requirements, lack of tuning capability and difficulty in maintenance have limited their usefulness and make them unsuitable for many applications. The alternative is to use a solid-state source in conjunction with multipliers. The poor efficiencies of present day multipliers, coupled with their small size, results in solid-state sources having relatively low output power. However, considerable research and development has resulted in significant improvements in these areas. Despite all

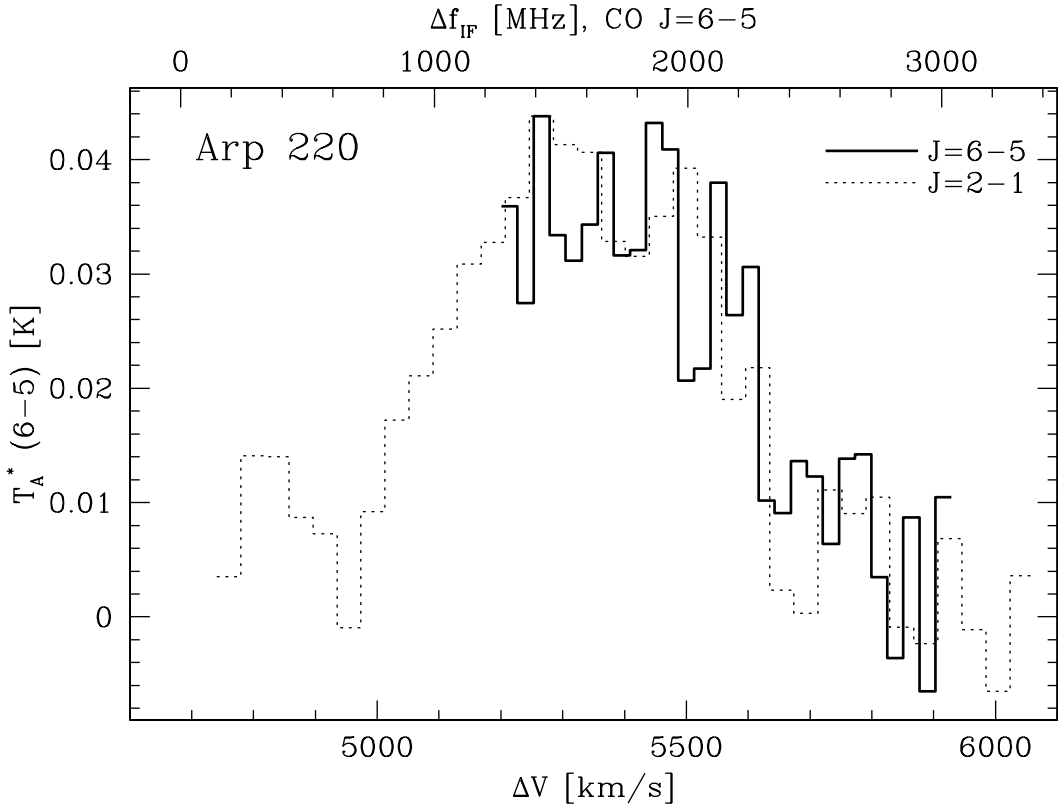

Figure 1.2 Spectrum of Arp 220 at 690 GHz in the CO $J = 6 \rightarrow 5$ and $J = 2 \rightarrow 1$ transitions. Both spectra were obtained at the CSO in May 1998, using a wideband analog correlation spectrometer. The 6–5 data were taken using a twin-slot 690 GHz SIS receiver with a 2 GHz IF bandwidth. (Ward, Harris, Zmuidzinas 1999)

these disadvantages, millimeter and submillimeter waves represent an excellent compromise between the performance characteristics of the microwaves and the small, compact size, short range, high resolution, high bandwidths of infrared and optical wavelengths.

1.1 Millimeter and Submillimeter Wave Astronomy

The submillimeter band recently has gained widespread attention in the astronomical community [3]. Spectroscopy at millimeter through far-infrared wavelengths promises

to become an essential tool for unraveling the redshift distribution and physical nature of submillimeter objects. The millimeter and submillimeter bands contain spectral and spatial information on the cosmic background radiation, on very distant newly formed galaxies, and on the early stages of star formation in gas clouds within our own galaxy. One can immediately see the importance of the submillimeter band to star-formation studies by noting that the temperatures of the dense interstellar gas range from about 10 K in the cooler regions to 100 or 200 K in the hotter and usually denser parts. The corresponding frequencies ($h\nu \sim kT$) range from about 200 GHz to 4 THz. This same range corresponds to many interesting molecular rotation and atomic fine-structure transitions. Figure 1.2 shows one such spectrum of the ultra-luminous infrared galaxy Arp 220 at 690 GHz in the CO $J = 6 \rightarrow 5$ and $J = 2 \rightarrow 1$ transitions.

The quest for higher angular resolution and increased sensitivity at millimeter and submillimeter wavelengths has led to larger telescopes and interferometric arrays for radio astronomy purposes. The 45 m telescope of the Nobeyama Radio Observatory and the 30 m telescope of the Institut de Radioastronomie Millimétrique (IRAM) are currently the largest operating filled aperture telescopes dedicated for millimeter-wave astronomy. The Large Millimeter Telescope (LMT) – a 50 m diameter telescope, is being built jointly by the University of Massachusetts and Mexico. Telescopes with more accurate surfaces and located at higher altitudes have been built specifically for submillimeter-wave observations. Examples include the 15 m James Clerk Maxwell Telescope (JCMT) and the 10.4 m Caltech Submillimeter Observatory (CSO) telescopes, both located near the 4200 m summit of Mauna Kea and also the 10 m Submillimeter Telescope Observatory (HHT/SMTO) located at 3200 m on Mt Graham, Arizona. The construction of a 2.5 m airborne telescope – the Stratospheric Observatory for Infrared Astronomy (SOFIA), which will be placed on a Boeing 747–SP aircraft, is well under way, and will allow observations beyond the 1 THz limit for ground-based observations imposed by the atmospheric transmission. ESA and NASA are jointly working on a 3.5 m Far Infra-Red Space Telescope (FIRST) for

launch in 2007.

Interferometry is needed to obtain higher angular resolution, and there are several operational millimeter-wave interferometers: the Owens Valley Radio Observatory (OVRO), the Berkeley-Illinois-Maryland-Association mm-array, the Nobeyama mm-array (NMA), and the IRAM mm-array. The CSO and JCMT telescopes are used periodically as a submillimeter-wave interferometer. Quite a few other arrays are also being built at millimeter and submillimeter wavelengths: the Smithsonian Astrophysical Observatory's six-element (6 m diameter each) Submillimeter-wave Array (SMA). The most ambitious ground-based project is the Atacama Large Millimeter Array (ALMA) – a joint U.S./European project to build a 64-element array of 12 m telescopes in Chile. The design goals of these arrays specify angular resolutions as high as $0.1''$.

1.2 Receivers at Millimeter and Submillimeter Wavelengths

Coherent detection techniques (heterodyne receivers) are used almost exclusively at centimeter and longer wavelengths, while direct detection predominates in the optical and infrared bands. The millimeter, submillimeter, and far–infrared bands represent a transition region from coherent to direct detection. Coherent detection refers to the radio technique of amplifying, down-converting, and filtering a signal prior to detection. Both heterodyne and incoherent detection techniques are used at millimeter and submillimeter wavelengths. Coherent systems offer essentially unlimited spectral resolution, but only over small bandwidths ($\sim$ 4 GHz). The spectral resolution of incoherent detection, using cooled bolometers, is set by the optics and filters preceding the detector. Incoherent detection is the obvious choice for broadband continuum radiation.

A simplified block diagram of millimeter and submillimeter wave heterodyne receiver

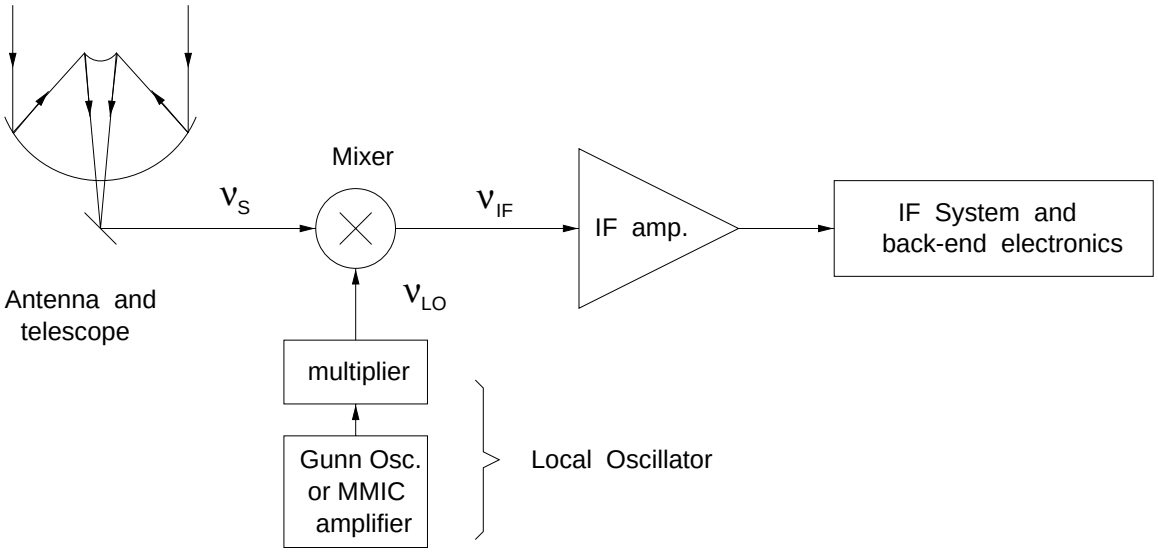

Figure 1.3 A block diagram of millimeter and submillimeter heterodyne receiver systems. At the low frequency end of the millimeter waves, the first component is a low–noise amplifier, followed by a mixer. At submillimeter wavelengths, low–noise amplifiers are not yet available. The signal from a telescope at a frequency ν_S is combined with a local oscillator at frequency ν_{LO} in a "mixer," which is a nonlinear device, to yield the difference or "intermediate" frequency $\nu_{IF} = |\nu_S - \nu_{LO}|$, which is then amplified and spectrally analyzed.

systems is shown in Figure 1.3. In such a system, frequency down-conversion is the first operation performed on the signal. This is the only viable possibility for submillimeter wavelengths since low–noise amplifiers (LNA) are not yet available. At millimeter wavelengths where LNAs are available, or slowly becoming available, the incoming radiation is first amplified by the LNA, and then the frequency down-conversion is performed. The principal components for such a heterodyne system are the local oscillator, the LNA, the mixer, the intermediate–frequency (IF) amplifier, and the back-end electronics. All of these components are undergoing intensive development and are improving very rapidly. In particular, there has been a tremendous (nearly two orders of magnitude) improvement in the sensitivity of submillimeter mixers over the past decade [4].

1.2.1 Waveguide Receivers

Traditionally millimeter wave receivers are implemented in waveguide mounts with scalar feed horns, which provide very high quality Gaussian beam patterns and high efficiencies, resulting in good coupling and low spillovers. Tunerless mixers in waveguide mounts result in very sensitive receivers in millimeter and the lower end of submillimeter frequencies. However, waveguide mixers become increasingly difficult and expensive to construct at higher frequencies because the critical dimensions scale with the wavelength, and the tolerances become very important. The waveguide block becomes harder to machine and the mixer elements become more difficult to fabricate. However, these difficulties are practical, and not fundamental. For instance, a 2.5 THz corrugated horn has been fabricated recently by using vacuum sputter deposition (instead of electroforming) on a conventionally machined mandrel [5], [6]. Over the past few years, some other low cost techniques have been developed for fabricating waveguide components at millimeter and submillimeter wavelengths, such as direct high-speed machining [7], laser silicon micromachining which uses lithography and anisotropic etching to create three-dimensional micron-scale structures [8], and mastering, moulding, and casting techniques [9].

Both Schottky-diode mixers and superconductor insulator superconductor (SIS) mixers are used at millimeter and submillimeter wave waveguide receivers. Below 700 GHz, SIS receivers are typically 5 – 10 times more sensitive than their Schottky-diode counterparts, and thus, SIS waveguide receivers are preferred for most radio astronomy applications at millimeter and submillimeter wavelengths. However, Schottky-diode receivers have some advantages. They can operate over a very wide temperature range, including room temperature, and can therefore be used in applications in which cryogenic cooling is undesirable or prohibitively expensive; thus Schottky-diode mixers are still favored in non-astronomy applications at millimeter wavelengths. Low-noise SIS waveguide mixers have been designed and built at frequencies up to 850 GHz [10] and beyond [11], and as the new technologies for fabricating waveguide components at terahertz frequencies mature, waveguide SIS mixers

at these frequencies will become more common.

1.2.2 Quasi-Optical Receivers

The loss encountered in waveguide structures at millimeter and submillimeter wavelengths has provided the incentive for the design of quasi-optical systems at these frequencies. An exact analysis of the propagation of radiation through the apertures, focusing optics, and other optical devices of quasi-optical systems of finite diameter requires a detailed solution of the electromagnetic diffraction problem. However, the assumption that the transverse amplitude and phase distribution of the propagating beam of electromagnetic radiation possesses circular symmetry and can be defined in terms of an orthogonal set of basis functions, termed "Gaussian modes," which are the product of a polynomial term, a Gaussian transverse amplitude variation and a phase factor provides a useful design technique for the development of quasi-optical systems [12].

Quasi-optical mixers rely on the fact that two-dimensional microstructures are easily fabricated using conventional lithography. In this approach the mixer element is fabricated integrally with a planar antenna and a substrate lens is used to increase the directivity of the planar antenna [13]. Quasi-optical mixers are much simpler to fabricate than either conventional or micromachined waveguide mixers.

The main challenge in constructing low-noise quasi-optical receivers at millimeter and submillimeter wavelengths is to obtain efficient radiation coupling. The planar antenna design and the particular choice of the planar antenna type is very critical in the success of a quasi-optical receiver. The planar antenna should have low sidelobes, a symmetric main beam, and low phase aberrations. The coupling efficiency to a fundamental Gaussian mode is a good test of these characteristics and indicates the quality of the planar antenna and the optics. There is no fundamental reason that planar antennas can not have a high efficiency; in fact, detailed calculations predict efficiencies around 90% for twin-slot antennas on antireflection-coated silicon

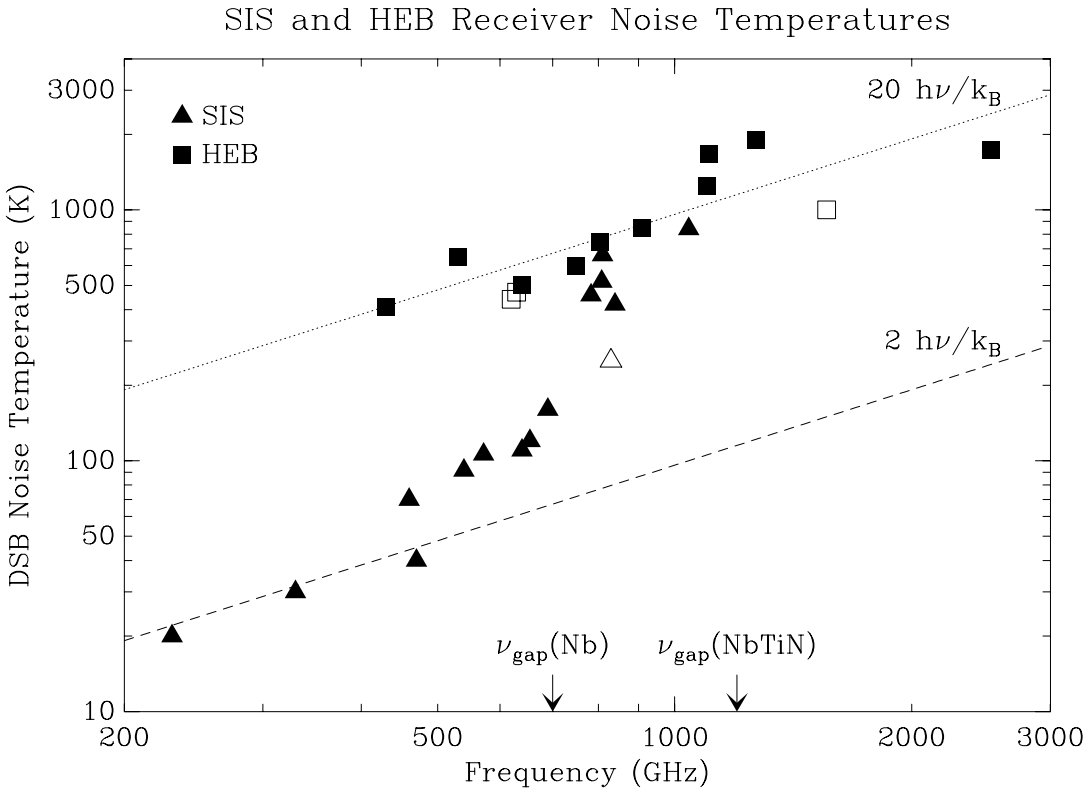

Figure 1.4 Selected noise temperatures obtained by various groups with superconductor insulator superconductor (SIS) and hot electron bolometer (HEB) receivers. The open triangle near 830 GHz is the recent SIS result using NbTiN; it is nearly a factor of two improvement over previous results.

lenses [14].

At millimeter and submillimeter wavelengths, Schottky-diode, superconductor insulator superconductor (SIS), and hot electron bolometers (HEB) are used as mixing elements in quasi-optical configuration. Quasi-optical SIS mixers are most sensitive below 1 THz, and HEB mixers [15] are favored above the gap frequency of niobium. Figure 1.4 shows the current status of SIS and HEB mixer performances. Though Schottky-diode quasi-optical mixers are not as sensitive as SIS and HEB mixers, they have a few advantages, as discussed in section 1.2.1.

1.3 SIS Receivers

The first descriptions of mixing on a superconducting tunnel diode called superconductor insulator superconductor (SIS) were published about twenty years ago [16], [17]. A comprehensive theoretical investigation of the SIS, at about the same time, made clear that SIS's respond to photons at millimeter and submillimeter wavelengths [18]. The SIS has become the receiver of choice for millimeter and submillimeter radio astronomy. The key reason for their excellent performance is the sharpness and strength of the nonlinearities in superconducting tunnel junctions, which allow efficient and low-noise frequency conversion. Since superconductor can have very low loss at millimeter and submillimeter wavelengths, it is possible to construct efficient tuning circuits and antennas which are integrated with the devices. Moreover, SIS mixers require local oscillator signals which are much lower than the Schottky-diode mixers.

The development of fabrication techniques for producing small area, high current density niobium superconductor insulator superconductor (SIS) tunnel junctions integrated with thin-film microstrip tuning circuits has resulted in dramatic improvement in the sensitivity of heterodyne receivers in the 100-1000 GHz range [4]. In principle, the sensitivity of SIS mixers is limited only by the zero-point quantum fluctuations of the electromagnetic field. In terms of the single-sideband (SSB) noise temperature, this limit is $h\nu/k_{\mathrm{B}} \approx 0.05$ K/GHz. In practice, the SSB noise temperatures of the best SIS receivers now fall below 0.5 K/GHz over the 100-700 GHz band, dropping as low as 0.2 K/GHz in some cases.

The noise of these sensitive receivers is actually often dominated by other factors such as optical losses, thermal noise introduced along with the local oscillator, and IF amplifier noise, rather than by the noise in the SIS mixer itself. The progress in SIS mixers is largely the result of the development of robust, small area, high quality Nb/Al-Oxide/Nb junctions integrated with low loss Nb thin-film tuning circuitry. These junctions have been used in both waveguide and quasi-optical circuits.

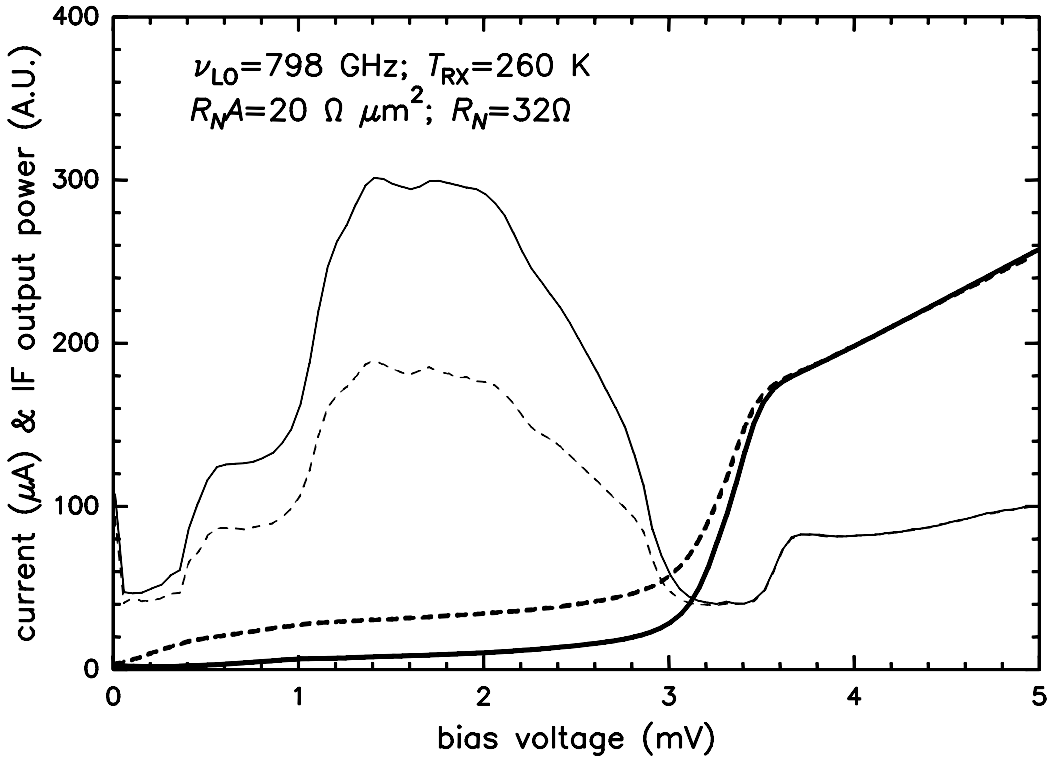

Figure 1.5 Results for an 800 GHz SIS mixer using NbTiN ground planes and wiring layers, and Nb/AlN/NbTiN junctions. The noise temperature is 260 K (DSB), with no corrections applied.

The situation changes dramatically above 700 GHz, the gap frequency of niobium, at which point the niobium tuning circuits become very lossy since the photon energy is large enough to break Cooper pairs ($h\nu > 2\Delta$). At these frequencies, the performance is limited by the circuit losses, even when high conductivity normal metals such as aluminum are used for tuning in place of niobium [19], [20]. Recent advances in developing SIS mixers with tuning circuits made with superconducting NbTiN films show great promise for frequencies above 700 GHz [21]. The gap energy of NbTiN is larger than that of niobium by a factor of about 1.7, and appears to be a very promising low-loss material for SIS circuits at frequencies up to 1.2 THz. Figure 1.5 shows the recent results for an 800 GHz mixer, which achieved a noise temperature of 260 K (DSB), which is nearly a factor of two lower noise than previous mixers [22].

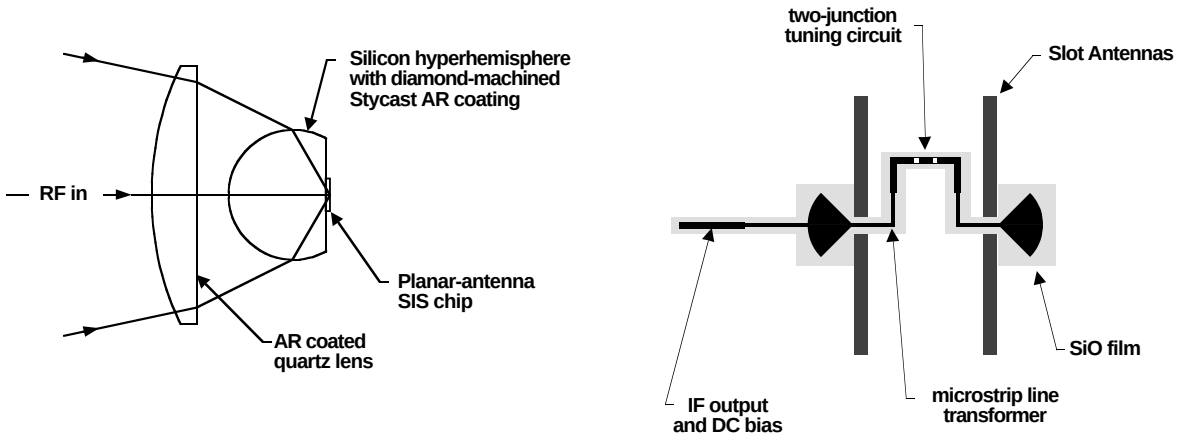

Figure 1.6 Twin-slot mixer design. **Left**: the optical configuration uses an antireflection-coated hyperhemispherical silicon lens to focus radiation onto the SIS chip; **Right**: the SIS chip consists of a twin-slot antenna, a microstrip transformer, and a tuning circuit which uses two SIS junctions.

1.3.1 Single Polarized SIS Receivers

Quasi-optical SIS mixers with a twin-slot antenna on a hyperhemispherical substrate lens have been shown to be very successful for single-polarized receivers in millimeter and submillimeter wavelengths [23], [24], [25]. The main virtues of the slot antenna are that it radiates $\sim \epsilon_r/(1+\epsilon_r)$ of its power into the dielectric lens and therefore does not need a backing cavity when placed on high dielectric constant substrates. Furthermore, the ground-plane of the slot antenna isolates the back-side of the wafer and allows easy integration of active devices [26].

The twin-slot antenna on a hyperhemispherical lens has good efficiency, linear polarization, low impedance, and symmetric beam pattern. Kerr *et al.* first proposed the use of a twin-slot antenna for a 100 GHz mixer, using whisker-contacted Schottky-diodes with the two-slots fed in series [27]. This particular design did not use the hyperhemispherical lens. The twin-slot antenna properties are well known from Fourier domain Galerkin moment-method solutions [23], [26], which can account for the mutual interaction of the two slots.

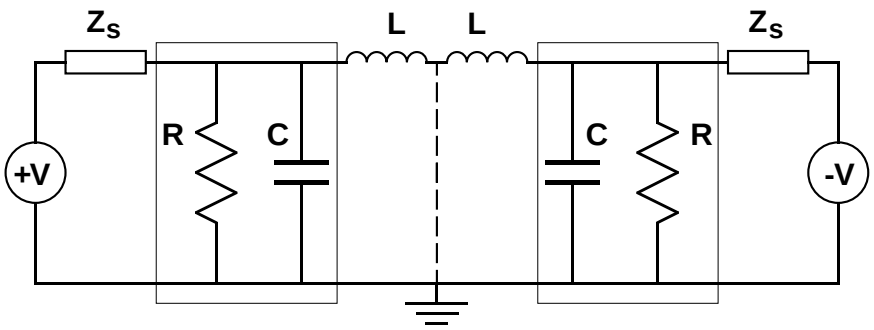

Figure 1.7 The equivalent circuit of the SIS mixer connected with the twin-slot antenna. The junctions can be idealized as simple parallel RC circuits. The physical spacing between the junctions determines the effective tuning inductance L. The slot antennas and microstrip transformers can be considered to be generators with complex source impedance Z_s; the two generators are 180° out of phase due to the symmetry of the circuit.

Figure 1.6 shows the details of a twin-slot SIS mixer with two-junction tuning circuits [28]. Also shown in the figure is the optical configuration with antireflection-coated silicon hyperhemispherical lens to focus the radiation onto the SIS junctions. The radiation received by the slots is coupled to the SIS junctions with superconducting microstrip lines. A two-junction tuning circuit, where the junction *separation* dictates the tuning inductance, is employed to tune out the SIS junction capacitance. The operation of this circuit is shown schematically in Figure 1.7. The symmetry of the circuit produces a virtual ground at the midpoint of the circuit; therefore, the short section of microstrip which connects the two junctions behaves as two inductive shunts which cancel the junction capacitance. The single-polarized 800 GHz quasi-optical SIS receiver, whose performance details are shown in Figure 1.5, employed a similar twin-slot design approach.

1.4 Dual Polarized SIS Receivers

Single-polarized receivers based on SIS tunnel junction mixers are currently the most sensitive receivers available in millimeter and submillimeter wavelengths, and are fast approaching towards the quantum-limit. One way to increase the sensitivity of

SIS receivers further is to use a dual-polarized receiver. When both polarizations are received simultaneously, there is a $\sqrt{2}$ improvement in signal to noise (S/N), or a factor of two reduction in observing time on a telescope for radio astronomy receivers. Also, one cannot improve the sensitivity by making lower-noise receivers if the sensitivity is already limited by atmospheric noise. This is now becoming the situation at the submillimeter wavelengths. The atmospheric transmission on a good night at the CSO is about 50% in the 600–700 GHz window, as can be seen from Figure 1.1, which contributes about 150 K of background noise. In this circumstances, to increase the sensitivity of ground-based radio astronomy receivers, one needs to build dual-polarized and/or side-band separation mixers. Dual polarization operation can be achieved either by quasi-optical means or by using waveguide components. At millimeter wavelengths, waveguide-based dual-polarized mixers are viable; however, at submillimeter wavelengths, quasi-optical designs are more practical.

1.4.1 Quasi-Optical Dual Polarized SIS Receivers

Quasi-optical dual polarization operation can be achieved by using a wire grid polarizer to split the telescope beam into two polarizations. The local oscillator (LO) can be injected using a beamsplitter, either after the polarizer, in which case two beamsplitters are necessary; or before the polarizer, necessitating a single, correctly oriented beamsplitter. Either approach tends to lead to fairly complicated optical designs, especially for receivers with multiple bands, or multiple spatial pixels. A much more elegant and compact solution is to directly construct a dual-polarization mixer. This is reasonably straightforward for quasi-optical designs, since the receiving antenna is lithographically fabricated, and can be designed to receive both polarizations simultaneously. The slot-ring mixer is one such example where a single annular (circular or square-shaped) slot is used, which is fed at two points which are 90° apart, and which has been shown to provide good results at 94 GHz [29]. A slot-ring antenna could easily be adapted for use in a SIS mixer. One drawback for this antenna is that it has a broader radiation pattern (in angle) than the twin-slot an-

tenna [23]. This is simply due to the fact that at any given frequency, the transverse dimensions of a slot-ring are smaller than those of a twin-slot. This broader pattern of the slot-ring will be somewhat more difficult to couple to, so the efficiency will be a bit lower than for a twin-slot. Naturally, development of a new dual-polarized antenna structure with good coupling efficiency will further improve sensitivity of quasi-optical dual-polarized SIS receivers.

1.4.2 Dual Polarized Waveguide Receivers

One of the major components for a dual-polarized waveguide receiver is an orthomode transducer (OMT), which separates orthogonal polarizations within the same frequency band. Dual polarization waveguide receivers use high performance dual-polarized corrugated feed horns with symmetric Gaussian beam patterns, followed by OMTs to separate the two mutually orthogonal polarization signals into two different waveguide channels which eventually lead to two outputs for the mixers. The OMTs for millimeter waves often need to be broadband to match the broadband feed horns and mixers. One important consideration often overlooked in the design of wide band waveguide receiver components is the excitation of higher order modes. These are inevitably excited to some degree at the higher frequencies. One of the serious manifestations of the unwanted modes is the additional level of cross-polarization. Thus, for dual polarization receivers, it is desirable that the cross-polarization introduced by the OMT be less than that introduced by the horn and the related optics.

Unfortunately, in spite of the importance and common use of dual polarization receivers (mostly in satellite antennas and in earth stations), the design details of various components like OMTs are unsatisfactorily treated in the literature [30]. Moreover, high performance broadband OMTs are not available today at millimeter wavelengths.

1.4.3 Balanced Mixers

Balanced mixers suppress Local Oscillator amplitude modulation (AM) noise, have better power handling capabilities, and reject certain spurious responses and spurious signals [31]. At millimeter and submillimeter wavelengths, single-ended mixers are almost always used, and the LO power is coupled into the mixer using a waveguide directional coupler or an optical beamsplitter. If the signal path loss through the LO coupler is to be kept small, the LO loss must be substantial, and is typically 10–15 dB at submillimeter wavelengths. Furthermore, along with the LO signal, noise from the LO source is also coupled into the mixer in the signal and the image band. Moreover, most of the LO power is wasted, as only about 10% to 20% of the LO power is coupled to the mixer. Depending on the nature of the LO source, its sideband noise temperature may be room temperature or higher, which means that if the LO is at room temperature (300 K), then the 10–15 dB beamsplitter will contribute 30–10 K at the input of the mixer, and which may be comparable with the noise temperature of the receiver itself. Balanced mixers eliminate all these shortcomings. LO coupling into balanced mixers is much more efficient, LO power requirement is 10–15 dB relative to the single-ended mixer; and balanced mixers reject the LO thermal noise.

Balanced mixers can be implemented either in waveguide mounts or in quasi-optical configurations. Waveguide balanced mixers can be designed using a "magic tee" waveguide junction, which works as a 180° hybrid, along with two single-ended mixers. It is also possible to use finline mixers, where the RF is coupled through one end of the finline guide and the LO is coupled through the other end of the guide using waveguide to microstrip transition, which provides the 180° hybrid. However, no balanced mixer results have been reported to date at submillimeter wavelengths. Stephan *et al.* proposed the first quasi-optical balanced mixer at 90 GHz [32], and Tong *et al.* proposed a magic tee balanced mixer which potentially could be used at millimeter wavelengths [33]. A single chip balanced mixer was described by Kerr *et al.* [34], for 200–300 GHz, where a 180° hybrid is fabricated lithographically along with the SIS junctions, but no experimental results were given.

1.5 Overview of Thesis

This thesis is comprised of seven chapters. Chapter 2 focuses on the design and characterization of a dual-polarized cross-slot antenna on a dielectric substrate, using Fourier domain method-of-moments analysis. Chapter 3 describes the design, fabrication, and the performance of a low-noise dual-polarized quasi-optical SIS mixer at 550 GHz. The mixer utilizes the cross-slot antenna described in chapter 2, along with two junction tuning circuits, niobium trilayer SIS junctions, and an IF circuit containing a lumped element 180° hybrid. In chapter 4, the design of a balanced mixer at 530 GHz, the *first* balanced mixer at this frequency range, is described. This quasi-optical balanced mixer utilizes the dual-polarized mixer chip presented in chapter 3, a 180° IF hybrid circuit, and a wire-grid polarizer to couple the RF and LO signals at two orthogonal polarizations. Chapter 5 and 6 describe ortho-mode transducers (OMT), a critical component for waveguide dual-polarized receivers. Chapter 5 details a moderately broadband septum OMT, designed for the *Polatron* project, which will be used to measure the polarization angular power spectrum of the cosmic microwave background (CMB). Chapter 6 follows with a study of a finline OMT for possible use in millimeter wave dual-polarized receivers, and presents scalar model results at X-band. Finally, chapter 7 concludes with a summary of the results with a discussion of future research directions. Included in the Appendix A are the simulation files for Pcircuit [35], which is a linear circuit simulator program capable of handling superconducting transmission lines that was used to design and optimize the dual-polarized mixer. Appendix B lists the C++ program files for SuperMix [36], [37], a full harmonic balance program capable of evaluating SIS mixers with any number of junctions, which was used to evaluate the dual-polarized and balanced mixers.

References

[1] H. H. Meinel, "Commercial Applications of Millimeter Waves: History, Present Status, and Future Trends," *IEEE Trans. Microwave Theory Tech.*, vol. 43, no. 7, pp. 1639–1653, July 1995.

[2] P. F. Goldsmith, C. -T. Hsieh, G. R. Huguenin, J. Kapitzky, and E. L. Moore, "Focal Plane Imaging Systems for Millimeter Wavelengths," *IEEE Trans. Microwave Theory Tech.*, vol. 41, no. 10, pp. 1664–1675, October 1993.

[3] T. G. Phillips, and J. Keene, "Submillimeter Astronomy," *Proceedings of the IEEE*, vol. 80, no. 11, pp. 1662–1678, November 1992.

[4] J. E. Carlstrom, and J. Zmuidzinas, "Millimeter and Submillimeter Techniques," *Review of Radio Science 1993 – 1996*, W. R. Stone, ed., pp. 839–882, Oxford University Press, 1996.

[5] B. Ellison, M. L. Oldfield, D. N. Matheson, B. J. Maddison, C. M. Mann, and A. F. Smith, "Corrugated Horns at Terahertz Frequencies - Primary Results," *Proceedings of the Fifth International Symposium on Space Terahertz Technology*, Ann Arbor, Michigan, pp. 851-860, May 10–12, 1994.

[6] D. S. Wilsher, J. J. Spencer, C. M. Mann, and M. C. Gaidis, "A Moderate Cost 2.5 THz High Performance Feedhorn," *Proceedings of the Tenth International Symposium on Space Terahertz Technology*, Charlottesville, Virginia, pp. 429–435, March 16–18, 1999.

[7] G. Narayanan, N. Erickson, and R. Grosslein, "Low cost direct machining of Terahertz Waveguide Structures," *Proceedings of the Tenth International Symposium on Space Terahertz Technology*, Charlottesville, Virginia, pp. 516–529, March 16–18, 1999.

[8] C. K. Walker, G. Narayan, H. Knoepfle, J. Capara, J. Glenn, and A. Hungerford, "Laser Micromachining of Silicon : A New Technique for Fabricating High Quality Terahertz Waveguide Components," *Proceedings of the Eighth International Symposium on Space Terahertz Technology*, Cambridge, Massachusetts, pp. 358–376, March 25–27, 1997.

[9] T. W. Crowe, P. J. Koh, W. L. Bishop, C. M. Mann, J. L. Hesler, R. M. Weikle, P. A. D. Wood, and D. Matheson, "Inexpensive Receiver Components for Millimeter and Submillimeter Wavelengths," *Proceedings of the Eighth International Symposium on Space Terahertz Technology*, Cambridge, Massachusetts, pp. 377–384, March 25–27, 1997.

[10] J. W. Kooi, J. Pety, B. Bumble, C. K. Walker, H. G. LeDuc, P. L. Schaffer, and T. G. Phillips, "A 850-GHz Waveguide Receiver Employing a Niobium SIS Junction Fabricated on a 1 μm Si_3N_4 Membrane," *IEEE Trans. Microwave Theory Tech.*, vol. MTT-46, no. 2, pp. 151–161, February 1998.

[11] H. van de Stadt, A. Baryshev, P. Dieleman, Th. de Graauw, T. M. Klapwijk, S. Kovtonyuk, G. de Lange, I. Lapitskaya, J. Mees, R. Panhuyzen, G. Pokopenko, and H. Schaeffer, "A 1 THz Nb SIS Heterodyne Mixer with Normal Metal Tuning Structures," *Proceedings of the Sixth International Symposium on Space Terahertz Technology*, Pasadena, California, pp. 66–77, March 21–23, 1995.

[12] P. F. Goldsmith, *Quasioptical Systems : Gaussian Beam Quasioptical Propagation and Applications*, IEEE Press/Chapman & Hall Publishers Series on Microwave Technology and Techniques, New York, 1998.

[13] D. B. Rutledge, D. P. Neikirk, and D. P. Kasilingam, "Integrated Circuit Antennas," in *Infrared and Millimeter Waves*, K. J. Button, Ed., vol. 10, chapter 1, pp. 1–90, Academic Press, New York, 1983.

[14] D. F. Filipovic, S. S. Gearhart, and G. M. Rebeiz, "Double-Slot Antennas on Extended Hemispherical and Elliptical Silicon Dielectric Lenses," *IEEE Trans. Microwave Theory Tech.*, vol. MTT-41, no. 10, pp. 1738–1749, October 1993.

[15] W. R. Mcgrath, "Hot Electron Bolometer Mixers for Submillimeter Wavelengths : An Overview of Recent Developments," *Proceedings of the Sixth International Symposium on Space Terahertz Technology*, Pasadena, California, pp. 216–228, March 21–23, 1995.

[16] P. L. Richards, T. M. Shen, R. E. Harris, and F. L. Lloyd, "Quasiparticle heterodyne mixing in SIS tunnel junctions," *Appl. Phys. Lett.*, vol. 34, pp. 345–347, March 1, 1979.

[17] G. J. Dolan, T. G. Phillips, and D. P. Woddy, "Low-noise 115 GHz mixing in superconducting oxide-barrier tunnel junctions," *Appl. Phys. Lett.*, vol. 34, pp. 347–349, March 1, 1979.

[18] J. R. Tucker, "Quantum limited detection in tunnel junction mixers," *IEEE J. Quantum Electron.*, vol. 15, pp. 1234–1258, November 1979.

[19] M. Bin, M. C. Gaidis, J. Zmuidzinas, T. G. Phillips, and H. G. LeDuc, "Low-Noise 1 THz Niobium Superconducting Tunnel Junction Mixer With a Normal Metal Tuning Circuit," *Appl. Phys. Lett.*, vol. 68, pp. 1714–1716, March 18, 1996.

[20] M. Bin, M. C. Gaidis, J. Zmuidzinas, T. G. Phillips, and H. G. LeDuc, "Quasi-Optical SIS Mixers with Normal Metal Tuning Structures Junction Mixer With a Normal Metal Tuning Circuit," *IEEE Trans. Applied Superconductivity.*, vol. 7, pp. 3584–3588, 1997.

[21] J. Zmuidzinas, J. W. Kooi, J. Kawamura, G. Chattopadhyay, J. A. Stern, B. Bumble, and H. G. LeDuc, "Development of SIS Mixers for 1 THz," *Proceedings of SPIE : Advanced Technology MMW, Radio, and Terahertz Telescopes*, vol. 3357, pp. 53–61, May 1998.

[22] J. Kawamura, J. Chen, D. Miller, J. Kooi, J. Zmuidzinas, B. Bumble, H. G. LeDuc, and J. A. Stern, "Low-Noise Submillimeter-Wave NbTiN Superconducting Tunnel Junction Mixers," *Submitted in Appl. Phys. Lett.*, 1999.

[23] J. Zmuidzinas, H. G. LeDuc, "Quasi-Optical Slot Antenna SIS Mixers," *IEEE Trans. Microwave Theory Tech.*, vol. MTT-40, no. 9, pp. 1797–1804, September 1992.

[24] J. Zmuidzinas, N. G. Ugras, D. Miller, M. C. Gaidis, H. G. LeDuc, and J. A. Stern, "Low-noise slot antenna SIS mixers," *IEEE Trans. Appl. Superconduct.*, vol. 5, pp. 3053–3056, 1995.

[25] M. C. Gaidis, H. G. LeDuc, M. Bin, D. Miller, J. A. Stern, and J. Zmuidzinas, "Characterization of Low-Noise Quasi-Optical SIS Mixers for the Submillimeter Band," *IEEE Trans. Microwave Theory Tech.*, vol. MTT-44, no. 7, pp. 1130–1139, July 1996.

[26] M. Kominami, D. M. Pozar, and D. H. Schaubert, "Dipole and Slot Elements and Arrays on Semi-Infinite Substrates," *IEEE Trans. Antennas Propagat.*, vol. AP-33, no. 6, pp. 600-607, June 1985.

[27] A. R. Kerr, P. H. Siegel, and R. J. Mattauch, "A Simple Quasi-Optical Mixer for 100-120 GHz," in *1977 IEEE MTT-S Int. Microwave Symp. Dig.*, p. 96, 1977.

[28] J. Zmuidzinas, H. G. LeDuc, J. A. Stern, and S. R. Cypher, "Two-Junction Tuning Circuits for Submillimeter SIS Mixers," *IEEE Trans. Microwave Theory Tech.*, vol. MTT-42, no. 4, pp. 698–706, April 1994.

[29] Sanjay Raman, and Gabriel M. Rebeiz, "Single- and Dual-Polarized Millimeter-wave Slot-Ring Antennas," *IEEE Trans. Antennas Propagat.*, vol. AP-44, no. 11, pp. 1438-1444, November 1996.

[30] A.M. Bøifot, "Classification of Ortho-Mode Transducers," *European Trans. Telecommunications and Related Technologies*, vol. 2, no. 5, pp. 503-510, September 1991.

[31] S. A. Maas, *Microwave Mixers*, Second Edition, Artech House, Boston, 1993.

[32] K. D. Stephan, N. Camilleri, and T. Itoh, "A Quasi-Optical Polarization-Duplexed Balanced Mixer for Millimeter Wave Applications," *IEEE Trans. Microwave Theory Tech.*, vol. MTT-31, no. 2, pp. 164-170, February 1983.

[33] C. E. Tong, and R. Blundell, "A Self-Diplexing Quasi-Optical Magic Slot Balanced Mixer," *IEEE Trans. Microwave Theory Tech.*, vol. MTT-42, no. 3, pp. 383-388, March 1994.

[34] A. R. Kerr, and S.-K. Pan, "Design of Planar Image Separating and Balanced SIS Mixers," *Proceedings of the Seventh International Symposium on Space Terahertz Technology*, Charlottesville, Virginia, pp. 207-219, March 12-14, 1996.

[35] M. Bin, "Low-Noise THz Niobium SIS Mixers," PhD Dissertation, California Institute of Technology, Pasadena, October 1996.

[36] J. Ward, F. Rice, G. Chattopadhyay, and J. Zmuidzinas, "SuperMix : A Flexible Software Library for High-Frequency Circuit Simulation, Including SIS Mixers and Superconducting

Elements," *Proceedings of the Tenth International Symposium on Space Terahertz Technology*, Charlottesville, Virginia, pp. 269–281, March 16–18, 1999.

[37] F. Rice, J. Ward, J. Zmuidzinas, and G. Chattopadhyay, "Fast Harmonic Balance of SIS Mixers with Multiple Junctions and Superconducting Circuits," *Proceedings of the Tenth International Symposium on Space Terahertz Technology*, Charlottesville, Virginia, pp. 282–297, March 16–18, 1999.

Chapter 2

Dual-Polarized Cross-Slot Antenna

This chapter details the design, analysis, simulation, and performance of a dual-polarized cross-slot antenna on a dielectric substrate. The cross-slot antenna structure is similar to the twin-slot antenna on a hyperhemispherical substrate lens, which has been shown to be a good antenna for single polarization receivers [1]. The dual-polarized cross-slot antenna is obtained by crossing two-sets of twin-slots at 90°, as shown in Figure 2.1, and has four feed points. The cross-slot antenna is analyzed using a numerical method of moments analysis in the Fourier domain similar to that described by Kominami, Pozar, and Schaubert [2].

2.1 Design and Analysis

Figure 2.1 shows the cross-slot antenna structure. This design takes advantage of the fact that the slot length is $L \approx \lambda_d$, and therefore, a single slot would have voltage (or $\vec{E}$-field) maxima at $0.25\,L$ and $0.75\,L$ along its length. These voltage maxima correspond to nulls in the current flowing parallel to the slot on either side. Thus, crossing the slots at these points produces little perturbation in the current flow, which means that the introduction of two extra slots will not change the antenna performance, and the cross-slot antenna will primarily behave like the twin-slot antenna.

Much, but not all, can be learned about the field distribution inside the cross-slot antenna from simple symmetry considerations. The electric field distribution inside the slots is shown by the directions of the arrows in Figure 2.1, for the case that the horizontal pair of slots are excited symmetrically. The arrows in the figure indicate the direction of the fields only, and not amplitude; the electric fields inside the slots

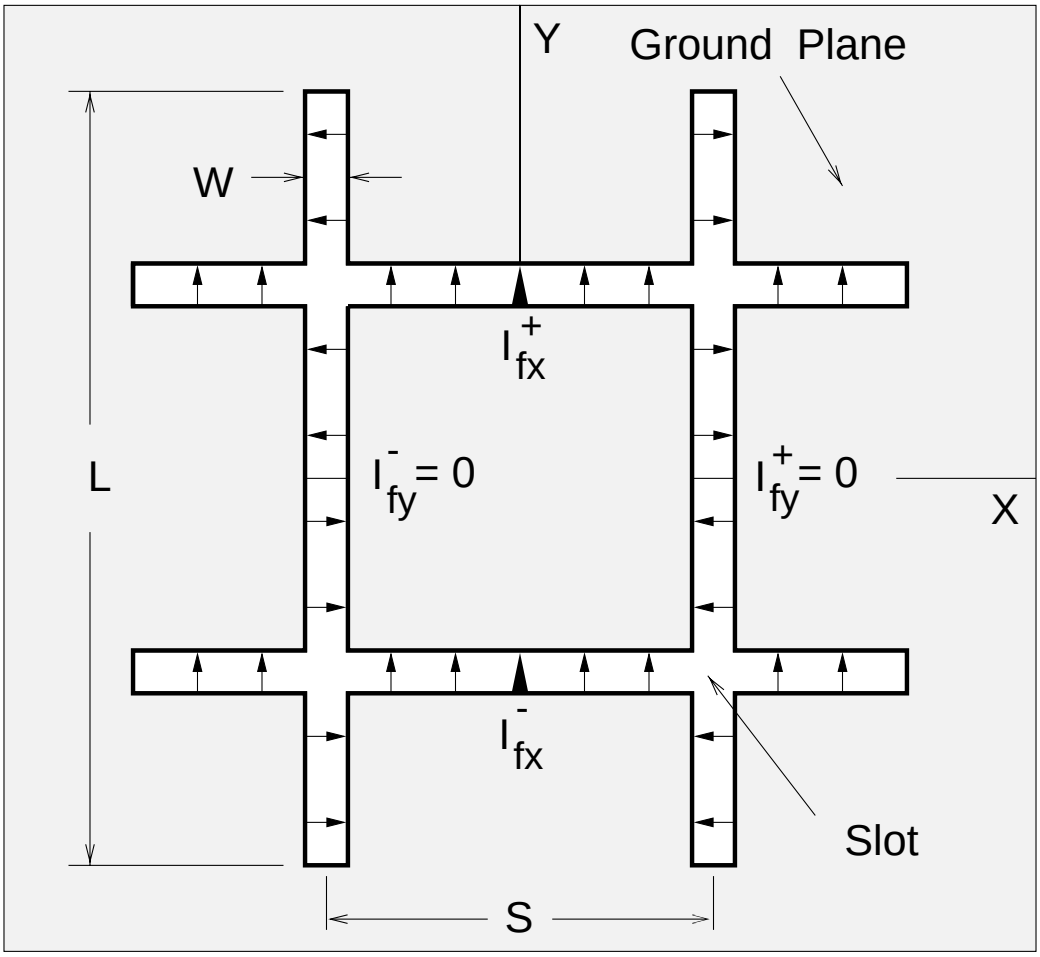

Figure 2.1 Proposed antenna structure. The four feed points are at the centers of the slots. The horizontal slots are symmetrically excited, $I_{fx}^{+} = I_{fx}^{-}$, and the vertical slots are not excited, $I_{fy}^{+} = I_{fy}^{-} = 0$.

have sinusoidal distribution and would be zero at the edges of the slots. It can be seen that the fields along $\hat{y}$–direction (horizontal slots) are symmetric, and the fields along the $\hat{x}$–direction (vertical slots) are antisymmetric. It is clear from the field distribution that the antenna will produce radiation that is predominantly polarized in the $\hat{y}$–direction for symmetric excitation of the horizontal slots. Due to the antisymmetric field distribution in the vertical slots, the radiation in the $\hat{x}$–direction will cancel, and the voltage at the orthogonal slots will vanish. Using the method of moments analysis, the properties of the cross-slot antenna are calculated in greater detail, including the full four-port impedance matrix, and the co-polarized and cross-polarized antenna radiation patterns, as a function of frequency.

2.1.1 Method of Moments Analysis

For method of moments analysis the substrate lens is treated as a semi-infinite dielectric slab. This is a very good approximation, since in practice, reflections at the lens surface can be largely eliminated by using an anti-reflection coating [3]. Figure 2.1 shows details of the cross-slot antenna where the horizontal slots are excited symmetrically with feed currents I_{fx}^{+} and I_{fx}^{-} respectively. The length and width of the slots are L and W $(W \ll \lambda_g)$, and the slot separation is S. The z–axis is defined to be normal to the antenna plane, and two other vectors on the $x-y$ plane $\vec{k_t} = (k_x, k_y, 0)$, and $\vec{p_t} = \hat{z}$ x $\vec{k_t}$ $= (-k_y, k_x, 0)$ are also defined. The admittance kernel, which relates the Fourier transforms of the electric fields and surface currents on the antenna plane, is a tensor under rotations of the $x - y$ plane and can be written as

$$Q_{\alpha\beta}(\vec{k_t}) = \frac{1}{Z_0}\Big[\Big(\frac{\epsilon_1 k}{\gamma_1} + \frac{\epsilon_2 k}{\gamma_2}\Big)\delta_{\alpha\beta} - \Big(\frac{1}{k\gamma_1} + \frac{1}{k\gamma_2}\Big)p_\alpha p_\beta\Big], \tag{2.1}$$

where $\delta_{\alpha\beta}$ is the Kronecker delta function ($\delta_{\alpha\beta} = 1$ for $\alpha = \beta$ and $\delta_{\alpha\beta} = 0$ for $\alpha \neq \beta$; $\alpha, \beta = x$ or y), p_α is a component of the vector $\vec{p_t}$, $k = \omega/c$ is the magnitude of the wave vector in free space, $Z_0 = 377\,\Omega$ is the impedance of free space, ϵ_1 and ϵ_2 are the dielectric constants above $(z > 0)$ and below $(z < 0)$ the antenna plane, and the z-component of the wave vector in the two half spaces are $\gamma_s^2 = \epsilon_s k^2 - k_x^2 - k_y^2$, with the conditions $\mathrm{Im}(\gamma_1) \leq 0$ and $\mathrm{Im}(\gamma_2) \geq 0$. The electric fields in the slots are expanded in a set of basis functions $f_{xi},\ f_{yi}$:

$$\begin{aligned} E_x(x,\, y) &= \sum_i \Big[V_{xi}^{+} f_{xi}(x,\, y - \frac{S}{2}) + V_{xi}^{-} f_{xi}(x,\, y + \frac{S}{2})\Big] \\ E_y(x,\, y) &= \sum_i \Big[V_{yi}^{+} f_{yi}(x - \frac{S}{2},\, y) + V_{yi}^{-} f_{yi}(x + \frac{S}{2},\, y)\Big], \end{aligned} \tag{2.2}$$

where $V_{xi}^{\pm}$ and $V_{yi}^{\pm}$ are the unknown amplitudes. The electric fields are Fourier transformed and then multiplied by the admittance kernels to yield the surface currents

$$J_\alpha(\vec{k_t}) = \sum_\beta Q_{\alpha\beta}(\vec{k_t})\, E_\beta(\vec{k_t}). \tag{2.3}$$

Using the condition that the currents must vanish inside the slots except at the feed points, and using the basis functions as testing functions (the Galerkin method), gives the following matrix equations for the amplitudes $V_{xi}^{\pm}$, $V_{yi}^{\pm}$:

$$\begin{aligned}
I_{xi}^{+} &= \sum_j \Big[V_{xj}^{+} Y_{xx,ij}^{++} + V_{xj}^{-} Y_{xx,ij}^{-+} + V_{yj}^{+} Y_{yx,ij}^{++} + V_{yj}^{-} Y_{yx,ij}^{-+} \Big] \\
I_{xi}^{-} &= \sum_j \Big[V_{xj}^{+} Y_{xx,ij}^{+-} + V_{xj}^{-} Y_{xx,ij}^{--} + V_{yj}^{+} Y_{yx,ij}^{+-} + V_{yj}^{-} Y_{yx,ij}^{--} \Big] \\
I_{yi}^{+} &= \sum_j \Big[V_{xj}^{+} Y_{xy,ij}^{++} + V_{xj}^{-} Y_{xy,ij}^{-+} + V_{yj}^{+} Y_{yy,ij}^{++} + V_{yj}^{-} Y_{yy,ij}^{-+} \Big] \\
I_{yi}^{-} &= \sum_j \Big[V_{xj}^{+} Y_{xy,ij}^{+-} + V_{xj}^{-} Y_{xy,ij}^{--} + V_{yj}^{+} Y_{yy,ij}^{+-} + V_{yj}^{-} Y_{yy,ij}^{--} \Big].
\end{aligned} \tag{2.4}$$

The admittance matrix elements are obtained from the admittance kernels and the Fourier transforms of the basis functions through the numerical evaluation of the integrals of the form

$$\begin{aligned}
Y_{xx,ij}^{\pm\pm} &= \frac{-1}{(2\pi)^2} \iint_{-\infty}^{\infty} Q_{xx} \tilde{f}_{xi} e^{\pm jk_y S/2} \left(\tilde{f}_{xj} e^{\pm jk_y S/2} \right)^{*} dk_x \, dk_y \\
Y_{yy,ij}^{\pm\pm} &= \frac{-1}{(2\pi)^2} \iint_{-\infty}^{\infty} Q_{yy} \tilde{f}_{yi} e^{\pm jk_x S/2} \left(\tilde{f}_{yj} e^{\pm jk_x S/2} \right)^{*} dk_x \, dk_y \\
Y_{xy,ij}^{\pm\pm} &= \frac{-1}{(2\pi)^2} \iint_{-\infty}^{\infty} Q_{xy} \tilde{f}_{xi} e^{\pm jk_y S/2} \left(\tilde{f}_{yj} e^{\pm jk_x S/2} \right)^{*} dk_x \, dk_y \\
Y_{yx,ij}^{\pm\pm} &= \frac{-1}{(2\pi)^2} \iint_{-\infty}^{\infty} Q_{yx} \tilde{f}_{yi} e^{\pm jk_x S/2} \left(\tilde{f}_{xj} e^{\pm jk_y S/2} \right)^{*} dk_x \, dk_y,
\end{aligned} \tag{2.5}$$

where $\tilde{f}_{xi}$ and $\tilde{f}_{yi}$ are the Fourier transforms of $f_{xi}(x, y)$ and $f_{yi}(x, y)$ respectively, and the $(*)$ denotes complex conjugate. There are five such independent admittance matrix elements with $\mathbf{Y}_{xx}^{++} = \mathbf{Y}_{xx}^{--}$, $\mathbf{Y}_{yy}^{++} = \mathbf{Y}_{yy}^{--}$, $\mathbf{Y}_{xx}^{+-} = \mathbf{Y}_{xx}^{-+}$, $\mathbf{Y}_{yy}^{+-} = \mathbf{Y}_{yy}^{-+}$ and $\mathbf{Y}_{xy}^{++} = \mathbf{Y}_{xy}^{-+} = \mathbf{Y}_{yx}^{++} = \mathbf{Y}_{yx}^{+-} = -\mathbf{Y}_{xy}^{--} = -\mathbf{Y}_{xy}^{+-} = -\mathbf{Y}_{yx}^{--} = -\mathbf{Y}_{yx}^{-+}$. The current moments $I_{xi}^{\pm}$ and $I_{yi}^{\pm}$ are equal to the feed currents $I_{fx}^{\pm}$ and $I_{fy}^{\pm}$ respectively with suitable normalizations of the basis functions. Entire domain basis (EDB) functions used by Kominami *et al.* [2], which prescribe a sinusoidal variation of the electric

fields in the slots, are used for the horizontal slots. The functions are

$$f_i(x,\, y) = \frac{1}{\pi\sqrt{(W/2)^2 - y^2}} \cdot \begin{cases} \dfrac{\sin k_i(L/2 - |x|)}{\sin k_i L/2} & (i \text{ odd}) \\ \dfrac{1 - \cos k_i(L/2 - |x|)}{1 - \cos k_i L/2} & (i \text{ even}) \end{cases} \tag{2.6}$$

and the parameters k_i are arbitrarily chosen to be roughly integer multiples of the propagation constant calculated using the mean dielectric constant $(1 + \epsilon_r)/2$. For the vertical slots, antisymmetric triangular basis functions of the form

$$A_n(x;\, d) = T(x - x_n;\, d) - T(x + x_n;\, d), \tag{2.7}$$

are used, where $x_n = nd;\ n = 1, 2, \ldots, n_{max};\ d = L/[2(n_{max} + 1],$ and $T(x, d)$ is a triangular function extended over $(-d, d)$. The equations $I_{xi}^{\pm}$ and $I_{yi}^{\pm}$, given in equation (2.4), are overlap integrals between the feed currents in the slots and the basis functions. Thus, $I_{xi}^{+} = I_{xi}^{-} = I_{fx}$ – the feed current, since the horizontal slots are excited symmetrically, and $I_{yi}^{+} = I_{yi}^{-} = 0,$ since the vertical slots are not excited. The impedance matrix can be obtained by inverting the admittance matrix, $\mathbf{Z} = \mathbf{Y^{-1}}$, as shown by Zmuidzinas and LeDuc [1]. For symmetric excitation, the mode amplitudes can be written as:

$$\begin{aligned} V_{xi}^{+} &= I_{fx} \sum_j \Big[Z_{xx,ij}^{++} + Z_{xx,ij}^{-+} \Big], \qquad V_{xi}^{-} = I_{fx} \sum_j \Big[Z_{xx,ij}^{+-} + Z_{xx,ij}^{--} \Big], \\ V_{yi}^{+} &= I_{fx} \sum_j \Big[Z_{xy,ij}^{++} + Z_{xy,ij}^{-+} \Big], \qquad V_{yi}^{-} = I_{fx} \sum_j \Big[Z_{xy,ij}^{+-} + Z_{xy,ij}^{--} \Big]. \end{aligned} \tag{2.8}$$

The antenna impedance is calculated by taking the ratio of the total voltage at the feed point over the feed current, and are given by:

$$\begin{aligned} Z^{+}_{ant} = \frac{\sum_i V^{+}_{xi}}{I_{fx}} &= \sum_{i,j} Z^{++}_{xx,ij} + \sum_{i,j} Z^{-+}_{xx,ij} \\ Z^{-}_{ant} = \frac{\sum_i V^{-}_{xi}}{I_{fx}} &= \sum_{i,j} Z^{+-}_{xx,ij} + \sum_{i,j} Z^{--}_{xx,ij} \end{aligned} \tag{2.9}$$

The mode amplitudes given in the equation (2.8) allow the electric fields in the slots to be calculated in the Fourier domain:

$$\begin{aligned} E_x(k_x,\, k_y) &= \sum_i \Big[V^{+}_{xi} f^{+}_{xi}(k_x,\, k_y) + V^{-}_{xi} f^{-}_{xi}(k_x,\, k_y) \Big] \\ E_y(k_x,\, k_y) &= \sum_i \Big[V^{+}_{yi} f^{+}_{yi}(k_x,\, k_y) + V^{-}_{yi} f^{-}_{yi}(k_x,\, k_y) \Big], \end{aligned} \tag{2.10}$$

where $f^{+}_{xi}(k_x,\, k_y)$ and $f^{-}_{xi}(k_x,\, k_y)$ are the Fourier transform of $f_{xi}(x,\, y - \frac{S}{2})$ and $f_{xi}(x,\, y + \frac{S}{2})$ respectively; and $f^{+}_{yi}(k_x,\, k_y)$ and $f^{-}_{yi}(k_x,\, k_y)$ are the Fourier transform of $f_{yi}(x - \frac{S}{2}\, y)$, and $f_{yi}(x + \frac{S}{2},\, y)$ respectively. Finally, the radiated electric field can be calculated using the field quantities in the equation (2.10), and can be written in polar coordinates $(r,\, \theta,\, \phi)$ by

$$\mathbf{E}_{\alpha}(r,\, \theta,\, \phi) = \frac{\exp\left(-jk_{\alpha} r\right)}{r} \mathbf{g}_{\alpha}(\theta,\, \phi) \tag{2.11}$$

where the amplitude and polarization of the electric field radiated in the direction $(\theta,\, \phi)$ is obtained from $E_x(k_x,\, k_y)$ and $E_y(k_x,\, k_y)$ using:

$$\begin{aligned} &\mathbf{g}_{\alpha}(\theta,\, \phi) = \frac{-jk_{\alpha}}{\pi} \\ &\cdot \Big[E_x(k_{\alpha}\, \sin\theta\cos\phi,\, k_{\alpha}\, \sin\theta\sin\phi) \cdot [\cos\theta\, \hat{\mathbf{x}} - \sin\theta\cos\phi\, \hat{\mathbf{z}}] \cdot j \sin\Big(k_{\alpha} \frac{S}{2} \sin\theta\cos\phi \Big) \\ &+ E_y(k_{\alpha}\, \sin\theta\cos\phi,\, k_{\alpha}\, \sin\theta\sin\phi) \cdot [\cos\theta\, \hat{\mathbf{y}} - \sin\theta\sin\phi\, \hat{\mathbf{z}}] \cdot \cos\Big(k_{\alpha} \frac{S}{2} \sin\theta\sin\phi \Big) \Big]. \end{aligned}$$

Here $\alpha = 1, 2$ labels the half-space $z > 0$ or $z < 0$ (or equivalently, $0 \leq \theta < \pi/2$ and $\pi/2 < \theta \leq \pi$) and $k_\alpha = \epsilon_\alpha^{1/2} k$. The factors $\sin(k_\alpha[S/2]\sin\theta\cos\phi)$ and $\cos(k_\alpha[S/2]\sin\theta\sin\phi)$ are simply the array factor for two slots separated by a distance S along the x-axis and y-axis respectively. Since antisymmetric basis functions are used for the vertical slots, the array factor for the slots separated along the x-axis is antisymmetric as well. The power dP radiated into a solid angle $d\Omega$ is given by

$$\frac{dP}{d\Omega} = \frac{\sqrt{\epsilon_\alpha}}{Z_0}|\mathbf{g}_\alpha(\theta, \phi)|^2, \tag{2.13}$$

as can easily be seen by calculating the Poynting vector $\mathbf{S} = \mathbf{E}$ x $\mathbf{H}^*$ and using $|\mathbf{H}| = {\epsilon_\alpha}^{1/2}|\mathbf{E}|/Z_0$. The co-polarized and cross-polarized radiated fields are obtained from the equation (2.11), and for cross-polarization calculations the third definition given by Ludwig [4] is used.

2.2 Results

2.2.1 Antenna Impedance

A program has been developed to perform this method of moments analysis. Calculations are done for a cross-slot antenna with dimensions $L = 200\,\mu$m, $S = 100\,\mu$m, $W = 10\,\mu$m, which is the "standard" geometry used for a 500 GHz antenna on a silicon ($\epsilon_r = 11.8$) substrate. Typically, six basis functions of each type (EDB and triangular) are used in the analysis. The calculated impedance as a function of frequency is plotted in Figure 2.2, and in general, is quite similar to the twin-slot case. The cross-slot antenna has a broad region of low impedance which lies in between two high-impedance resonances, as can be seen from the figure. The antenna impedance bandwidth is quite broad, the 1 dB impedance bandwidth for matching the antenna to a $30\,\Omega$ resistive load (impedance of the antenna at 500 GHz was calculated to be $28\,\Omega$) was found to be about 200 GHz ($\approx 40\%$ bandwidth).

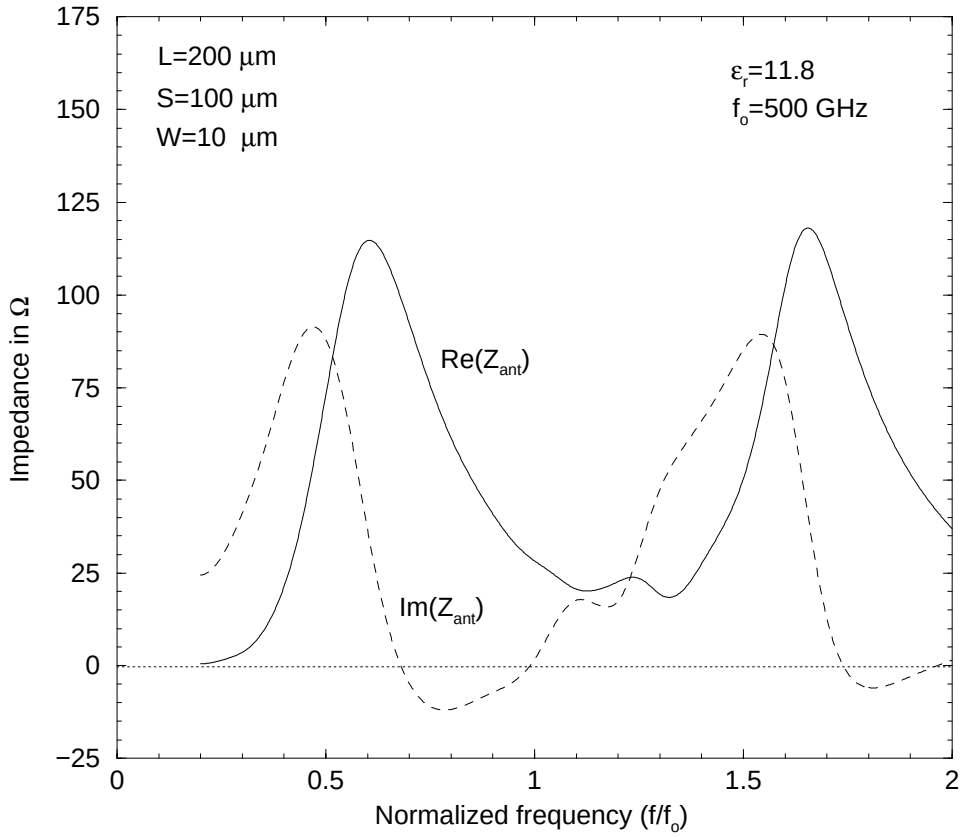

Figure 2.2 Antenna impedance as a function of frequency for the cross-slot antenna on a semi-infinite silicon dielectric substrate.

2.2.2 Antenna Radiation Pattern

A contour plot of the co-polarized and cross-polarized power pattern radiated into the dielectric is shown in Figure 2.3. The contours for the co-polarized power pattern are linearly spaced from 1% to 92% of the peak co-polarized power in increments of 7%; and the contours for the cross-polarized power pattern are linearly spaced from 5% to 95% of the peak cross-polarized power in increments of 5%. The beams are found to be fairly symmetric with half power beam widths of 52° for the E–plane, and 46° for the H–plane. The main beam efficiency (power in the main lobe, to the first null) is quite high, 88.2% (see Table 2.1). The remaining power is radiated into small E–plane sidelobes (1.6%), and to the cross-polarized field (0.6%) in the dielectric; and the rest is radiated backwards into air (9.9%). The phase of the antenna showed a small error (in the H-plane), but fortunately the reduction in the coupling efficiency

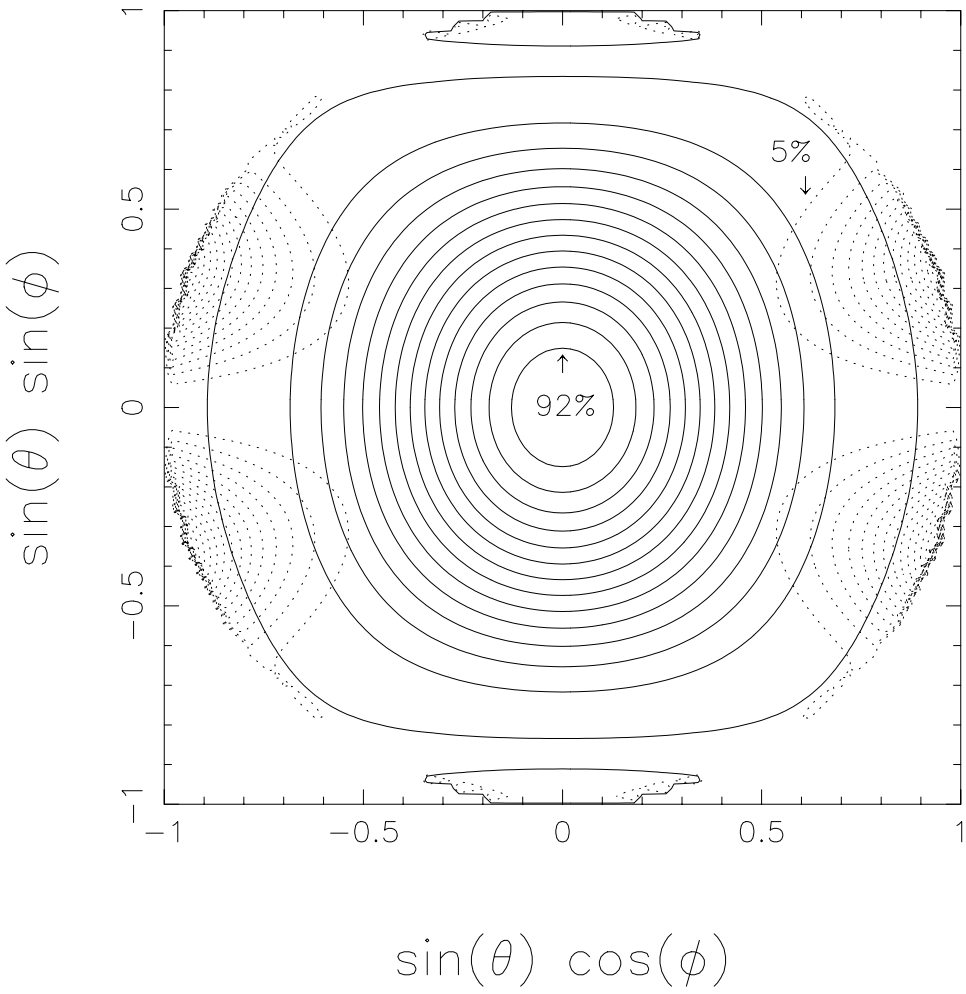

Figure 2.3 Contour plots of the calculated co-polarized and cross-polarized power pattern radiated into the dielectric by the antenna. The solid lines are for the co-polarized power and the dotted lines are for the cross-polarized power. The dimensions of the slot are the same as in Figure 2.2. For the co-polarized power, the contours are linearly spaced from 1% to 92% of the peak co-polarized power, in increments of 7%; and for the cross-polarized power, the contours are linearly spaced from 5% to 95% of the peak cross-polarized power in increments of 5%. The quantities (θ, ϕ) are the usual polar angles with respect to $\hat{z}$.

due to this is very low. The error is due to a slight astigmatism: the E–plane and H–plane phase centers are slightly displaced from each other in a direction normal to the substrate. The cross-slot antenna shows good cross-polarization performance with the cross-polarization peak power 24 dB below the co-polarized peak power. The hyperhemispherical lens on which the antenna will be placed will affect the cross-polarization response, because the transmission through the air/dielectric interface

Table 2.1 Antenna Results

	E-plane	H-plane
HWHM	26°	23°
Phase -3dB	0°	−2.9°
Power lost to:		
(i) Cross-polarized field in dielectric = 0.6%		
(ii) Sidelobes in dielectric = 1.3%		
Power radiated backwards into "air" = 9.9%		
Main beam efficiency for the co-polarized beam = 88.2%		

at the lens surface depends on the polarization and angle of incidence. However, experimental wire grid polarizer measurements on a 500 GHz receiver using a twin-slot antenna show that the total cross-polarization is no more than -20 dB, indicating that the effect of an anti-reflection coated lens on the cross-polarization is quite low.

2.3 Conclusion

The cross-slot antenna appears to be an excellent candidate for millimeter and sub-millimeter quasi-optical devices. The impedance, radiation pattern, and bandwidth of the cross-slot are very similar to those of the twin-slot. In comparison to the dual polarized slot-ring antenna, where a single annular (circular or square shaped) slot is used, and is fed at two points which are 90° apart, and has been shown to provide good results at 94 GHz [5]; the cross-slot offers superior radiation characteristics. The slot-ring antenna has a broader radiation pattern (in angle) than the cross-slot antenna. This is simply due to the fact that at any given frequency, the transverse dimensions of a slot-ring are smaller than those of a cross-slot. This broader pattern of the slot-ring will be somewhat more difficult to couple to, so the efficiency will be a bit lower compared to a cross-slot antenna [6].

References

[1] J. Zmuidzinas, and H. G. LeDuc, "Quasi-Optical Slot Antenna SIS Mixers," *IEEE Trans. Microwave Theory Tech.*, vol. MTT-40, no. 9, pp. 1797-1804, September 1992.

[2] M. Kominami, D. M. Pozar, and D. H. Schaubert, "Dipole and Slot Elements and Arrays on Semi-Infinite Substrates," *IEEE Trans. Antennas Propagat.*, vol. AP-33, no. 6, pp. 600-607, June 1985.

[3] M. C. Gaidis, H. G. LeDuc, M. Bin, D. Miller, J. A. Stern, and J. Zmuidzinas, "Characterization of Low-Noise Quasi-Optical SIS Mixers for the Submillimeter Band," *IEEE Trans. Microwave Theory Tech.*, vol. MTT-44, no. 7, pp. 1130-1139, July 1996.

[4] Arthur C. Ludwig, "The Definition of Cross Polarization," *IEEE Trans. Antennas Propagat.*, vol. AP-21, no. 1, pp. 116-119, January 1973.

[5] Sanjay Raman, and Gabriel M. Rebeiz, "Single- and Dual-Polarized Millimeter-wave Slot-Ring Antennas," *IEEE Trans. Antennas Propagat.*, vol. AP-44, no. 11, pp. 1438-1444, November 1996.

[6] G. Chattopadhyay, and J. Zmuidzinas, "A Dual-Polarized Slot Antenna for Millimeter Waves," *IEEE Trans. Antennas Propagat.*, vol. AP-46, no. 5, pp. 736-737, May 1998.

Chapter 3

Dual-Polarized Quasi-Optical SIS Mixer

This chapter describes the design, fabrication, and the performance of a low-noise dual-polarized quasi-optical superconductor insulator superconductor (SIS) mixer at 550 GHz. The mixer utilizes a novel cross-slot antenna on a hyperhemispherical substrate lens, described in chapter 2, two junction tuning circuits, niobium trilayer junctions, and an IF circuit containing a lumped element 180° hybrid. The antenna has four feed points, two for each polarization, and each feed point is coupled to a two-junction SIS mixer. The 180° IF hybrid is implemented using a lumped element/microstrip circuit located inside the mixer block. Fourier transform spectrometer (FTS) measurements of the mixer frequency response, co-polarized and cross-polarized beam patterns for both polarizations, and the heterodyne noise performance measurements in single polarization and dual-polarization configurations are presented here.

3.1 Mixer Design

The easiest method to design an SIS mixer using the crossed-slot antenna would be to couple a separate tuned SIS circuit to each of the four antenna ports. One possible concern in this approach would be that the resonant frequencies of the four SIS circuits might not all be the same, which would lead to degraded cross-polarization, and inferior performance overall. To minimize this effect, tuning circuits in which the junction *separation* dictates the tuning inductance [1] is used. In this technique, the circuit can be fed either from both ends as shown in Figure 3.1(a), or from one end as shown in Figure 3.1(b). Both these feeding arrangements give an *impedance* bandwidth equal to the shunt tuning inductance, described in [1], which is the ideal

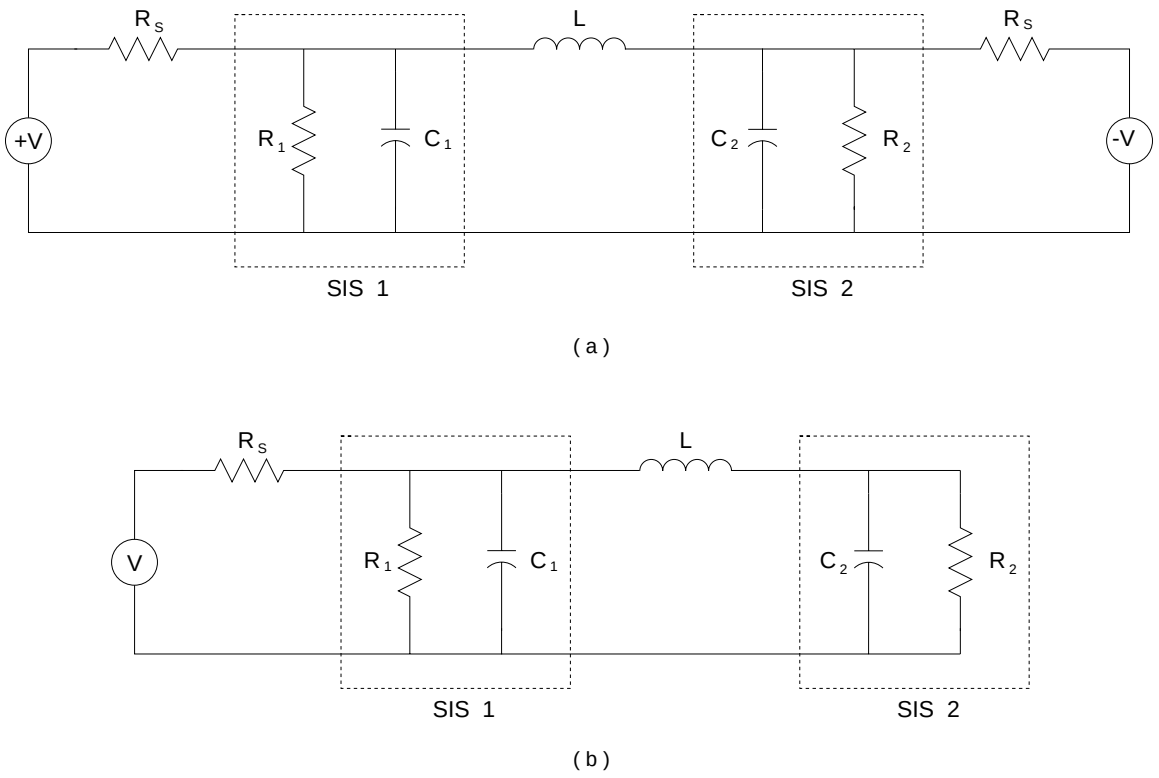

Figure 3.1 Diagrams showing tuning circuits which use two SIS junctions: (a) shows the circuit for two-feed configuration; and (b) shows the circuit for single-feed configuration. In both circuits, the inductance is chosen so that $L/2$ tunes out the capacitance of a single junction (assuming $C_1 = C_2$).

tuning circuit for an SIS junction. These two-junction circuits do not use DC blocking capacitors, and the tuning inductance is precisely controlled by the separation of the two junctions. Since both junctions are defined in the same lithography step, the tuning inductance is nearly immune to registration errors between layers.

3.1.1 Circuit Design

The mixer layout is shown in Figure 3.2. The radiation received by the cross-slot antenna is coupled into the SIS junctions with superconducting microstrip lines. The properties of the superconducting microstrip lines were calculated using the methods described by Zmuidzinas and LeDuc [2], which includes the frequency-dependent surface impedance of niobium as given by Mattis-Bardeen [3] theory in the local limit. Quarter-wave microstrip stubs, as shown in the figure, are used to effect the coupling

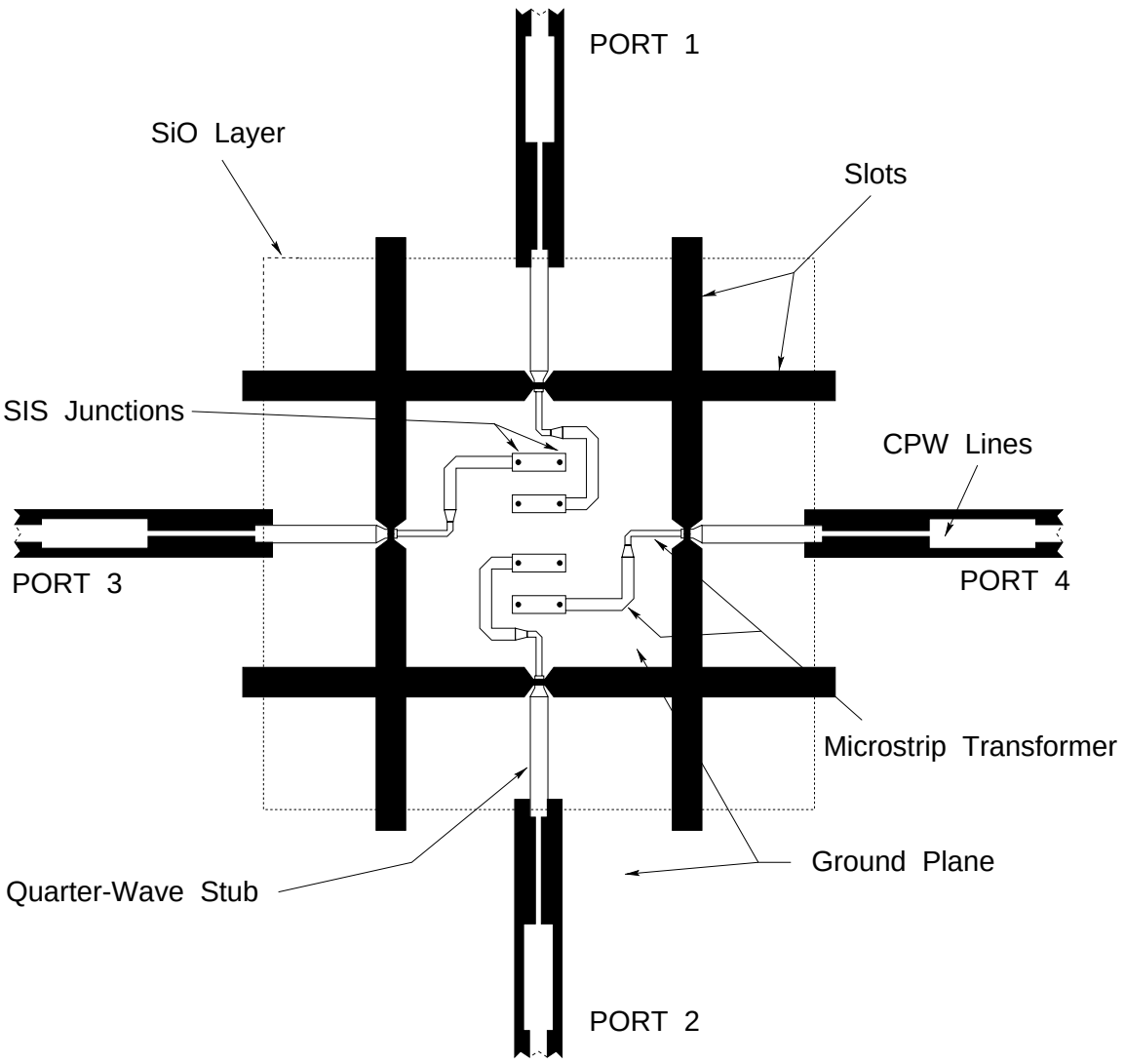

Figure 3.2 Details of the mixer layout. CPW lines carry the IF output to the 180° hybrid, not shown here. The junctions are placed as shown to allow suppression of the Josephson effect with a single magnet.

to the slot antennas by providing an RF short-circuit between the microstrip and one side of the slot antenna. The two section quarter-wave microstrip transformer allows a good impedance match between the antenna ($\approx 30\ \Omega$) and the tunnel junctions ($R_n/2 \approx 7\ \Omega$). The relatively low antenna impedance promotes good matching to even low resistance tunnel junctions.

The four SIS circuits connected at the four ports, as shown in the figure, are combined into two horizontal and vertical polarization outputs simply by biasing the circuits

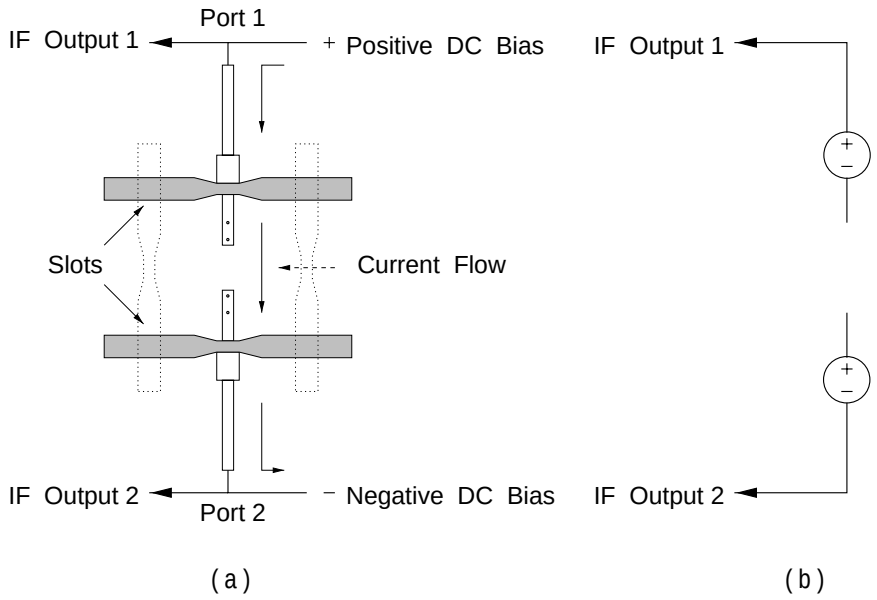

Figure 3.3 Schematic showing how the two IF outputs for a given polarization are 180° out of phase: (a) shows the current flow for biasing the junctions in series and (b) shows the equivalent bias circuit.

in series from IF port 1 to 2, and from 3 to 4. This also eliminates the necessity of attaching an electrical connection to the isolated ground plane at the center of the cross-slot with the ground plane outside the slots. The junctions are placed as shown in Figure 3.2 to allow suppression of the Josephson effect with a single magnet. A simulation program called "Pcircuit," developed in house [4], was used to simulate and optimize the RF device performance (Appendix A). It can be seen from Figure 3.2 that for each polarization there are two IF outputs and four SIS junctions, for a total of eight junctions on the chip. In principle, single junction mixers could also be used, which would require only four junctions per chip.

3.1.2 180° hybrid

Due to the mixer structure and the series bias of the junction pairs, it turns out that the two IF outputs for a given polarization are 180° out of phase. This can be easily explained. For a given polarization, like the horizontal pair of slots, as shown in Figure 3.3(a), the LO and RF will have the same relative phase at either port (1 or 2), so one would expect the IF currents to be in phase. However, due to

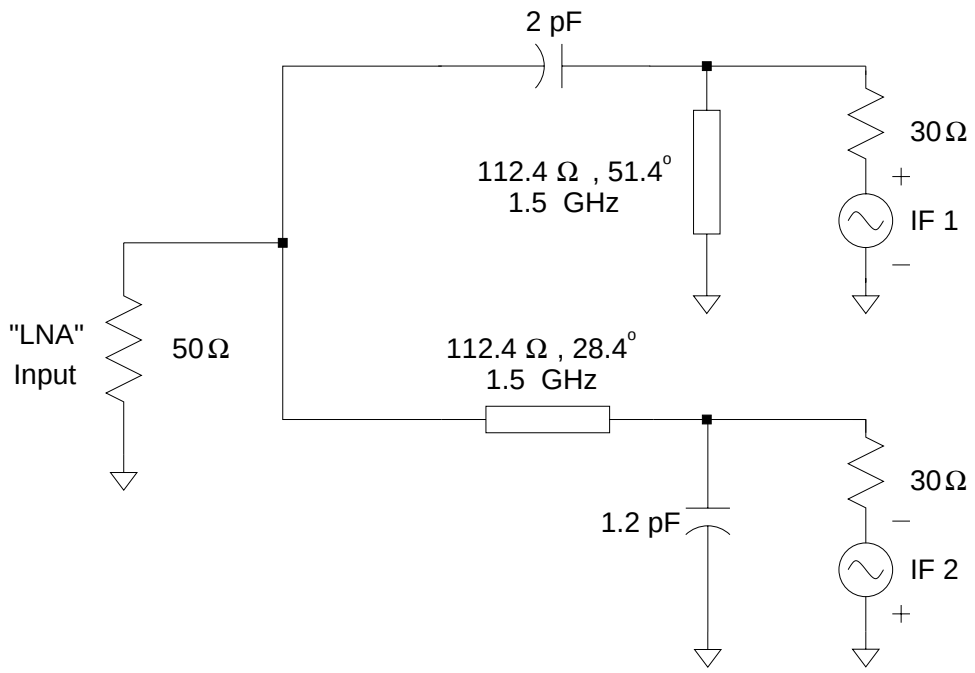

Figure 3.4 Circuit diagram for the 180° hybrid. LNA input port impedance is 50Ω, the two IF output impedance ports are 30Ω, and the two IF outputs are 180° out of phase.

the series biasing of the junctions, one junction pair is "forward" biased while the other is "reverse" biased. As shown in the equivalent circuit in Figure 3.3(b), the two IF outputs are 180° out of phase, and thus a 180° hybrid circuit is necessary to combine the two IF outputs for a given polarization. The hybrid circuit is designed using a first order lowpass-highpass filter combination, whose bandwidth at 1.5 GHz center frequency is 500 MHz. The hybrid is implemented using a combination lumped element/microstrip circuit as shown in Figure 3.4. The circuit was optimized using Hewlett Packard's microwave design system (MDS) [5] to deliver maximum power to a 50 Ω load (the LNA input) from two 180° out of phase 30 Ω generators (the SIS IF outputs). The input reflection coefficient (S_{11}) of the lumped hybrid IF circuit was measured at cryogenic temperatures to evaluate its performance and to verify the design.

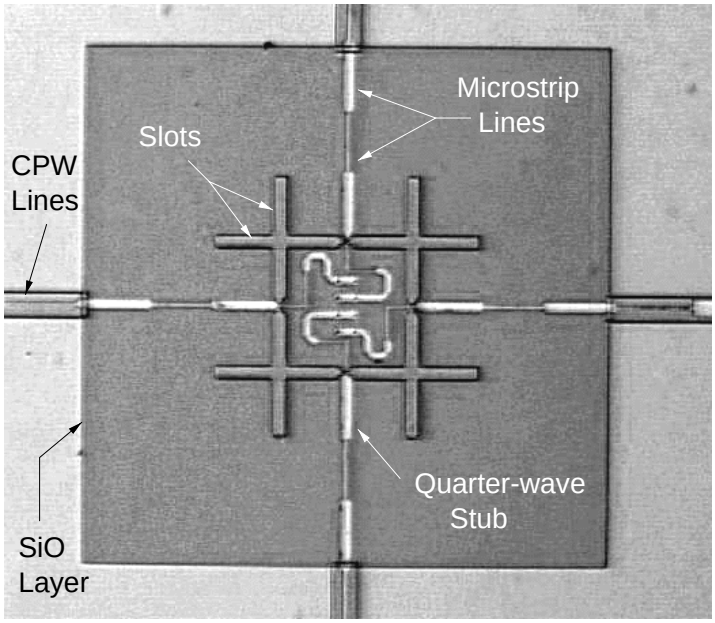

(a)

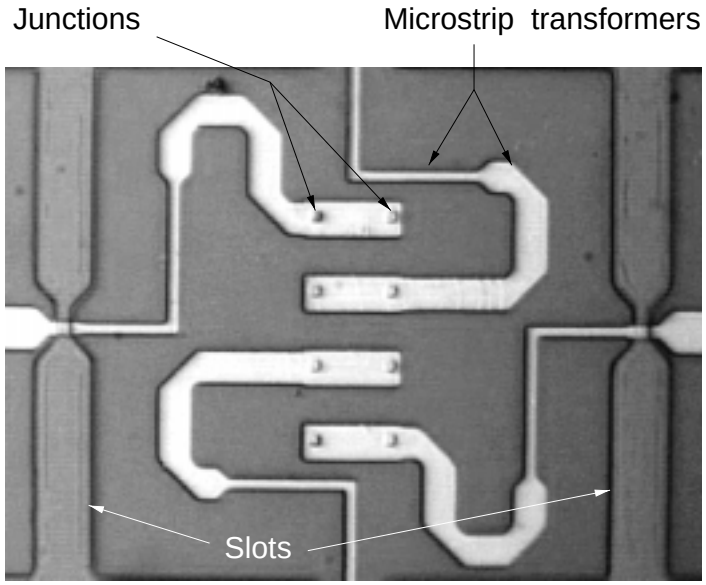

(b)

Figure 3.5 Actual picture of a cross-slot mixer chip: (a) shows the slots, microstrip transmission lines, and CPW lines; (b) shows the close-up view of the junctions, the tuning inductors, and the microstrip transformers used to match the antenna impedance to the junction impedance.

Table 3.1 SIS Device Data

Junction area: $1.44\,\mu\text{m}^2, 1.69\,\mu\text{m}^2, 1.96\,\mu\text{m}^2$
Current density: $J_c \approx 7.1$ kA/cm^2
$R_nA \approx 26\,\Omega\,\mu\text{m}^2$
Ground plane: 2000 Å Niobium
Wiring layer: 2500 Å Niobium
Dielectric layer: 2000 Å SiO for transformers and inductors

3.1.3 Device Fabrication

The mixer chip fabrication was performed at the JPL Center for Space Microelectronics Technology, using their standard Nb/Al-Oxide/Nb trilayer process. This is essentially the same process described by Zmuidzinas *et al.* [1], which uses all optical lithography. A three mask level junction fabrication with a 2000 Å thick niobium ground plane, 2500 Å thick niobium wiring layer and a single layer of 2000 Å thick SiO, which is used as the dielectric for the superconducting microstrip lines, was used. Junctions were fabricated with three different junction areas $1.44\,\mu\text{m}^2$, $1.69\,\mu\text{m}^2$, and $1.96\,\mu\text{m}^2$. Though the design was optimized for $1.69\,\mu\text{m}^2$ area junctions, it was decided to fabricate three different junction area devices to allow for process variations. The SIS devices are fabricated on a 0.25 mm thick, 50 mm diameter, high-resistivity ($> 100\,\Omega$-cm) silicon wafer, which is then diced into 2.0 x 2.0 mm individual chips. For these devices the junction area resistance product R_NA was measured to be $26\,\Omega\,\mu\text{m}^2$, and device current density was measured to be 7.1 kA cm^{-2}. Table 3.1 summarizes the SIS device data. Figure 3.5 shows the picture of the fabricated mixer chip, showing the SIS junctions and other microstrip and CPW transmission lines.

3.2 Receiver Configuration

A general view of the receiver configuration is shown in Figure 3.6; specific modifications for single and dual-polarization measurements will be described later. The local oscillator (LO) used for antenna beam pattern and heterodyne measurements

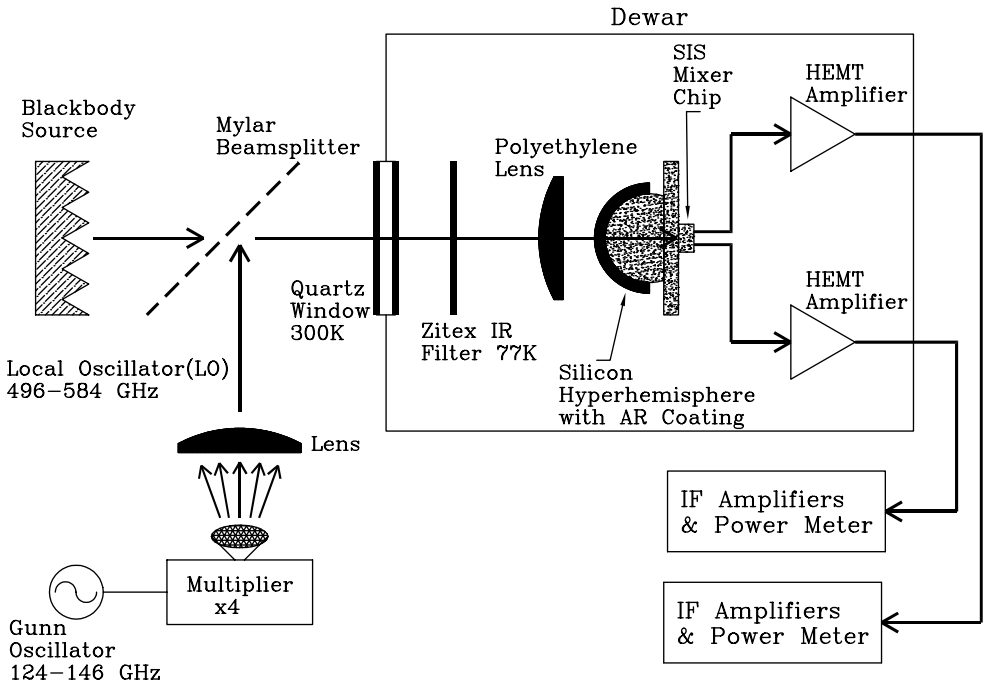

Figure 3.6 Simplified receiver layout. The elements within the dewar are mounted on a 4.2 K cold plate.

is a tunable Gunn oscillator with varactor multipliers [6], [7]. The RF and the LO signals pass through a 10 μm thick mylar beamsplitter and the combined signals travel into the cryostat through a 3.8 mm thick crystal quartz pressure window at room temperature, followed by a 0.1 mm thick Zitex [8] IR filter at 77 K. Inside the cryostat the well-collimated ($\approx F/17$) beam is matched to the broad beam pattern of the cross-slot antenna with a polyethylene lens and a silicon hyperhemispherical lens with anti-reflection (AR) coating of alumina-loaded epoxy [9], [10]. The quartz pressure window is AR coated with Teflon. Semirigid coaxial cables connect the SMA IF output ports with HEMT low noise amplifiers (LNAs). The 1.0 - 2.0 GHz LNAs have measured noise temperatures of 5 K [11]. The LNA outputs are sent to room temperature amplifiers and diode detectors which measure the total IF power in 500 MHz IF bandwidth.

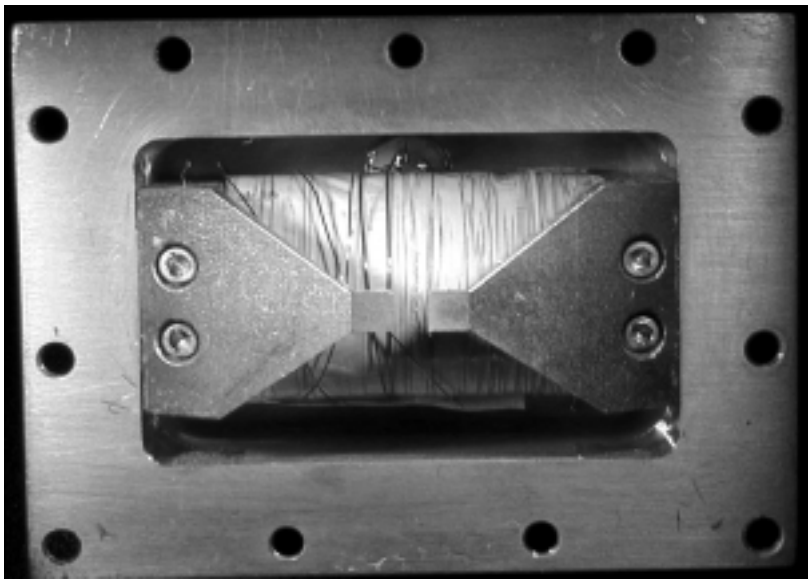

(a)

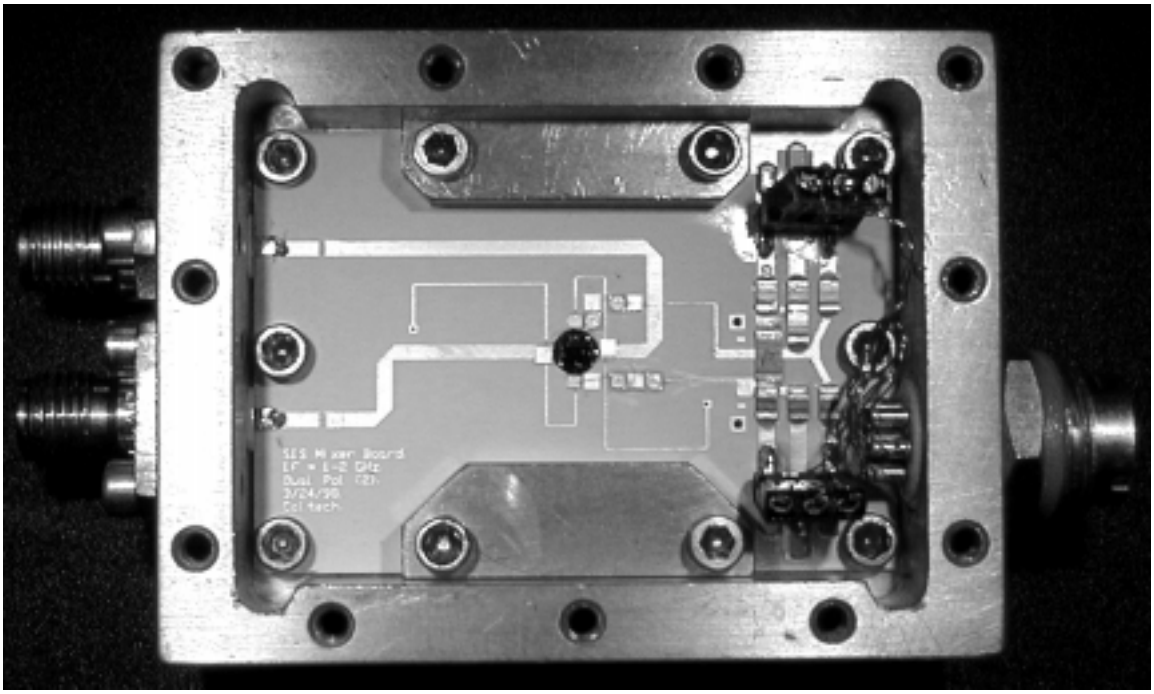

(b)

Figure 3.7 Picture of the disassembled mixer block: (a) shows the magnet housing, (b) shows the bias and IF circuits along with the 180° hybrid, and the mixer chip at the center.

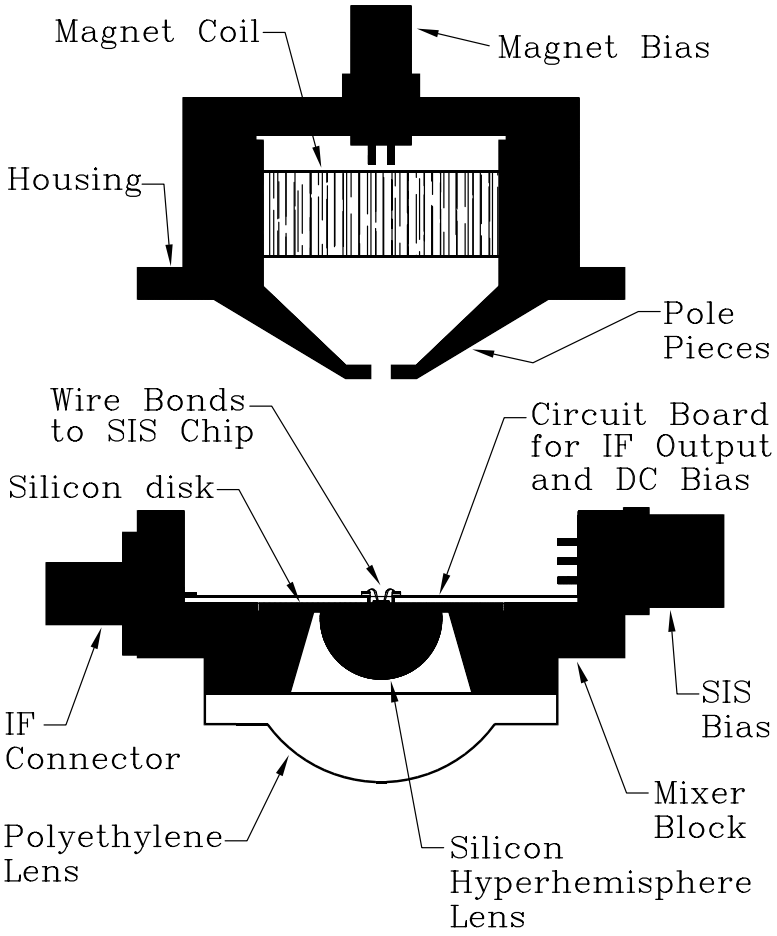

Figure 3.8 Schematic of the mixer block showing the hardwares used inside the block.

3.2.1 Mixer Assembly

For the dual-polarization mixer, an existing single polarization mixer block, described in detail by Gaidis *et al.* [12], was used with some minor modifications, such as a second SMA connector to bring out two IF outputs for the two polarizations. Figure 3.7 presents a picture of a disassembled mixer block. Figure 3.7(a) shows the magnet housing. The magnet is used to suppress Josephson effects, and consists of approximately 3600 turns of superconducting NbTi wire on a #1018 cold-rolled steel core. Steel pole pieces serve to concentrate the field at the junctions to allow operation at lower magnet currents. Figure 3.7(b) shows bias and IF circuitry along with the lumped element 180° hybrid, and the mixer chip at the center of the mixer block. Figure 3.8 shows the drawing of the mixer block giving details of the hardwares used

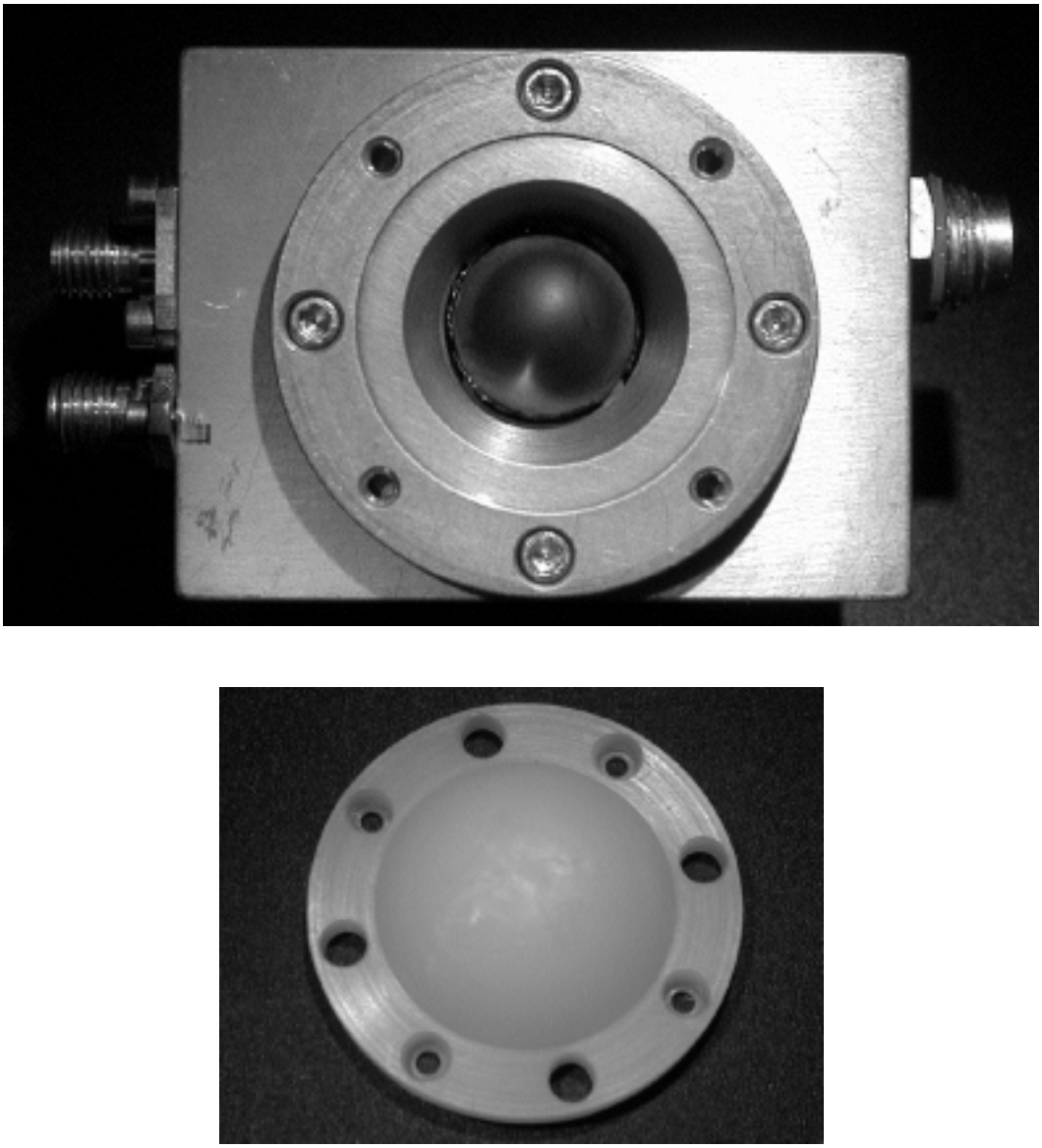

Figure 3.9 Actual picture of an assembled block, with the polyethylene lens removed to show the AR coated silicon hyperhemisphere. The SMA connectors for the two IF outputs can be seen on the left and the multi-pin bias connector can be seen on the right.

inside the block. As indicated in Figure 3.8, the back side of the SIS mixer chip is glued [13] to one side of a silicon support disk, and the silicon hyperhemisphere is glued [13] to the opposite side of the disk. The high resistivity ($> 1000\ \Omega$-cm) silicon support disk is 2.5 cm in diameter and 1.0 mm thick. The silicon hyperhemisphere consists of a very high resistivity ($\approx 4000\,\Omega$-cm) silicon [14], diamond-machined into

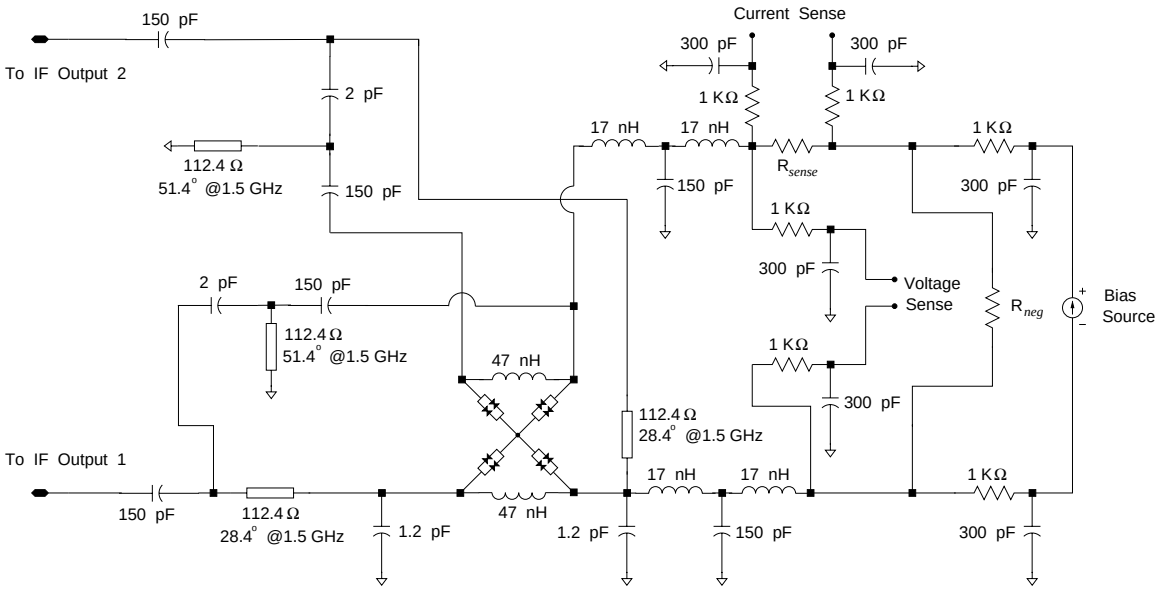

Figure 3.10 The circuit schematic showing the details of biasing and IF circuits on the printed circuit board.

a 6.35 mm radius hemisphere with a 0.7 mm extension [10]. The high resistivity silicon ensures low RF losses, but is likely to be not very critical when operating at 4.2 K. The thickness of the hyperhemisphere's extension, the support disk, and the chip substrate all add up to place the device at the aplanatic focus of the hyperhemisphere.

The silicon disk is clamped in the mixer block by a printed circuit board, which is held in place by metal clamps and screws, as shown in Figure 3.7(b). The circuit board is 0.64 mm thick TMM6 temperature stable microwave laminate from Rogers corporation, with room temperature dielectric constant 6.0 [15]. A multi-pin Microtech connector [16] is connected on the right side of the block for DC bias supply connections and bias voltage and current read out. The mixer IF outputs, after being combined by the 180° hybrids, are carried on two different microstrip lines to SMA connectors on the left of the block. Figure 3.9 shows the assembled mixer block, with the polyethylene lens removed to reveal the silicon hyperhemispherical lens. The mixer block is attached to the 4.2 K cold plate with a mounting fixture.

3.2.2 DC Bias and IF Circuits

The schematic in Figure 3.10 details the DC bias and IF circuitry on the printed circuit board. A single bias source is used to bias all the junctions, for both the horizontal and the vertical polarizations. The DC bias source resistance is adjustable by feedback to present the mixer with either a current source or a voltage source. Resistor R_{neg} is chosen at approximately 100 Ω to prevent unstable biasing due to regions of negative dynamic resistance in the SIS I-V curve. The current-sensing resistor R_{sense} is 10 Ω, and the IF-blocking spiral inductors (17 nH) at liquid helium temperature (4.2 K) add $\ll 1\ \Omega$ series resistance. The 150 pF DC blocking capacitors in Figure 3.10 are attached to the IF output microstrips with silver-loaded epoxy. The chip inductors are wire-bonded to the top electrodes of the 150 pF bypass capacitors. The SIS mixer chip sits within a through hole at the center of the board, allowing straight forward wire-bonding of the mixer chip to the biasing network and to the 180° hybrid circuits. The remaining chip resistors, chip capacitors, and connector pins are attached to the circuit board traces with either solder or silver-loaded epoxy. Two 180° hybrids for the two polarizations are also shown in the schematic circuit diagram.

3.3 Measurements and Results

3.3.1 Antenna Beam Pattern Measurements

The beam pattern of the dual-polarized antenna was measured with an antenna measurement system [17] and is shown in Figure 3.11. The test set-up consists of an aperture limited chopped hot-cold load on a x-z linear stage, stepper motors to drive the linear stage, a lock-in amplifier, and a data acquisition system. The hot load is a heat emitter at a constant temperature of about 240° C, and the Eccosorb on the chopping wheel acts as room temperature cold load. For the beam pattern measurements the SIS receiver is run as a heterodyne detector. The IF output of the mixer is detected, amplified, and fed to the lock-in amplifier. Since the lock-in is set at the

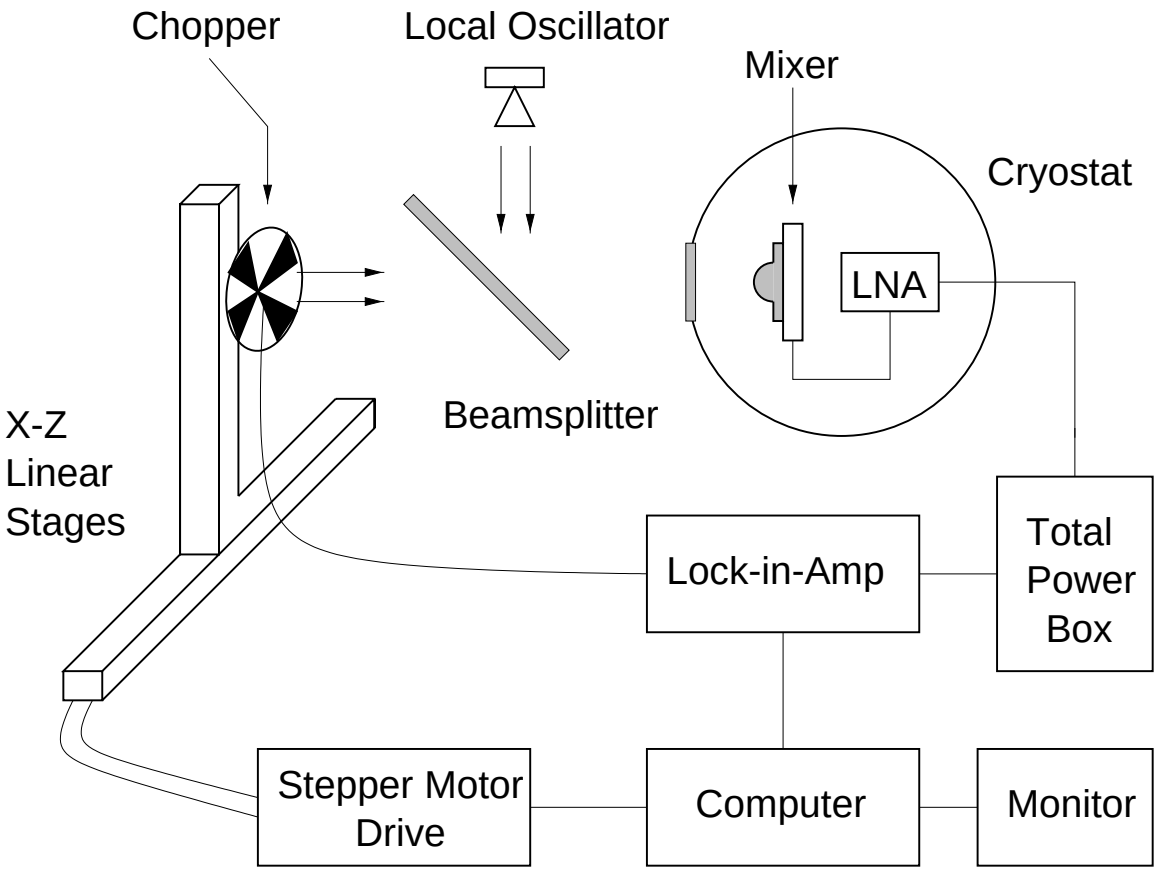

Figure 3.11 Antenna beam pattern measurement set-up.

chopping frequency (usually around 220 Hz), the lock-in output is the total power of the hot-cold source signal detected by the SIS mixer. The lock-in output signal is a voltage that represents power level of the antenna pattern.

For the beam pattern measurements the hot-cold load linear stage was placed at 24 cm away from the cryostat vacuum window. The hot-cold load aperture was set at 3.2 mm and the lock-in amplifier time constant was set at 3 seconds, giving a signal to noise of about 18 dB for the measurement set-up. The mixer was pumped with a 528 GHz LO source. The hot-cold RF signal and the LO were coupled to the junctions through a 10 μm thick beamsplitter. Figure 3.12 shows the co-polarized beam pattern contour plot for the horizontal pair of slots, and Figure 3.13 shows the corresponding E-plane and H-plane cuts for the beam. Figure 3.14 shows the co-polarized beam pattern contour plot for the vertical pair of slots, and Figure 3.15 shows the

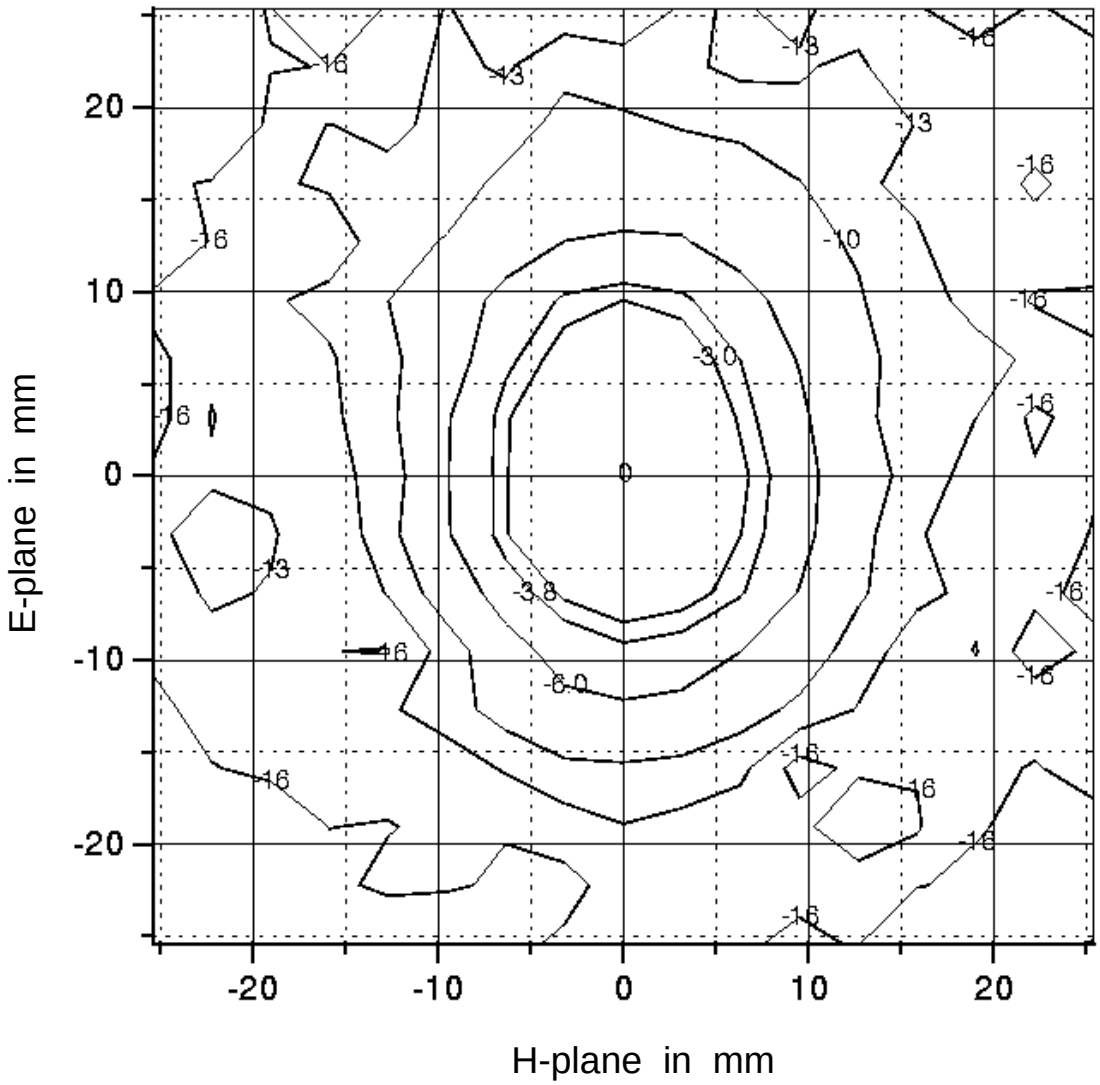

Figure 3.12 Co-polarized antenna beam pattern contour plot for the horizontal pair of slots. The LO frequency for this measurement was set at 528 GHz.

corresponding E-plane and H-plane cuts for the beam. The E-plane beam is wider than the H-plane beam (as is expected) for both the polarizations. For the horizontal slots, the E-plane and H-plane FWHM was found to be 18.5 mm and 14 mm respectively, giving E/H ratio of 1.3, which is higher than the theoretical prediction of 1.14. For the vertical pair of slots, the E-plane and H-plane FWHM was found to be 18 mm and 13 mm respectively. The discrepancy between the measured and the calculated beam width ratio may be due to the misalignment of the mixer-chip with

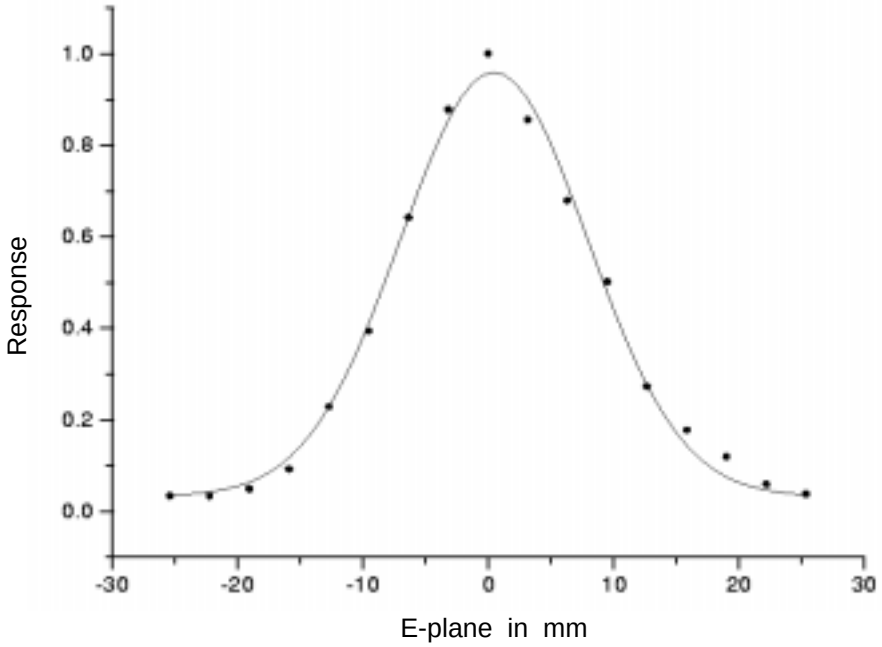

(a)

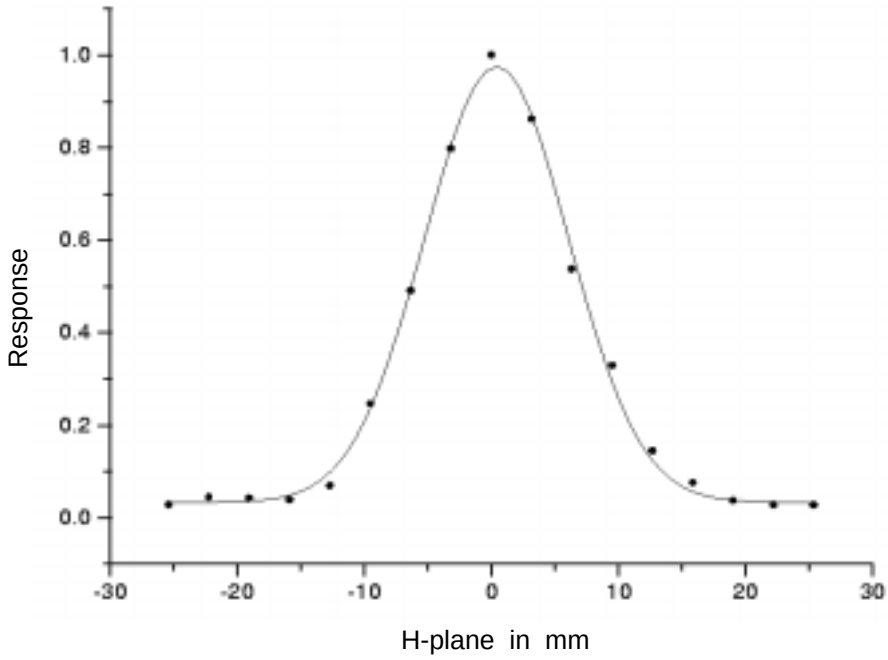

(b)

Figure 3.13 The E-plane and H-plane cuts for the beam shown in Figure 3.12: (a) shows E-plane cut and (b) shows H-plane cut.

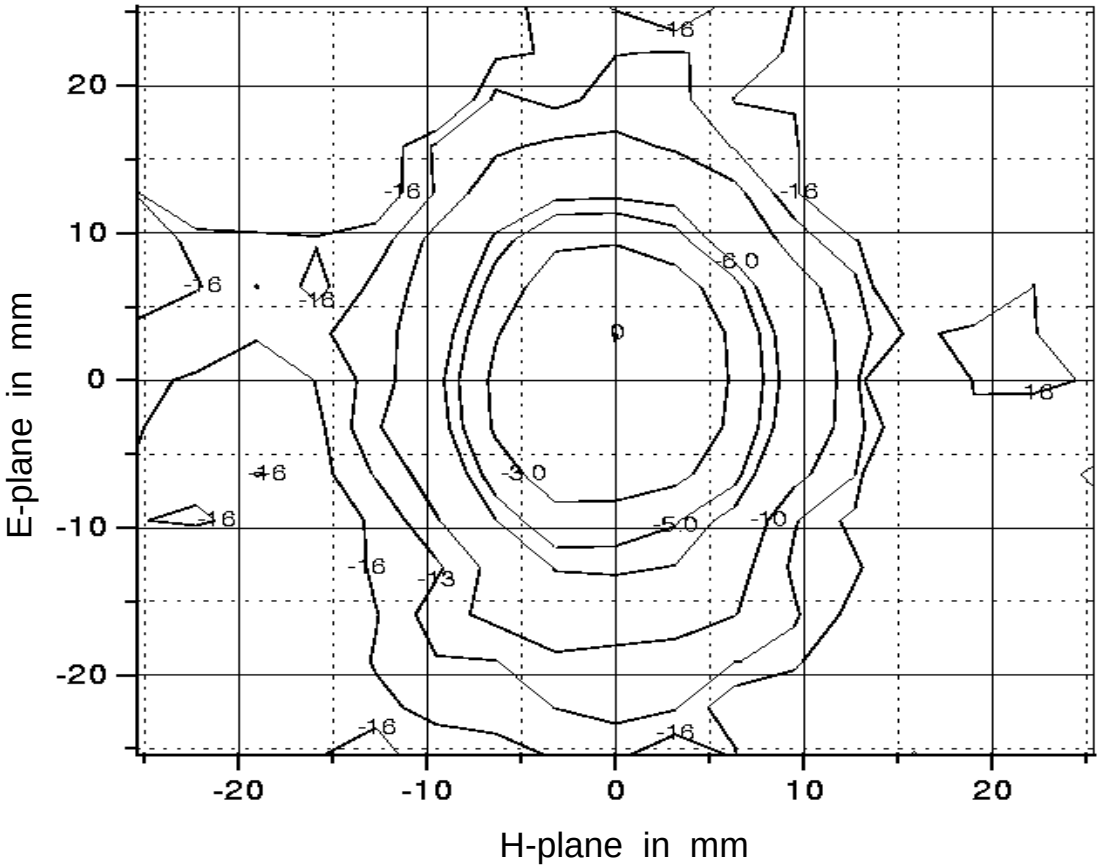

Figure 3.14 Co-polarized antenna beam pattern contour plot for the vertical pair of slots. The LO frequency for this measurement was set at 528 GHz.

respect to the silicon hyperhemispherical lens. It can be seen in Figure 3.12 that the beam is stretched a bit towards the bottom end of the E-plane. This asymmetry is not expected theoretically and may be indicative of chip/lens misalignment. A few experiments were carried out to ascertain this, and is described in the next section (3.3.2). Initially, it was thought that the stretching of the beam could be the result of distortion of the shape of the plastic lens at liquid helium temperature (4.2 K), but this was found not to be the case in the subsequent measurements.

For cross-polarization measurement a wire-grid polarizer was used in front of the cryostat window. The hot-cold load aperture was set at 6.4 mm and the lock-in amplifier time constant was set at 10 seconds, which improved the signal to noise to about 28 dB. The cross-polarization beam pattern is shown in Figure 3.16. One

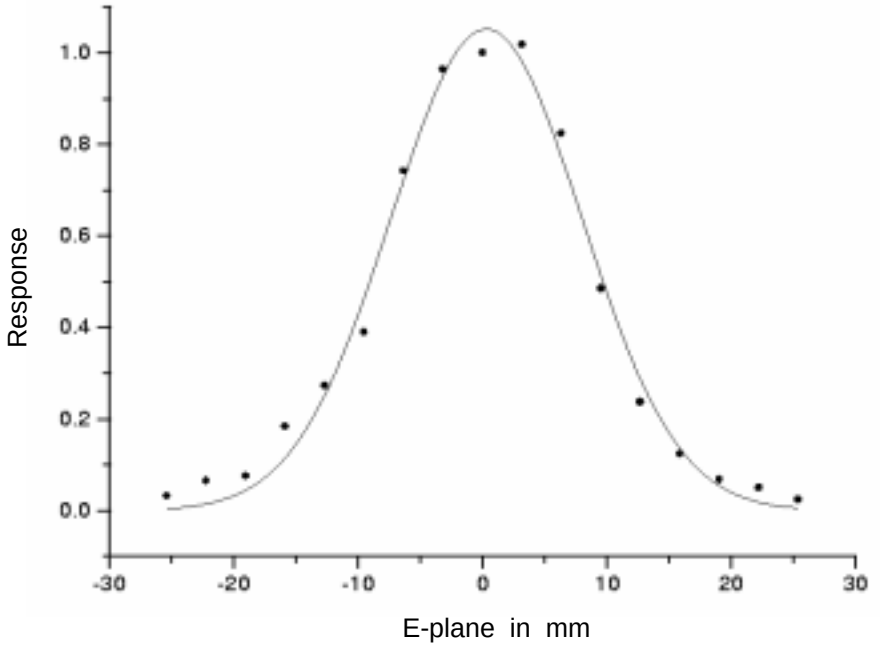

(a)

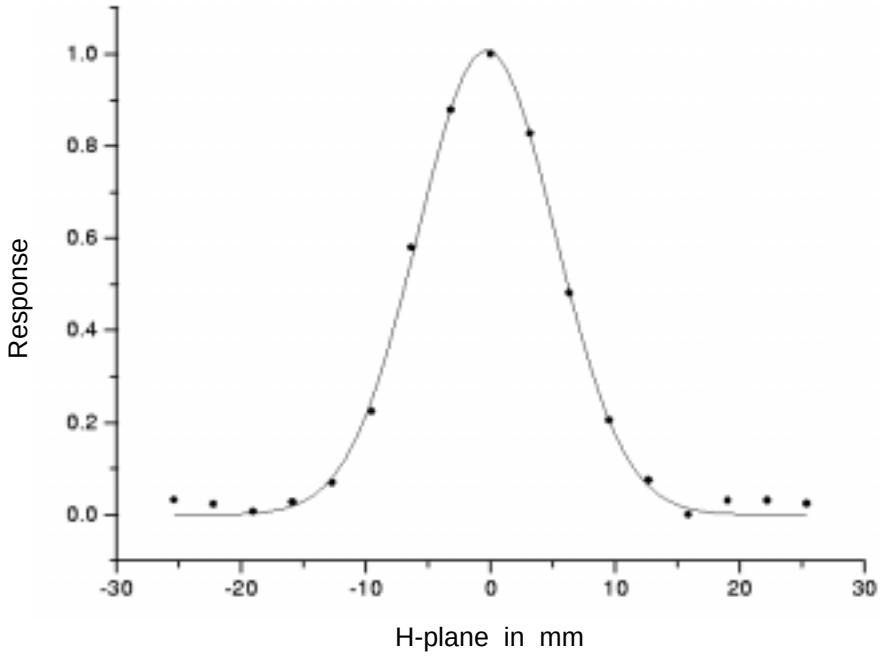

(b)

Figure 3.15 The E-plane and H-plane cuts for the beam shown in Figure 3.14 : (a) shows E-plane cut and (b) shows H-plane cut.

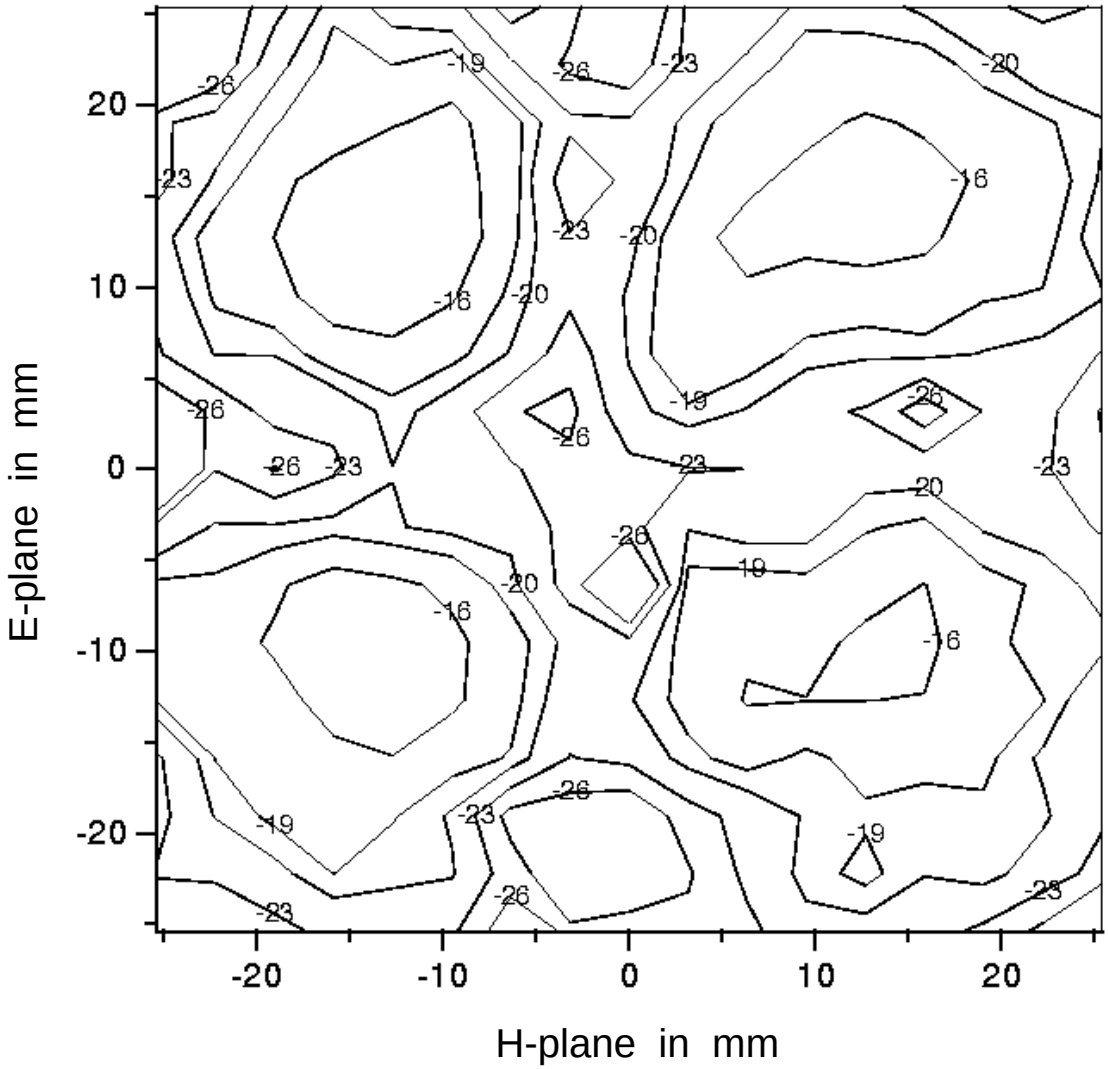

Figure 3.16 Cross-polarization beam pattern in dB, relative to the peak co-polarized power. The LO frequency for this measurement was set at 528 GHz.

can see from the cross-polarization plot that the four lobes are not identical, and is suspected to be due to the misalignment of the mixer-chip. To verify this, another chip was mounted on the silicon hyperhemispherical lens, deliberately misaligning the chip with respect to the silicon lens, and the resulting cross-polarization pattern is shown in Figure 3.17. The plot clearly demonstrates that the chip alignment plays a significant role in cross-polarization level of the beam. From Figure 3.16 the integrated cross-polarization level was found to be around -15 dB (compared to the

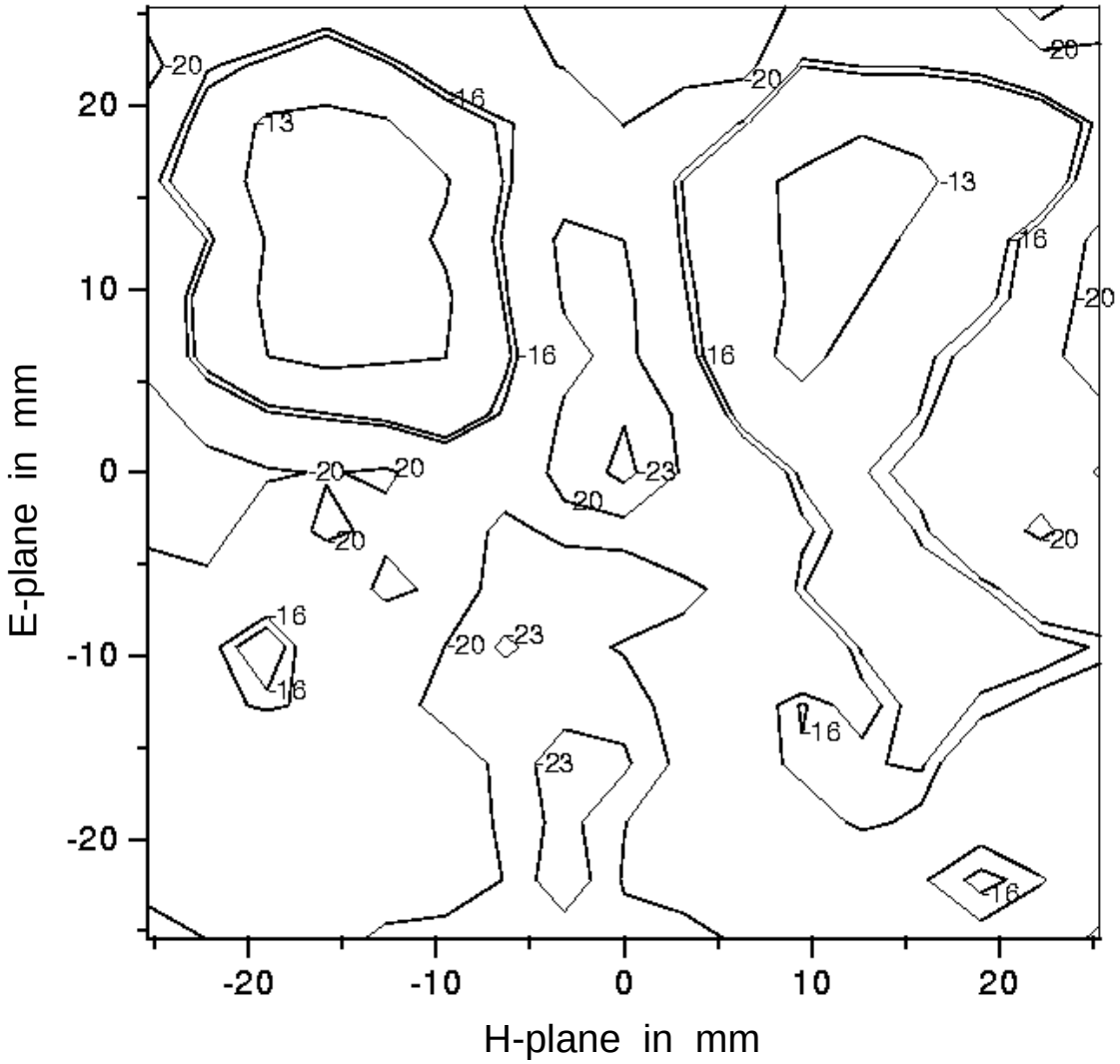

Figure 3.17 Cross-polarization beam pattern in dB, relative to the peak co-polarized power when the chip is misaligned with respect to the silicon hyperhemispherical lens. The LO frequency for this measurement was set at 528 GHz.

integrated co-polarized beam), which includes the effects of the wire-grid polarizer and the beamsplitter.

3.3.2 Mixer Chip Alignment

Plastic Lens Distortion

It has been mentioned in the previous section that the antenna beam pattern results show that the beams have been stretched in one direction, giving E/H ratio higher

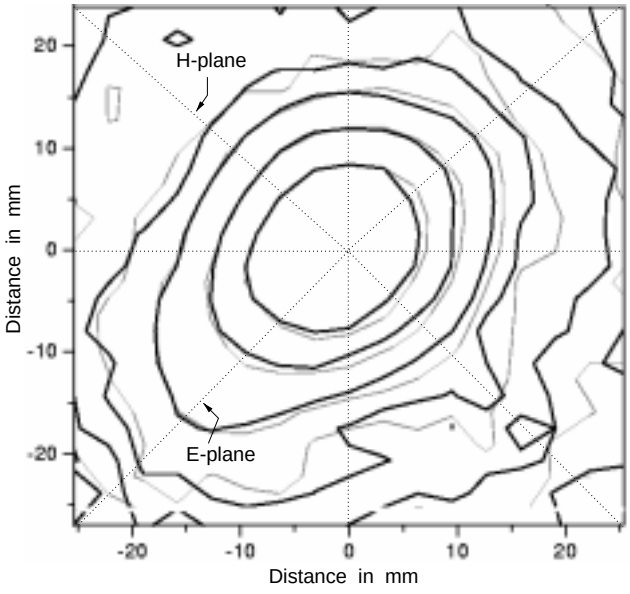

(a)

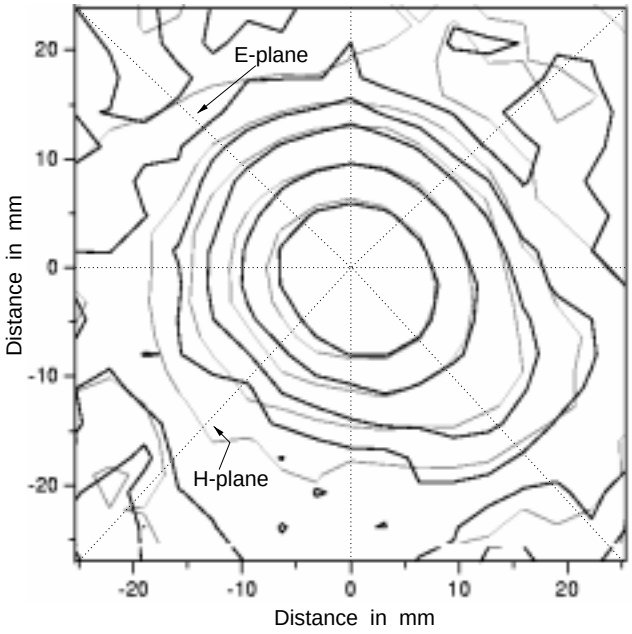

(b)

Figure 3.18 Comparison of co-polarized antenna radiation patterns for two different positions of the plastic lens. The thick dark lines show the radiation patterns with the lens at the original position, and the thin light lines show the radiation patterns after the lens was rotated by 90°: (a) for the horizontal pair of slots, (b) for the vertical pair of slots. Since the chip was mounted at 45° angle with respect to the horizontal axis, the E-planes and H-planes are as shown.

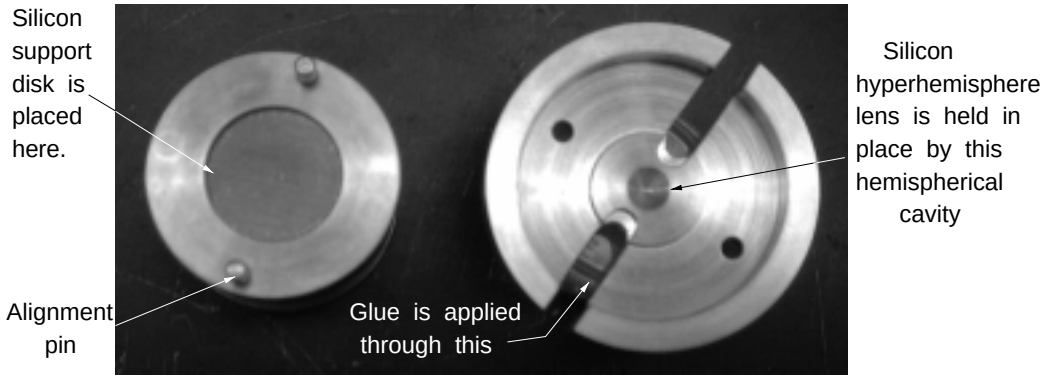

(a)

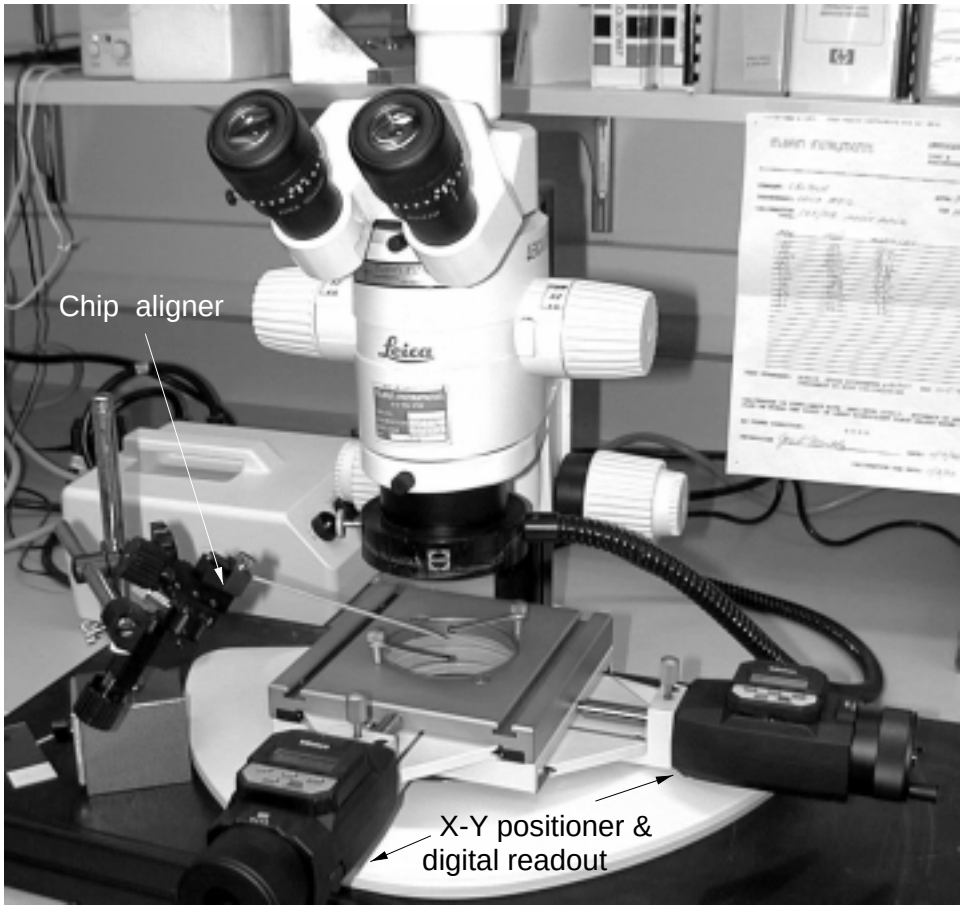

(b)

Figure 3.19 Alignment arrangements of the mixer chip and the hyperhemispherical lens: (a) shows the alignment kit for the hyperhemispherical lens and the silicon support disk, (b) shows the microscope and the associated tools for aligning the mixer chip on the lens.

than what was expected from theoretical calculations; and initially it was thought to be due to the distortion of the shape of the plastic lens at liquid helium temperature (4.2 K). To verify this, the following experiment was carried out. The mixer chip was mounted at 45° angle with respect to the horizontal microstrip line shown in Figure 3.7(b), and a single LO source pumped both the polarizations simultaneously. The co-polarized beam patterns were measured for both the polarizations with the plastic lens mounted the same way as it was for the co-polarization and cross-polarization measurements, described in the previous section. Then the plastic lens was rotated by 90° and the co-polarized beam patterns were measured again for both the polarizations, keeping everything else in the measurement set-up the same. The plots comparing these two different sets of measurements are shown in Figure 3.18, where Figure 3.18(a) is for the horizontal polarization and Figure 3.18(b) is for the vertical polarization. Since the device was mounted at 45° angle, the E-plane and the H-plane for the beams are at 45° angle with respect to the vertical axis. If the beam stretching was due to the plastic lens distortion, then rotating the lens would have changed the beam patterns, because the plastic lens would distort differently for two orthogonal polarizations. However, no noticeable differences were observed between the two sets of measurements, as can be seen from Figure 3.18, eliminating the plastic lens as the possible cause for the beam stretching. A few other experiments were also carried out to check if any other components in the optical path, such as the quartz vacuum window angle, or the LO coupling angle, etc., were causing the beam stretching, and were subsequently eliminated as the possible cause for this effect.

Chip Alignment

The possible cause for the beam stretching was attributed to the chip alignment problem after it was noticed that the deliberate misalignment of the mixer chip on the hyperhemispherical substrate lens had a very pronounced effect on the cross-polarization beam pattern, as shown in Figure 3.17. The proper alignment of the device on the lens, and the lens on the silicon disk, is very important, not only for the dual-polarized receiver described here, but also in other terahertz frequency quasi-

optical receivers [18] where the lens size gets even smaller. To solve this problem, a new chip alignment system is currently being set-up in the laboratory by J. Kawamura [19], and will be described here. Figure 3.19 shows the tools used for aligning the mixer chip, hyperhemispherical lens, and the silicon support disk. Figure 3.19(a) shows the tools used to align and glue the hyperhemispherical lens to the silicon disk. The silicon disk is placed on the disk holder shown on the left, and the hyperhemispherical lens is put on top of the disk. The tool shown on the right in Figure 3.19(a) has a hemispherical hole at the center to hold the lens in place. Two small holes, as shown, mate with the alignment pins, and this set-up holds the lens in place, and then glue [13] is applied through the opening shown in the figure. For aligning the chip on the hyperhemispherical lens, the microscope shown in Figure 3.19(b) is used. The microscope base plate is attached to $X - Y$ positioners with digital readout. The chip is aligned on the disk (the lens is glued to the other side of the disk) by using the fine tip mounted on a 3-D positioner, as shown in the figure. It is believed that this set-up will make the device assembly much easier and faster, and also the alignment will be very close to perfect. The new alignment set-up will be available soon for mounting and aligning mixer chips.

3.3.3 Fourier Transform Spectroscopy

The receiver response as a function of frequency was measured with an FTS system built in-house [20] using the mixer as a direct detector [21]. The FTS operates in a purged nitrogen atmosphere, and has a $50\,\mu$m mylar beamsplitter and a hot-cold source consisting of a variable 300 - 1200 K resistively-heated wire chopped against a 77 K Eccosorb load. Although it is not yet possible to reliably measure the *absolute* response using the FTS, the *shape* of the relative response versus frequency is quite reliable.

Figure 3.20 shows the FTS response for two different polarizations of the receiver, Figure 3.20(a) for the horizontal slots and Figure 3.20(b) for the vertical slots. The device used for this measurement had $1.69\,\mu\text{m}^2$ area junctions and was optimized for

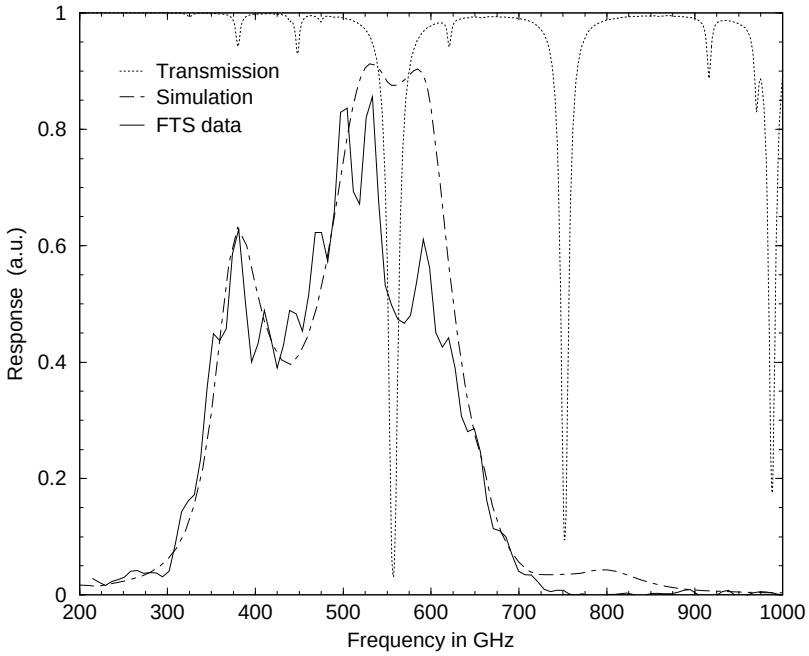

(a)

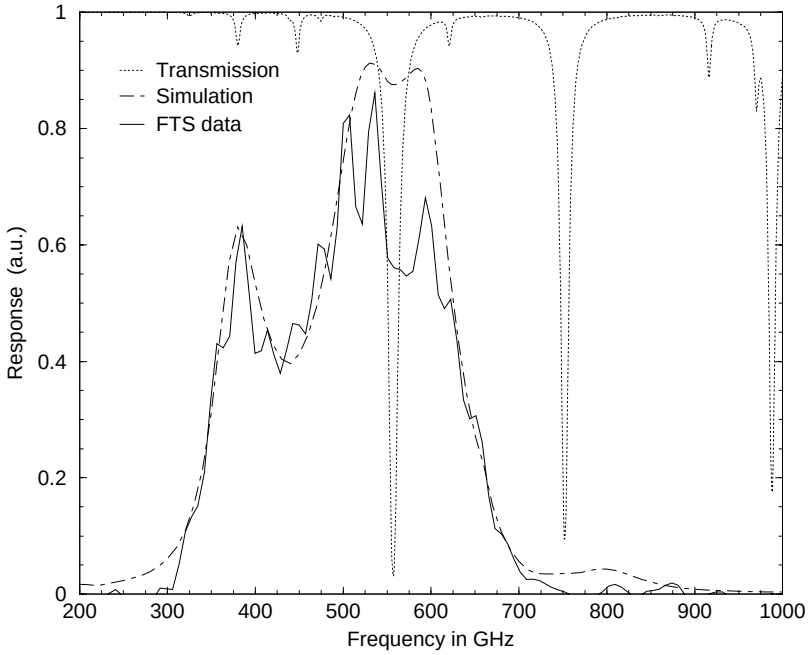

(b)

Figure 3.20 FTS measured response (solid lines), and mixer simulation results (dashed lines): (a) for the horizontal slots and (b) for the vertical slots. The dotted lines show the transmission for the FTS instrument.

550 GHz frequency band. The FTS responses agree well with the Pcircuit simulation results (Appendix A), as can be seen from Figure 3.20, given the non-idealities present in the measurement: strong water absorption lines at 557 GHz and 752 GHz, and Fabry-Perot resonances from the IR filter spaced approximately 50 GHz apart. The FTS response is very similar for both the polarizations, and the peak response was found at 528 GHz. Since the RF junction impedances in heterodyne and in direct detection operation typically differ by less than 10%, the direct FTS measurements can be expected to give relatively accurate indication of the device frequency dependence in heterodyne mode [22], [23]; which means that the best noise temperature for these devices would be around 528 GHz.

3.3.4 Heterodyne Measurements

Receiver noise temperatures were measured using the Y-factor method, first for one polarization at a time, and then with both the polarizations simultaneously active. Room temperature hot load and 77 K cold load is used for the hot-cold load Y-factor measurements. The cryostat temperature was 4.2 K for all the measurements. The noise temperatures reported here are referred to the input of the beamsplitter; *no corrections have been made for beamsplitter or any other optical losses.*

Single-Polarization Measurements

For measuring one polarization at a time, the device was mounted in such a way that the active pair of slots was horizontal with respect to Figure 3.7(b) and only two of the ports were biased at a time (1,2 or 3,4) in series. The correctly polarized LO pumped only four of the eight junctions at a time. Figure 3.21 shows the I-V characteristics for the "horizontal" and the "vertical" pair of slots. The pumped I-V curve clearly shows the photon step around V $\approx$ 1.4 mV, as expected from a 528 GHz LO source ($h\nu/e \approx$ 2.2 mV, since the junctions are in series, the gap voltage is at 5.8 mV and the photon step will appear at 5.8 mV - 2 x 2.2 mV = 1.4 mV). Also shown in Figure 3.21 are the total IF output power in 500 MHz bandwidth when hot

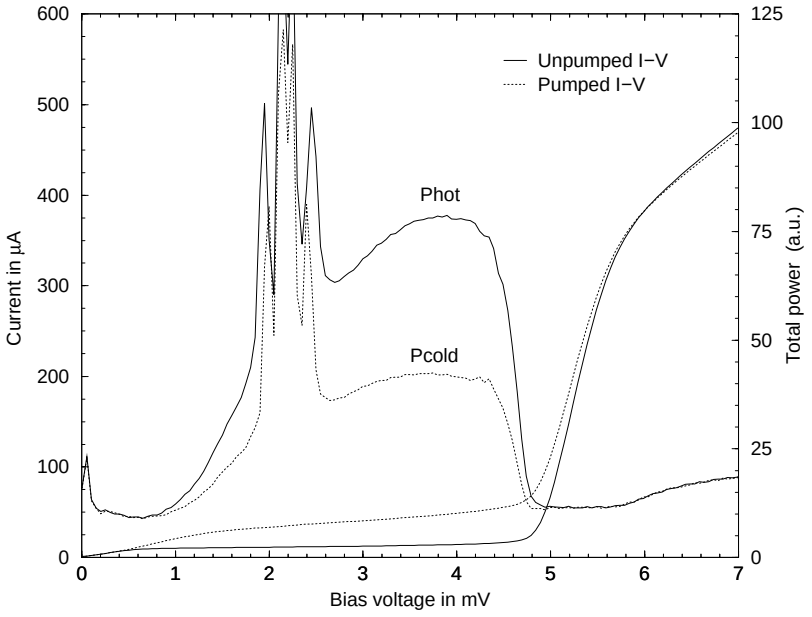

(a)

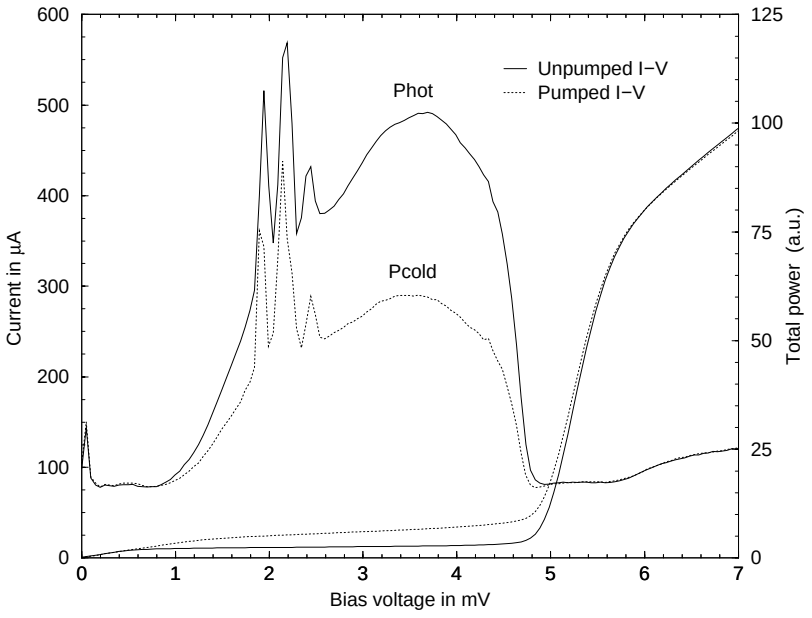

(b)

Figure 3.21 Current and IF output power versus bias voltage at 4.2 K when a single polarization was measured at a time: (a) for the "horizontal" polarization and (b) for the "vertical" polarization. The LO frequency for both polarization was 528 GHz and the measured DSB receiver noise temperatures were 145 K.

and cold loads (absorber at room temperature and at 77 K respectively) are placed at the receiver input. The curves for both the polarizations are relatively smooth, in spite of the fact that four junctions were under a single magnet, indicating good suppression of Josephson noise. At 528 GHz the best DSB noise temperature was measured to be 145 K for both the polarizations. Receiver noise temperature as a function of frequency was also measured from 512 GHz to 580 GHz, and it was found that the noise temperatures closely follow the FTS response, giving close to the best noise temperature near 528 GHz, getting worse near the water absorption line at 552 GHz, and getting better again after 572 GHz range.

Dual-Polarization Measurements

To measure the receiver noise temperature with both the polarizations simultaneously active, the device was mounted at 45° angle with respect to the horizontal microstrip line shown in Figure 3.7(b). As mentioned earlier, the noise temperatures reported here are referred to the input of the beamsplitter; *no corrections have been made for beamsplitter or any other optical losses.* The junctions were biased as shown in Figure 3.10, where the IF outputs of the two different polarizations are isolated from each other by two 47 nH spiral inductors. A single LO source pumped the junctions for both the polarizations simultaneously.

Before proceeding with the dual-polarization noise temperature measurements, it was very important to verify that indeed dual-polarization operation was being observed. Since quite a few wire-bonds connect various circuit elements to each other and to the IF outputs, it is possible to make mistakes in wire-bonding; and inadvertently connect the two polarizations in parallel, giving the same single polarization output signals at both the output ports, instead of dual-polarization outputs. Figure 3.22 shows the the experimental set-up used to confirm dual-polarization operation of the mixer. A wire-grid polarizer was placed in between the beamsplitter input and a cold load (77 K) as shown in the figure. As the grid was rotated about the optical axis, the two IF outputs were observed to increase or decrease independently, depending

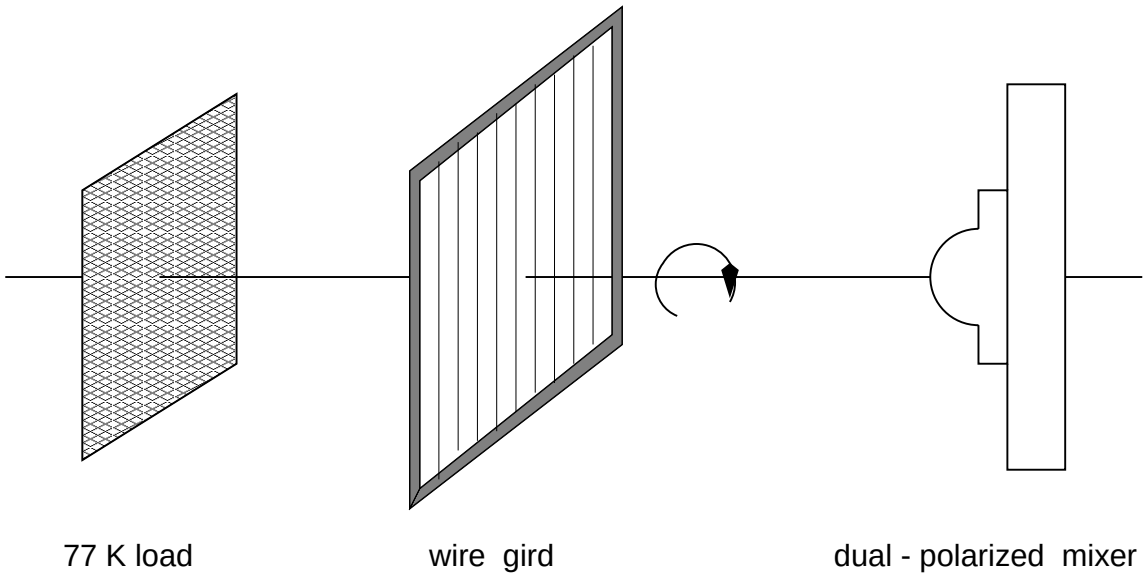

Figure 3.22 Experimental set-up to confirm dual-polarization operation.

on whether the corresponding mixer could *see* the cold load behind the wire-grid. That clearly demonstrated that the mixer was operating in dual polarization mode.

For dual-polarization noise temperature measurements, the LO and the magnet current was adjusted to get a smooth IF output for both the polarizations. Figure 3.23 shows the pumped and the unpumped I-V curves along with the IF outputs in 500 MHz bandwidth at 528 GHz LO frequency when hot and cold loads (absorber at room temperature and at 77 K respectively) are placed at the receiver input. Here again the pumped I-V curve clearly shows the photon step around V $\approx$ 1.4 mV, as expected from a 528 GHz LO source ($h\nu/e \approx$ 2.2 mV). The smooth IF total power outputs for both the polarizations demonstrate adequate suppression of Josephson noise for all the eight SIS junctions using a single magnet. At 528 GHz, nearly identical DSB noise temperature of 115 K were measured for both the polarizations. The receiver noise temperatures as a function of frequency were also measured from 512 GHz to 580 GHz for both the polarizations, and the corresponding plots are shown in Figure 3.24. At frequencies beyond 570 GHz, the available LO power was not sufficient enough to drive the mixer to the optimum operating point, and thus it is believed that lower noise temperatures above 570 GHz could be achieved with higher LO power drive.

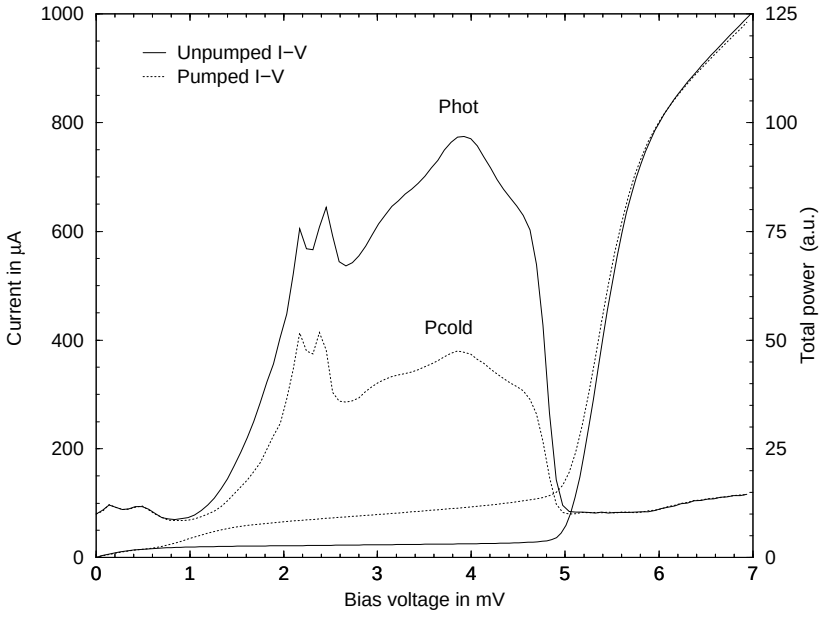

(a)

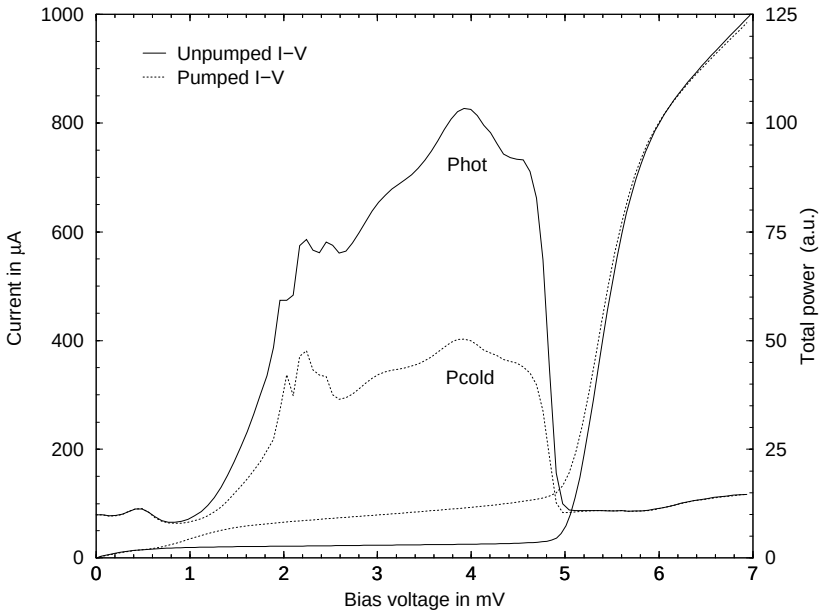

(b)

Figure 3.23 Current and IF output power versus bias voltage at 4.2 K when both the polarizations were measured simultaneously: (a) for the "horizontal" polarization and (b) for the "vertical" polarization. The LO frequency for both polarization was 528 GHz and the measured DSB receiver noise temperatures were 115 K.

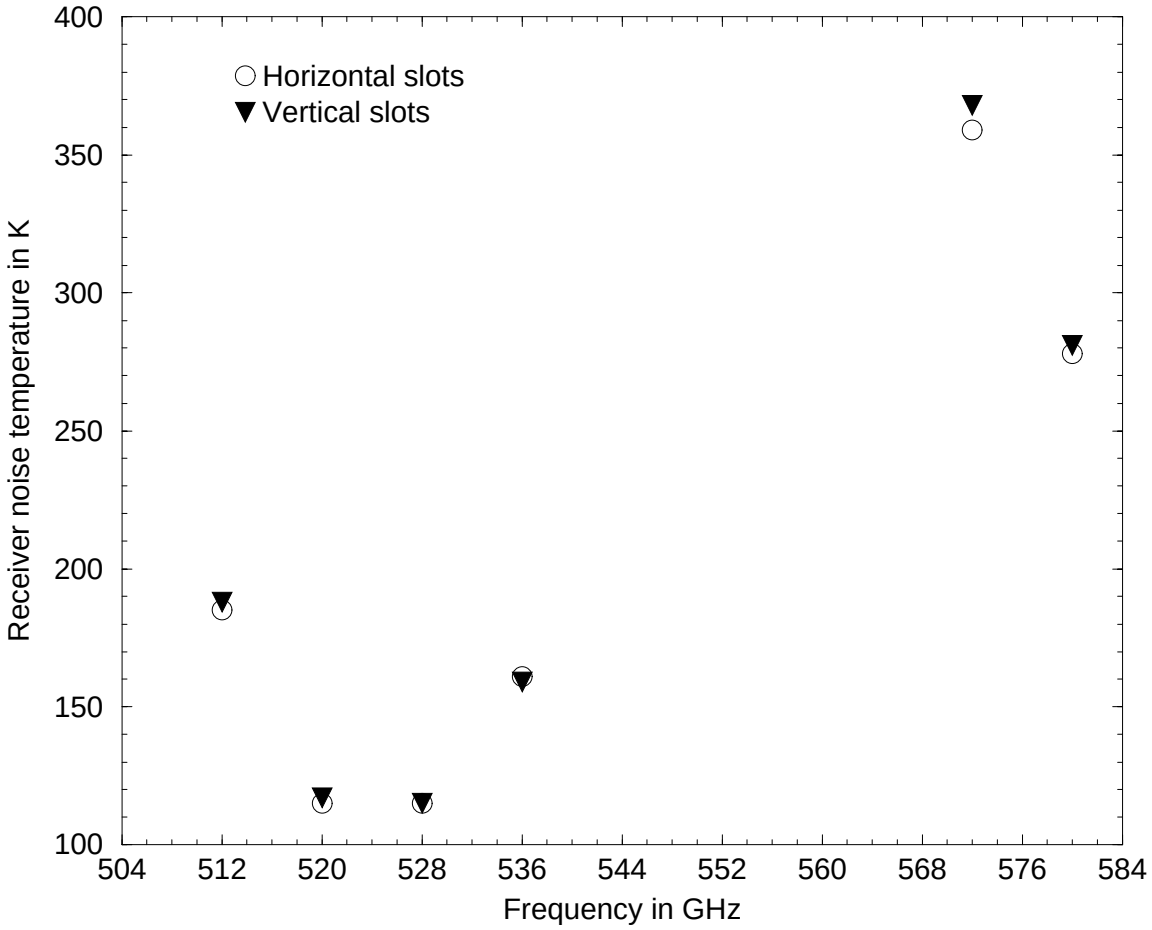

Figure 3.24 Receiver noise temperature as a function of frequency when both the polarizations are operating simultaneously. The circles are for horizontal polarization and the triangles are for vertical polarization.

3.4 Harmonic Balance Simulations Using SuperMix

"SuperMix" is a software library developed at Caltech which can be used to write C++ programs for performing spectral domain harmonic balance simulations of SIS mixers. SuperMix can handle mixer circuits of arbitrary complexity containing any number of superconducting tunnel junctions [24], [25]. SuperMix uses a multi-dimensional Newton-Raphson harmonic balance algorithm to achieve rapid convergence, even when many harmonics are included in the analysis.

3.4.1 Simulation for Single-Polarized and Dual-Polarized Mixer

Using the C++ programs listed in Appendix B, both the single-polarized and the dual-polarized mixers described in this chapter were simulated and compared with the measured results. The first step in the simulation was to match the measured unpumped I-V data to obtain the normal state resistance (R_n) of the junction, by adjusting the voltage and the current offsets of the measured data. Next the Kramers-Kronig transform of the dc I-V curve was obtained. In order to better determine various physical device parameters, it was attempted to simultaneously match the SuperMix predictions to the measured pumped I-V curve and the FTS frequency response. This was done by constructing an error function to quantify the differences between the predicted and the measured quantities, and applying the optimization algorithm in SuperMix to minimize the error function. The parameters which were varied during the optimization include: the junction capacitance, the LO frequency (because the Gunn oscillator was not phase locked), the LO power, dielectric layer (SiO) thickness, SiO dielectric constant (ϵ_r), and the niobium resistivity. The listing of this optimization program (matchivfts.cc) is given in Appendix B. The optimized parameters obtained for the single-polarized and the dual-polarized mixers are shown in Table 3.2. Since the devices used for the single-polarized mixer (device 52[16,7])

Table 3.2 Optimized device parameters obtained from SuperMix simulations

Common parameters for both the single-polarized and the dual-polarized mixers :
Niobium resistivity = 5.127 $\mu\Omega$ cm.
Dielectric layer (SiO) thickness = 2425 Å.
Dielectric constant for SiO (ϵ_r) = 5.68
Single-polarized mixer:
VGAP = 5.3673 mV, Normal state resistance: $R_n = 12.5513\,\Omega$
Capacitance C_j = 153.9 fF, LO frequency = 527 GHz, LO power = 231.2 nW.
Dual-polarized mixer:
VGAP = 5.3902 mV, Normal state resistance: $R_n = 11.5748\,\Omega$
Capacitance C_j = 168 fF, LO frequency = 528.1 GHz, LO power = 435.3 nW.

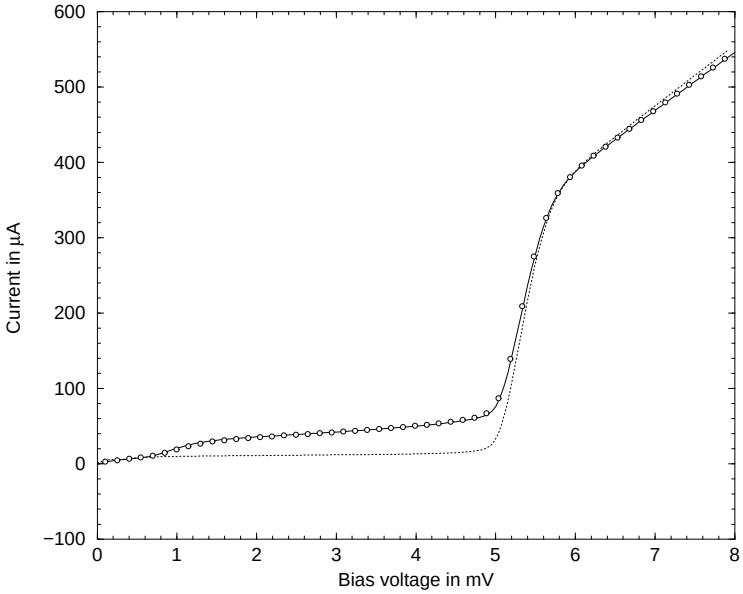

(a)

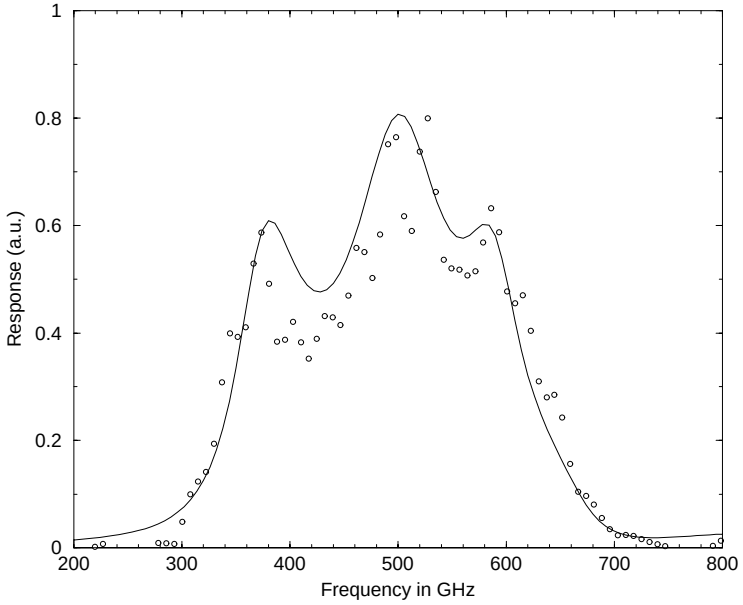

(b)

Figure 3.25 Comparison between the measured and the SuperMix simulation data for the single-polarized mixer: (a) I-V match – the dotted line is the unpumped I-V curve. The circles are the measured pumped I-V data and the solid line is the pumped I-V curve from the SuperMix simulation, (b) FTS match – the circles are the measured FTS data and the solid line shows the data obtained from SuperMix simulation.

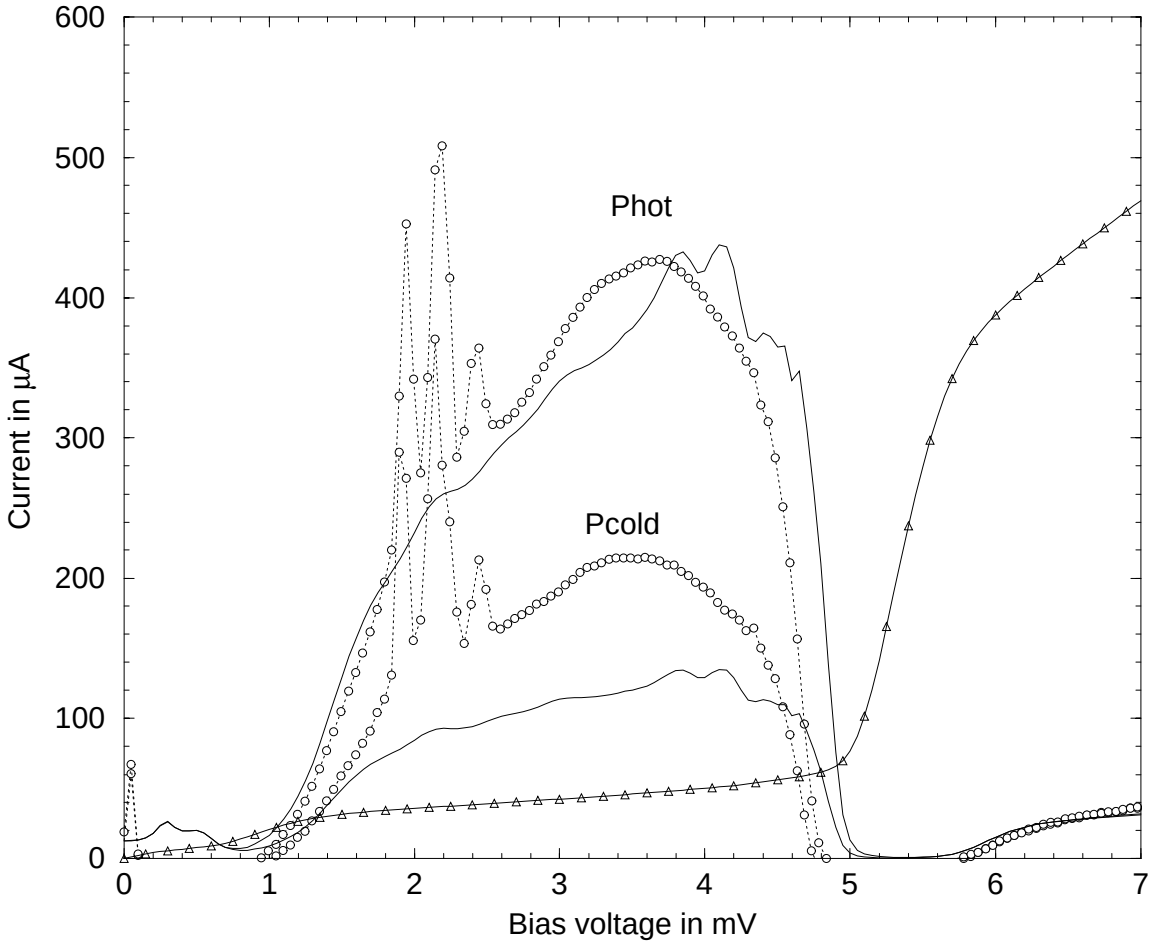

Figure 3.26 Plots showing the measured and the SuperMix simulated hot-cold load data for the single-polarized mixer. Circles with dotted lines are the measured data and the solid lines are the SuperMix simulated data. The measured pumped I-V curve is also shown. The hot-cold load total power curves are in arbitrary units.

and the dual-polarized mixer (device 52[10,7]) were from the same batch, the same physical parameters (except for the normal state resistance and the junction capacitance, which can change due to lithography variations) were used for the SuperMix simulations for both the mixers.

Figure 3.25 shows the measured and the simulated I-V and the FTS data for the single-polarized mixer. From Figure 3.25(a), it can be seen that the pumped I-V match is indeed very good. The FTS match obtained with SuperMix is clearly superior to the original design calculations done with Pcircuit. It should be noted that the

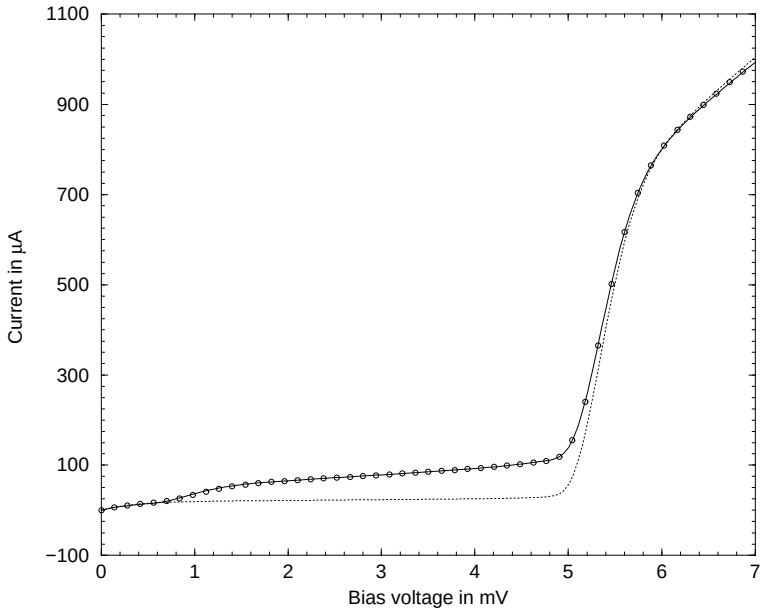

(a)

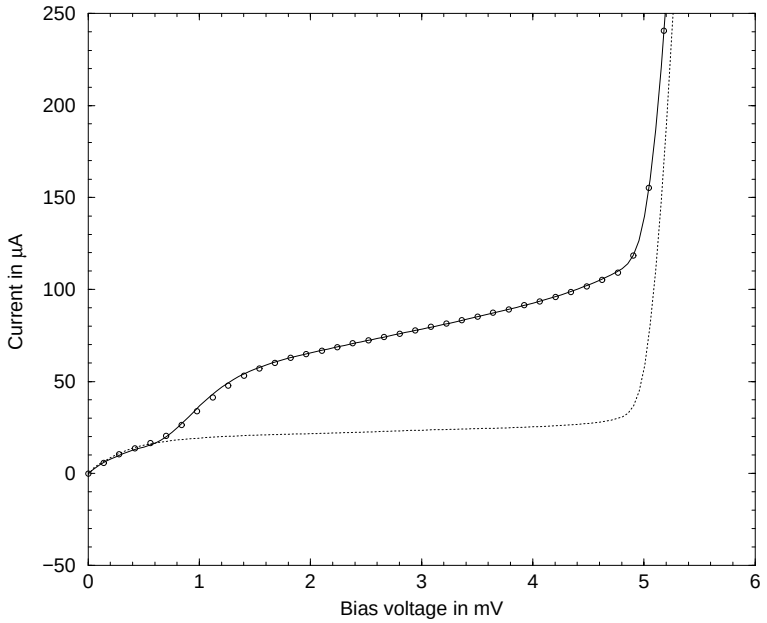

(b)

Figure 3.27 Comparison between the measured and the SuperMix simulation data for the dual-polarized mixer: (a) the dotted line is the unpumped I-V curve. The circles are the measured pumped I-V data and the solid line is the pumped I-V curve obtained from SuperMix simulation, (b) an enlarged view of the I-V data below the gap voltage, showing good match between the measured and the simulated data.

measured FTS response includes a number of non-idealities, such as standing-wave ripples in the optical transmission due to multiple reflections, which are obviously not taken into account in the simulations.

Figure 3.26 shows the measured and the simulated hot-cold load data for the single-polarized mixer. In the SuperMix simulations, no optical loss or thermal noise in the RF path was included, and hence, the Y-factor obtained from the simulation will be better than the measured value. The measured hot-cold load data starts rolling off at a lower bias voltage than the simulated data. The reason for this discrepancy is not clearly understood at this point, but may be due to differences between the actual and assumed IF circuits. Some of the more rapid wiggles in the simulated hot-cold load curves are believed to be produced by discontinuities in the Kramers-Kronig transform of the I-V data (due to measurement noise).

The measured and the simulated I-V curves for the dual-polarized mixer (with all eight junctions operating simultaneously) are shown in Figure 3.27. For this simulation, a three parameter optimization program was used, optimizing the device capacitance, the LO power, and the LO frequency. Figure 3.27(b) shows an enlarged view of the I-V match data below the gap voltage, and clearly indicates a very good match near the gap and also at the photon step.

From these simulation results it can be concluded that one should match both the pumped I-V data and the FTS data simultaneously to obtain reliable device parameters. The simulations also demonstrate that SuperMix would be a very useful tool in the future SIS mixer designs.

3.5 Conclusion

The design, fabrication and measurement of a dual-polarized quasi-optical SIS receiver at 550 GHz using a cross-slot antenna structure on a anti-reflection coated hyperhemispherical silicon lens has been presented with excellent noise temperature

performance (115 K DSB) for both the polarizations. The measured antenna radiation patterns agree reasonably well with theoretical predictions. It has been shown that this receiver has almost identical performance for both the polarizations, and could be very effectively used for submillimeter radio astronomy observations. Also, it should be stressed here that the present device was meant to serve as a prototype to verify the design concepts. The performance (noise temperature, RF bandwidth, etc.) could be improved further using more highly optimized devices. Wider IF bandwidths are possible through the use of a more sophisticated 180° hybrid design, perhaps integrated on-chip. It is also possible to use this device as a balanced mixer, and that will be discussed in the next chapter (chapter 4).

References

[1] J. Zmuidzinas, H. G. LeDuc, J. A. Stern, and S. R. Cypher, "Two-Junction Tuning Circuits for Submillimeter SIS Mixers," *IEEE Trans. Microwave Theory Tech.*, vol. MTT-42, no. 4, pp. 698-706, April 1994.

[2] J. Zmuidzinas, and H. G. LeDuc, "Quasi-Optical Slot Antenna SIS Mixers," *IEEE Trans. Microwave Theory Tech.*, vol. MTT-40, no. 9, pp. 1797-1804, September 1992.

[3] D. C. Mattis, and J. Bardeen, "Theory of Anomalous Skin Effect in Normal and Superconducting Metals," *Phys. Rev.*, vol. 111, pp. 412-417, 1958.

[4] M. Bin, "Low-Noise THz Niobium SIS Mixers," PhD Dissertation, California Institute of Technology, Pasadena, October 1996.

[5] Microwave Design Systems (MDS) version mds.07.10, Hewlett Packard Company, Test and Measurement Organization, Palo Alto, CA.

[6] J. E. Carlstrom, R. L. Plambeck, and D. D. Thornton, "A Continuously Tunable 65-115 GHz Gunn Oscillator," *IEEE Trans. Microwave Theory Tech.*, vol. MTT-33, no. 7, pp. 610-619, July 1985.

[7] N. R. Erickson, "High Efficiency Submillimeter Frequency Multipliers," *1990 IEEE MTT-S Int'l Microwave Symp.*, pp. 1301, June 1990.

[8] *Zitex* - Norton Co. Wayne, NJ 201696-4700.

[9] J. Zmuidzinas, N. G. Ugras, D. Miller, M. C. Gaidis, H. G. LeDuc, and J. A. Stern, "Low-Noise Slot Antenna SIS Mixers," *IEEE Trans. Appl. Superconduct.*, vol. 5, pp. 3053-3056, 1995.

[10] Janos Technology, Inc., HCR #33, Box 25, Route 35, Townshend, VT 05353-7702.

[11] J. W. Kooi, California Institute of Technology, Pasadena, CA, *private communication.*

[12] M. C. Gaidis, H. G. LeDuc, M. Bin, D. Miller, J. A. Stern, and J. Zmuidzinas, "Characterization of Low-Noise Quasi-Optical SIS Mixers for the Submillimeter Band," *IEEE Trans. Microwave Theory Tech.*, vol. MTT-44, no. 7, pp. 1130-1139, July 1996.

[13] Litetak 3761 UV-curing adhesive, by Loctite Corp., Hartford, CT 06106.

[14] Topsil US, 25 Burlington Mall Rd., Suite 300, Burlington, MA 01803.

[15] Rogers Corporation, Microwave Circuit Materials Division, 100 S. Roosevelt Ave., Chandler, AZ 85226.

[16] Microtech, Inc. 1420 Conchester Hwy. Boothwyn, PA 19061.

[17] David A. Miller, "Comparison Between Theory and Measurement of Beam Patterns for Double-Slot Quasi-Optical SIS Mixers," MSEE Dissertation, California State Polytechnic University, Pomona, May 1998.

[18] J. Zmuidzinas, J. W. Kooi, J. Kawamura, G. Chattopadhyay, J. A. Stern, B. Bumble, and H. G. LeDuc, "Development of SIS Mixers for 1 THz," *Proceedings of SPIE: Advanced Technology MMW, Radio, and Terahertz Telescopes*, vol. 3357, pp. 53-61, May 1998.

[19] J. Kawamura, California Institute of Technology, 320-47 Caltech, Pasadena, CA 91125, *private communication*.

[20] M. Bin, D. J. Benford, M. C. Gaidis, T. H. Büttgenbach, J. Zmuidzinas, E. Serabyn, and T. G. Phillips, "A Large Throughput High Resolution Fourier Transform Spectrometer for Submillimeter Applications," *Int. J. IR and MM Waves.*, vol. 20, no. 3, pp. 383-400, March 1999.

[21] Q. Hu, C. A. Mears, P. L. Richards, and F. L. Lloyd, "Measurement of Integrated Tuning Elements for SIS Mixers," *Int. J. IR and MM Waves.*, vol. 9, pp. 303-320, 1988.

[22] J. R. Tucker, and M. J. Feldman, "Quantum Detection at Millimeter Wavelengths," *Rev. Mod. Phys.*, vol. 57, pp. 1055-1113, 1985.

[23] T. H. Büttgenbach, H. G. LeDuc, P. D. Maker, and T. G. Phillips, "A Fixed Tuned Broadband Matching Structure for Submillimeter SIS Receivers," *IEEE Trans. Appl. Superconduct.*, vol. 2, pp. 165-175, 1992.

[24] J. Ward, F. Rice, G. Chattopadhyay, and J. Zmuidzinas, "SuperMix: A Flexible Software Library for High-Frequency Circuit Simulation, Including SIS Mixers and Superconducting Elements," *Proceedings of the Tenth International Symposium on Space Terahertz Technology*, Charlottesville, Virginia, pp. 269–281, March 16–18, 1999.

[25] F. Rice, J. Ward, J. Zmuidzinas, and G. Chattopadhyay, "Fast Harmonic Balance of SIS Mixers with Multiple Junctions and Superconducting Circuits," *Proceedings of the Tenth International Symposium on Space Terahertz Technology*, Charlottesville, Virginia, pp. 282–297, March 16–18, 1999.

Chapter 4

Balanced Mixer

The design and performance of the *first* balanced mixer at submillimeter wavelengths is presented in this chapter. This mixer at 530 GHz utilizes a dual-polarized SIS mixer chip, described in chapter 3, which has a cross-slot antenna on a hyperhemispherical substrate lens with eight SIS junctions connected to the four ports of the antenna, and a 180° lumped element IF hybrid circuit. The local oscillator (LO) and the radio frequency (RF) signal, orthogonal in polarization to each other, are coupled to the mixer using a wire-grid polarizer, and balanced mixer operation is achieved by connecting the four IF outputs in a specific configuration.

4.1 Balanced Mixers at Submillimeter Wavelengths

Balanced mixers suppress Local Oscillator amplitude modulation (AM) noise, have better power handling capabilities, and reject certain spurious responses and signals [1]. At millimeter and submillimeter wavelengths, single-ended mixers are almost always used, and LO injection into the mixer is usually accomplished using a waveguide coupler or an optical beamsplitter. However, due to the low available LO power in this frequency range, the coupling often must be fairly large, -10 dB or greater. Since the LO is usually at room temperature, this results in 30 K or more of thermal noise being injected into the receiver along with the LO. This can be a rather significant contribution to the total receiver noise temperature; modern SIS receivers can have noise temperatures well below 100 K. In contrast, balanced mixers are capable of rejecting the thermal noise incident at the LO port. In addition, balanced mixers make use of *all* of the available LO power, whereas single-ended mixers with beamsplitters or couplers waste $\geq 90\%$ of the LO power. However, no balanced mixer

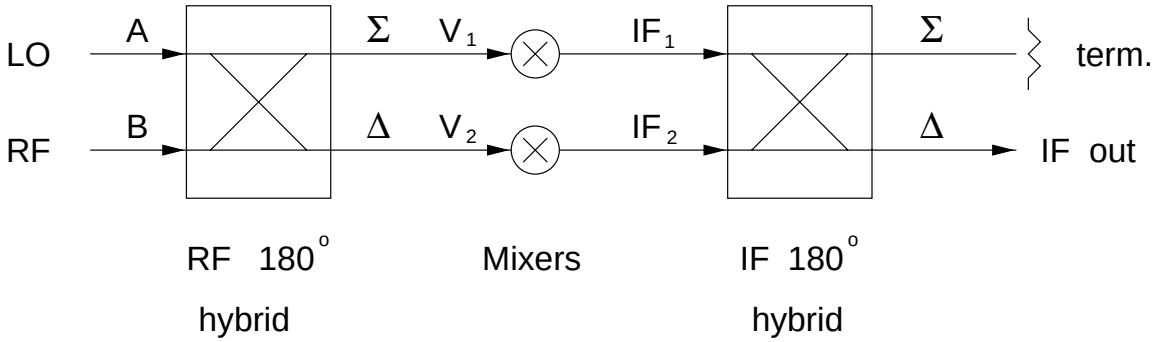

Figure 4.1 Circuit diagram of an ideal balanced mixer which uses 180° RF and IF hybrid circuits.

results have been reported to date at submillimeter wavelengths. In the following sections the design configuration and the results of a balanced mixer at 530 GHz will be presented.

4.1.1 Balanced Mixer Theory and Operation

Figure 4.1 shows the circuit of an ideal balanced mixer which uses a 180° RF hybrid circuit, a pair of mixers, and a 180° IF hybrid circuit. This circuit will be analyzed by writing the LO and the RF signals as

$$\begin{aligned} V_A &= V_{LO}\cos(\omega_{LO}t) + \delta V_A(t) \\ V_B &= \delta V_{sig}(t). \end{aligned} \tag{4.1}$$

Here, it is assumed that the RF signal is just thermal noise, and thermal noise ($\delta V_A(t)$) is also entering the LO port. The voltages $\delta V_A(t)$, $\delta V_{sig}(t)$ corresponding to the thermal noise sources are random, and are characterized by correlation functions,

$$\begin{aligned} &< \delta V_A(t)\,\delta V_A(t-\tau) > = A(\tau) \;\Rightarrow\; \text{LO thermal noise,} \\ &< \delta V_{sig}(t)\,\delta V_{sig}(t-\tau) > = S(\tau) \;\Rightarrow\; \text{signal.} \end{aligned} \tag{4.2}$$

The Fourier transform of these correlation functions, according to the Wiener-Khinchine theorem, are simply the power spectra of the thermal noise sources. For simplicity,

it is assumed that the mixers are ideal square-law detectors, and the two IF outputs will be

$$\begin{aligned} \mathrm{IF}_1 &= \alpha < V_1^2(t) >_{LO} \\ \mathrm{IF}_2 &= \alpha < V_2^2(t) >_{LO} \end{aligned} \tag{4.3}$$

where α is a coefficient related to the conversion loss of the mixer, and the averaging $<>_{LO}$ is meant to filter out the high frequency components, of the order of the LO frequency or higher. Due to the 180° hybrid, the signals entering the mixers will be:

$$\begin{aligned} V_1(t) &= \frac{1}{\sqrt{2}}\Big(V_A(t) + V_B(t)\Big) \\ V_2(t) &= \frac{1}{\sqrt{2}}\Big(-V_A(t) + V_B(t)\Big). \end{aligned} \tag{4.4}$$

The two IF output signals can therefore be written as

$$\begin{aligned} \mathrm{IF}_1 &= \alpha \left[\frac{1}{2} < {V_A}^2(t) >_{LO} + < V_A(t)V_B(t) >_{LO} + \frac{1}{2} < {V_B}^2(t) >_{LO}\right] \\ \mathrm{IF}_2 &= \alpha \left[\frac{1}{2} < {V_A}^2(t) >_{LO} - < V_A(t)V_B(t) >_{LO} + \frac{1}{2} < {V_B}^2(t) >_{LO}\right]. \end{aligned} \tag{4.5}$$

Due to the 180° IF hybrid circuit, the IF output signal $\mathrm{IF}_{\mathrm{out}}$ will be the difference of the two IF outputs, and can be written as

$$\mathrm{IF}_{\mathrm{out}} = \frac{1}{\sqrt{2}}\left(\mathrm{IF}_1 - \mathrm{IF}_2\right) \;=\; \alpha\sqrt{2} < V_A(t)V_B(t) >_{LO}. \tag{4.6}$$

Note that in particular, the $< V_A(t)^2 >_{LO}$ term has dropped out. This term includes the LO thermal noise down converted to the IF:

$$< V_A^2(t) >_{LO} = \frac{1}{2}\,V_{LO}^2 + 2\,V_{LO} < \cos(\omega_{LO}t)\,\delta V_A(t) >_{LO} + < \delta V_A^2(t) >_{LO}. \tag{4.7}$$

The second term in equation (4.7) is the LO thermal noise. The IF output signal $\mathrm{IF_{out}}$, given by the equation (4.6), can be expanded to

$$\begin{aligned}\mathrm{IF_{out}} &= \alpha\sqrt{2} < V_A(t)\, V_B(t) >_{LO} \\ &= \alpha\sqrt{2} < (V_{LO}\, \cos(\omega_{LO}t) + \delta V_A(t))\,.\,\delta V_{sig}(t) >_{LO}.\end{aligned}$$

The thermal noise power is small compared to the LO signal, since $P_{LO} \sim 1\,\mu\mathrm{W}$ while $P_{noise} = kT\Delta\nu \sim 0.5\,\mathrm{nW}$, for $T = 300\,\mathrm{K}$, $\Delta\nu = 100\,\mathrm{GHz}$ – for SIS receivers the bandwidth is around 100 GHz because of the tuning circuits – so $V_{LO} \gg \delta V_A$. Thus, the δV_A term is dropped, which corresponds to mixing of the signal by the noise entering the LO port, and the remaining IF output is just the down-converted signal:

$$\mathrm{IF_{out}} = \alpha\sqrt{2} < V_{LO}\, \cos(\omega_{LO}t)\,.\,\delta V_{sig}(t) >_{LO}. \tag{4.8}$$

From the above equations it is clear that balanced mixers indeed reject the thermal noise injected into the LO port, and would be very useful at submillimeter wavelengths.

4.2 Balanced Mixer Configuration and Design

The dual-polarized mixer chip with cross-slot antenna and four antenna ports, described in chapter 3, lends itself nicely for a balanced mixer design. If the chip is mounted at 45° angle, as was done in the case of dual-polarization heterodyne measurements in section 3.3.4 of chapter 3, and the LO and the RF signals are coupled to the mixer at two orthogonal (vertical and horizontal) polarizations, balanced mixing can be realized by combining the four IF outputs coming out from the four antenna ports in a specific configuration using a 180° IF hybrid circuit. When the LO and the RF signals are applied to the mixer chip at orthogonal polarizations, the signals appearing at each of the mixing elements, connected to the four ports of the antenna, are the combination of the sum and the difference of the LO and the RF signals,

similar to the ideal balanced mixer circuit shown in Figure 4.1. This is the key to the balanced mixer design using the dual-polarization cross-slot mixer chip because now there are two balanced mixer circuits with four mixers, and they are to be connected in a specific configuration to give a single balanced IF output.

4.2.1 Mixer Configuration

The configuration of the balanced mixer using the dual-polarized cross-slot mixer chip is shown in Figure 4.2. Figure 4.2(a) shows the mixer chip orientation with the LO and the RF signals, orthogonal to each other and denoted by L and S respectively. Also shown in the figure are the phases of the LO and RF signals at the four ports of the cross-slot antenna ($+S-L, +S+L$, etc.). At each of the antenna ports, two junction SIS mixing elements, described in chapter 3, are connected. The IF outputs are combined to a single balanced IF output by a 180° hybrid circuit as shown. The equivalent circuit connected to each of the antenna ports is shown in Figure 4.2(b). Two junction tuning circuit, where the junction *separation* dictates the tuning inductance, is shown connected to a two section quarter-wave microstrip transformer which allows a good impedance match between the antenna ($\approx 30\ \Omega$) and the tunnel junctions ($R_n/2 \approx 7\ \Omega$). The LO and the RF port is isolated from the IF and DC port through RF chokes as shown in the figure. The corresponding functional diagram for the balanced mixer is shown in Figure 4.2(c). The LO and the RF signals are incident on the cross-slot antenna and the combined signals with proper phases appear at each of the four antenna ports. The four IF outputs are combined, first two at a time, and finally the two IF outputs are combined in a 180° hybrid circuit. It is to be noted that due to the mandatory series biasing of the mixers (described in section 3.1), the IF currents in the ports which are positively biased will be 180° out of phase compared to the IF currents in the ports which are negatively biased, and that is important in deciding how the different IF signals are to be combined.

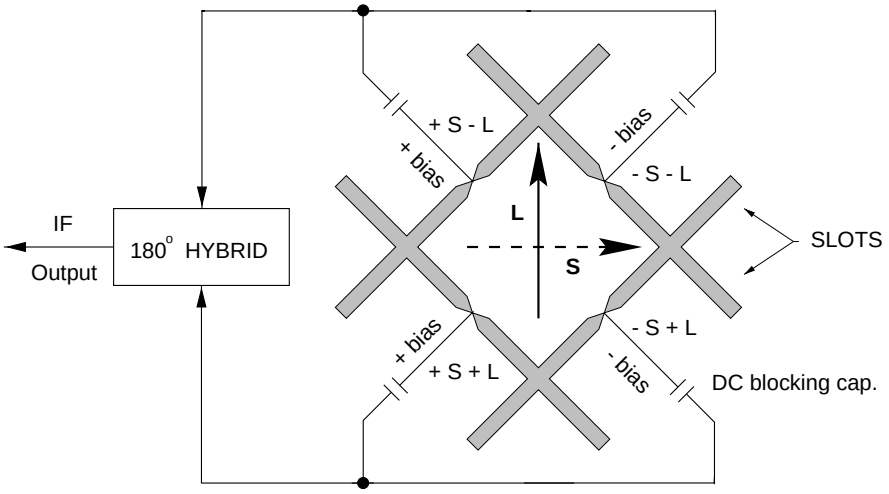

(a)

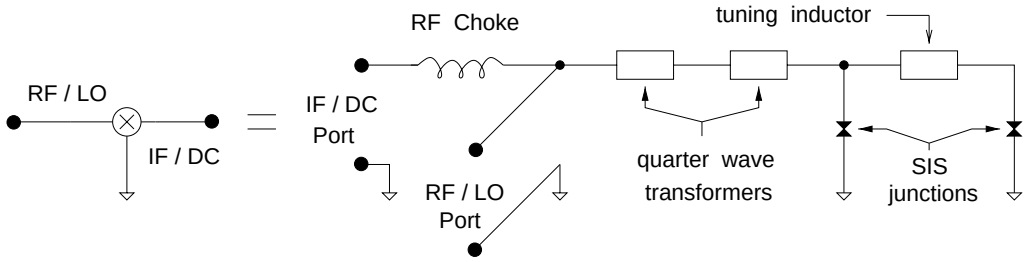

(b)

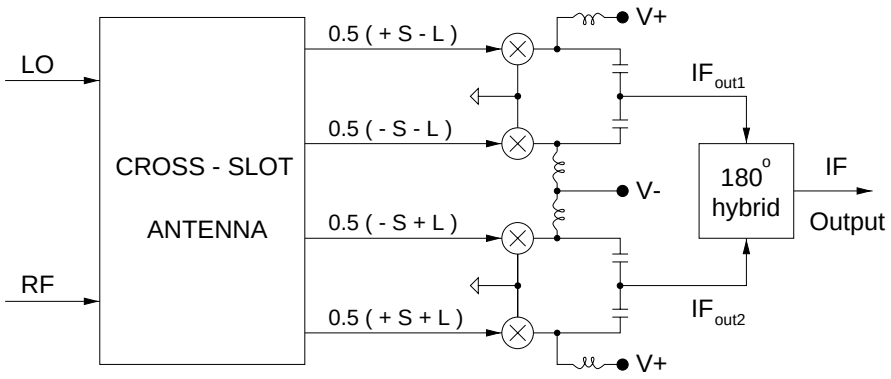

(c)

Figure 4.2 Balanced mixer configuration using the dual-polarized mixer chip: (a) shows the cross-slot antenna with different signals and circuits. LO and RF signals (denoted as L and S respectively) with the phases are shown at the four antenna ports, (b) shows the mixer circuit connected to each of the four antenna ports, (c) shows the corresponding functional diagram.

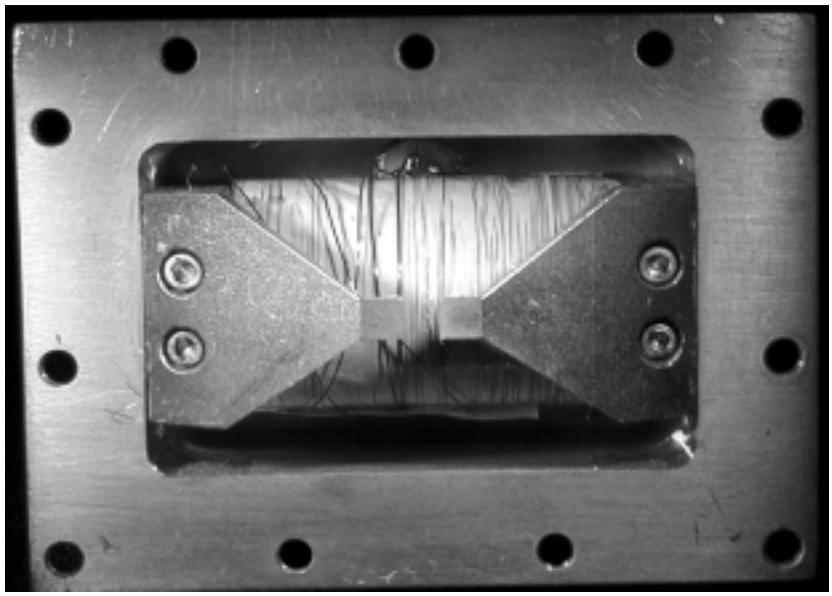

(a)

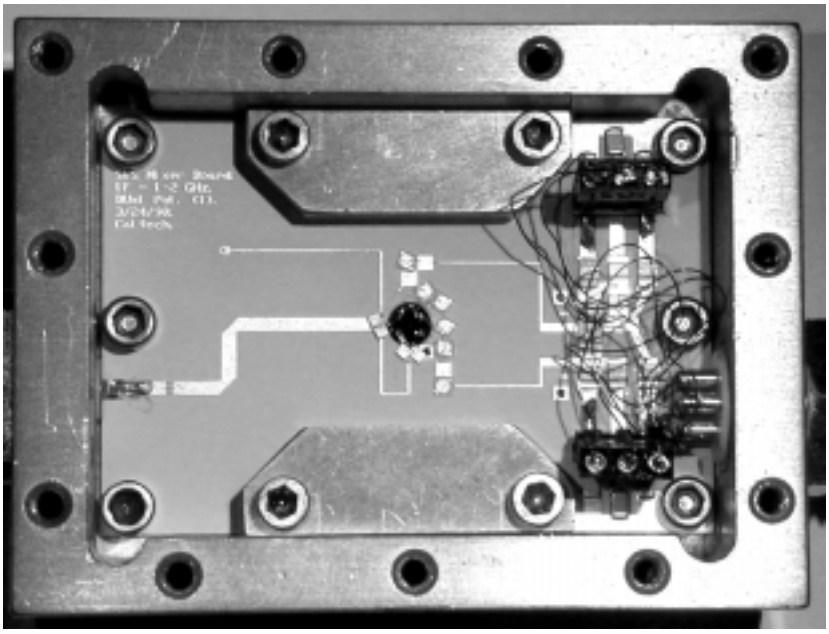

(b)

Figure 4.3 Picture of the disassembled mixer block: (a) shows the magnet housing, (b) shows the bias and IF circuits along with the 180° hybrid, configured for balanced mixer operation. Note that there is only one IF output line in this case, unlike the dual-polarized mixer with two IF outputs for two polarizations.

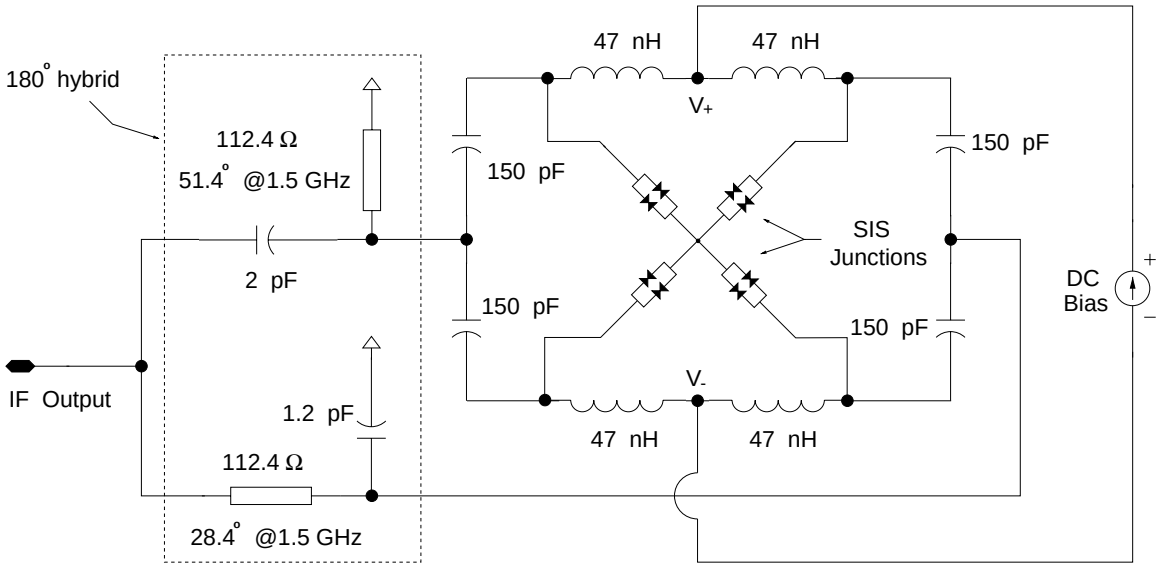

Figure 4.4 The details of the IF and DC bias circuits.

4.2.2 Mixer Assembly, Bias and IF Circuits

For the balanced mixer assembly, existing single polarization mixer block, described in detail by Gaidis *et al.* [2], was used. Figure 4.3 presents a picture of a disassembled balanced mixer block. Figure 4.3(a) shows the magnet housing. The magnet is used to suppress Josephson effects. The construction details of the magnet is described in section 3.2.1 of chapter 3. Figure 4.3(b) shows the picture of the IF circuit board inside the mixer block with DC bias and IF circuit connections, including the lumped element 180° hybrid circuit, and the mixer chip can be seen at the center. The mixer chip was mounted at 45° angle with respect to the horizontal microstrip line shown in Figure 4.3(b). The components used inside the block are similar to the components used for the dual-polarized mixer block, details of which can be seen in Figure 3.8 of chapter 3. The silicon disk, which holds the AR-coated silicon hyperhemispherical lens on one side and the mixer chip on the other, is clamped in the mixer block by a printed circuit board, which is held in place by metal clamps and screws. The circuit board is 0.64 mm thick TMM6 temperature stable microwave laminate from Rogers corporation, with room temperature dielectric constant 6.0 [3]. A multipin Microtech [4] connector is connected at the right side of the mixer block for DC bias

supply and readout connections for the bias voltage and current. The IF outputs are combined in a 180° hybrid circuit and is carried on a 50 Ω microstrip line to the SMA connector on the left.

Figure 4.4 shows the schematic circuit details for the DC bias and IF circuitry on the printed circuit board. A single bias source is used to bias all the eight junctions. The 47 nH spiral inductors, which add $\ll 1\ \Omega$ series resistance at liquid helium temperatures, are glued [5] to the circuit board and isolate the four IF outputs as shown in the figure. The 150 pF DC blocking capacitors are attached to the IF output microstrips with silver-loaded epoxy [6]. The spiral inductors are wire-bonded to the top electrodes of the 150 pF bypass capacitors. The SIS mixer chip sits within a through hole at the center of the board, allowing straightforward wire-bonding of the mixer chip to the biasing network and to the 180° hybrid circuit. The 180° hybrid circuit is realized using high impedance microstrip transmission lines acting as inductors and lumped chip capacitors.

It is to be noted here that the correct orientation of the mixer chip (45° angle with respect to the horizontal axis, as shown in Figure 4.2(a)) inside the mixer block is very important in the operation of the balanced mixer. The isolation of a balanced mixer depends on the amplitude and phase balance of the components [7]. In the case of the balanced mixer described in here, if the mixer chip is not oriented correctly with respect to the LO and the RF signal, there will be both amplitude and phase imbalance, and the isolation will be poor. The mixer chip aligning tools, described in section 3.3.2 of chapter 3, were not available at the time of assembling this mixer, but could be used in future designs.

4.3 Measurements and Results

The balanced mixer measurement set-up is shown in Figure 4.5. The wire-grid polarizer reflects the vertically polarized LO signal and passes the horizontally polarized RF signal. The combined LO and RF signals, polarized orthogonal to each other,

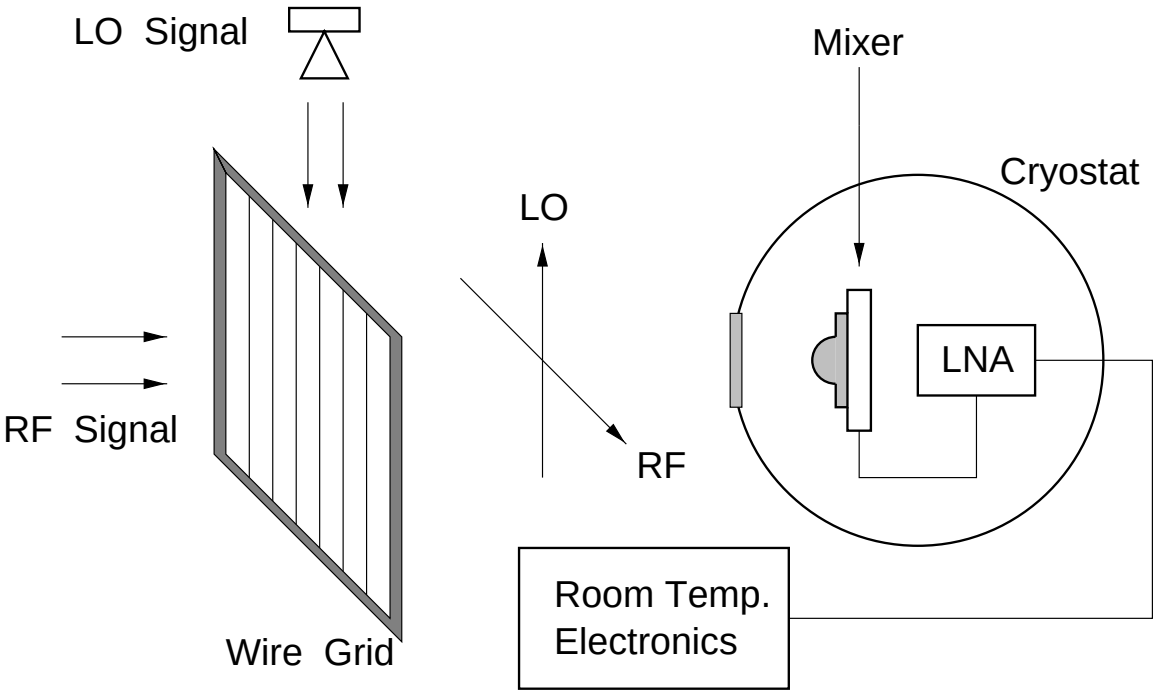

Figure 4.5 Measurement set-up for the balanced mixer. The LO frequency was 528 GHz and the cryostat temperature was 4.2 K.

are coupled to the mixer inside the cryostat after passing through the optics. The cross-slot antenna is oriented as shown in Figure 4.2(a). The balanced IF output is amplified by a 1.0 - 2.0 GHz cooled HEMT low noise amplifier (LNA) with a measured noise temperature of 5 K [8]. The LNA output is sent to room temperature amplifiers and diode detectors for measuring total IF power.

The noise temperature of the receiver was measured by the Y-factor method, using room temperature hot load and 77 K cold load. The cryostat temperature was 4.2 K for the measurements. The noise temperature reported here is referred to the input of the wire-gird; *no corrections have been made for the wire-grid or any other optical losses*. The LO and the magnet current (which suppresses Josephson oscillations) were adjusted to get a smooth IF output and then the noise temperature was measured. Figure 4.6(a) shows the pumped and unpumped I-V curves along with the total IF output power in 500 MHz bandwidth at 528 GHz LO frequency when hot and cold loads are placed at the receiver input. The pumped I-V curve clearly shows

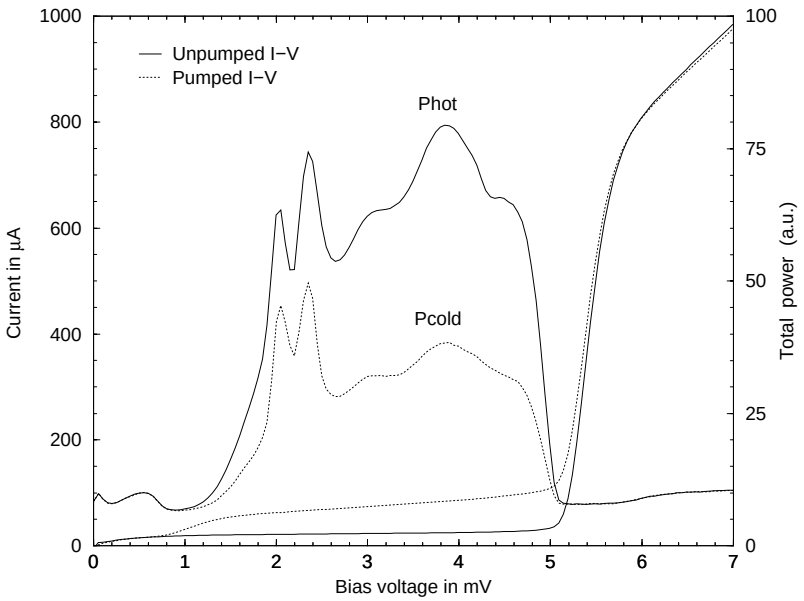

(a)

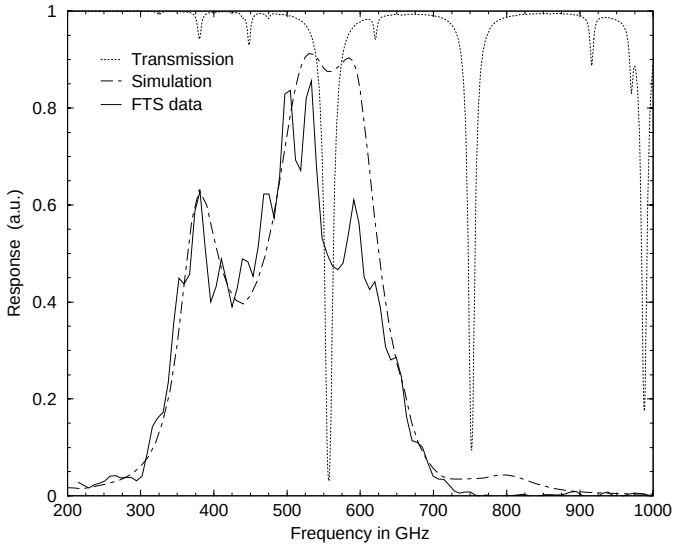

(b)

Figure 4.6 Heterodyne and FTS results: (a) measured bias current and IF output power versus bias voltage at 4.2 K. The gap voltage is at 5.8 mV because two SIS junctions are connected in series. LO frequency for this measurement was 528 GHz and the measured DSB noise temperature was 105 K, (b) measured FTS response is shown by the solid line, and mixer simulation result obtained by using Pcircuit, the program listing of which is given in Appendix A, is shown by the dashed lines. The dotted line show the transmission for the FTS instrument.

the photon step around V $\approx$ 1.4 mV, as expected from a 528 GHz LO source. At 528 GHz, the best noise temperature was measured to be 105 K. For this device, the Fourier transform spectroscopy (FTS) measurement, which measures the receiver response as a function of frequency using the mixer as a direct detector, shows peak response at 528 GHz, as shown in Figure 4.6(b), which means that the best noise temperature measured for this device should be near this frequency [9].

4.4 Balanced Mixer Simulation Using SuperMix

"SuperMix" – is a software library which can be used to write C++ programs to simulate SIS mixers, using full nonlinear Tucker theory [10], [11]. SuperMix programs were written to evaluate the performance of the balanced mixer described in this chapter. The mixer chip used for the balanced mixer design (device 52[13, 7]) is from the same batch as the dual-polarized mixer described in chapter 3 (see section 3.4). Thus, the device parameters used for the dual-polarized mixer simulations are also used for the balanced mixer simulations, except for the normal state resistance and the device capacitance, which can change due to lithography variations. The normal state resistance (R_n) and the gap voltage (Vgap) for the device were obtained from the measured unpumped I-V data using the program unpump.cc, by adjusting the voltage and current offsets. Table 4.1 lists the device parameters and the file names of

Table 4.1 C++ Programs and device parameters used in SuperMix simulations

C ++ programs: makeiv.cc, makeikk.cc, main.balanced.inc.cc, unpump.cc, matchiv.cc, hc.cc, matchbalanced.h
VGAP = 5.3976 mV, Normal state resistance: $R_n = 11.7254\,\Omega$
Junction capacitance C_j = 165 fF
Niobium resistivity = $5.127\,\mu\Omega$ cm.
Dielectric layer (SiO) thickness = 2425 Å.
Dielectric constant for SiO (ϵ_r) = 5.68
Local Oscillator frequency = 525.812 GHz.
Local Oscillator power = 367 nW.

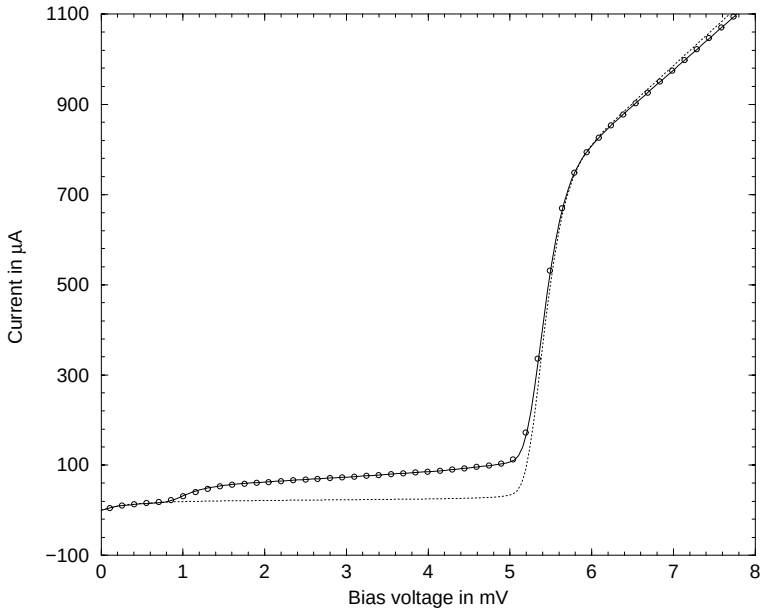

(a)

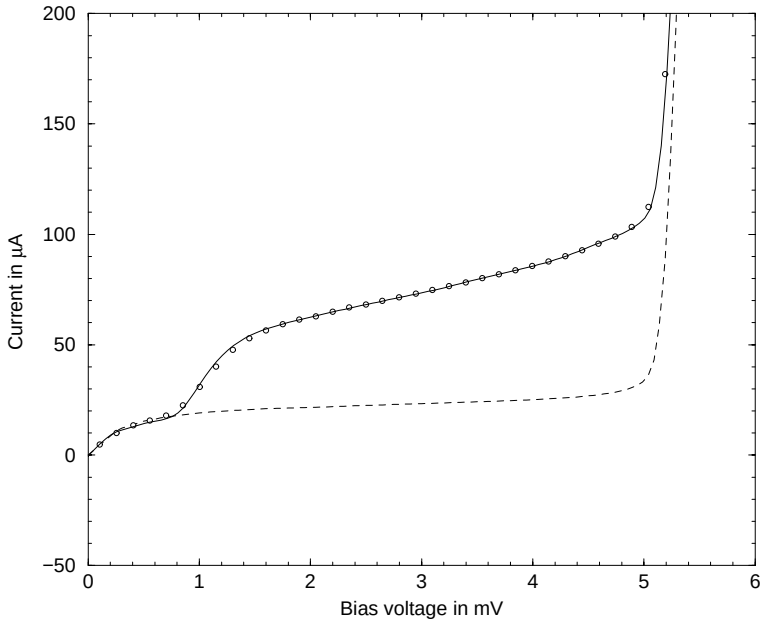

(b)

Figure 4.7 Comparison between the measured and the SuperMix simulation data: (a) the dotted line is the unpumped I-V curve. The circles are the measured pumped I-V data and the solid line is the pumped I-V curve obtained from SuperMix simulation, (b) an enlarged view of the I-V data below the gap voltage, showing good match between the measured and the simulated data.

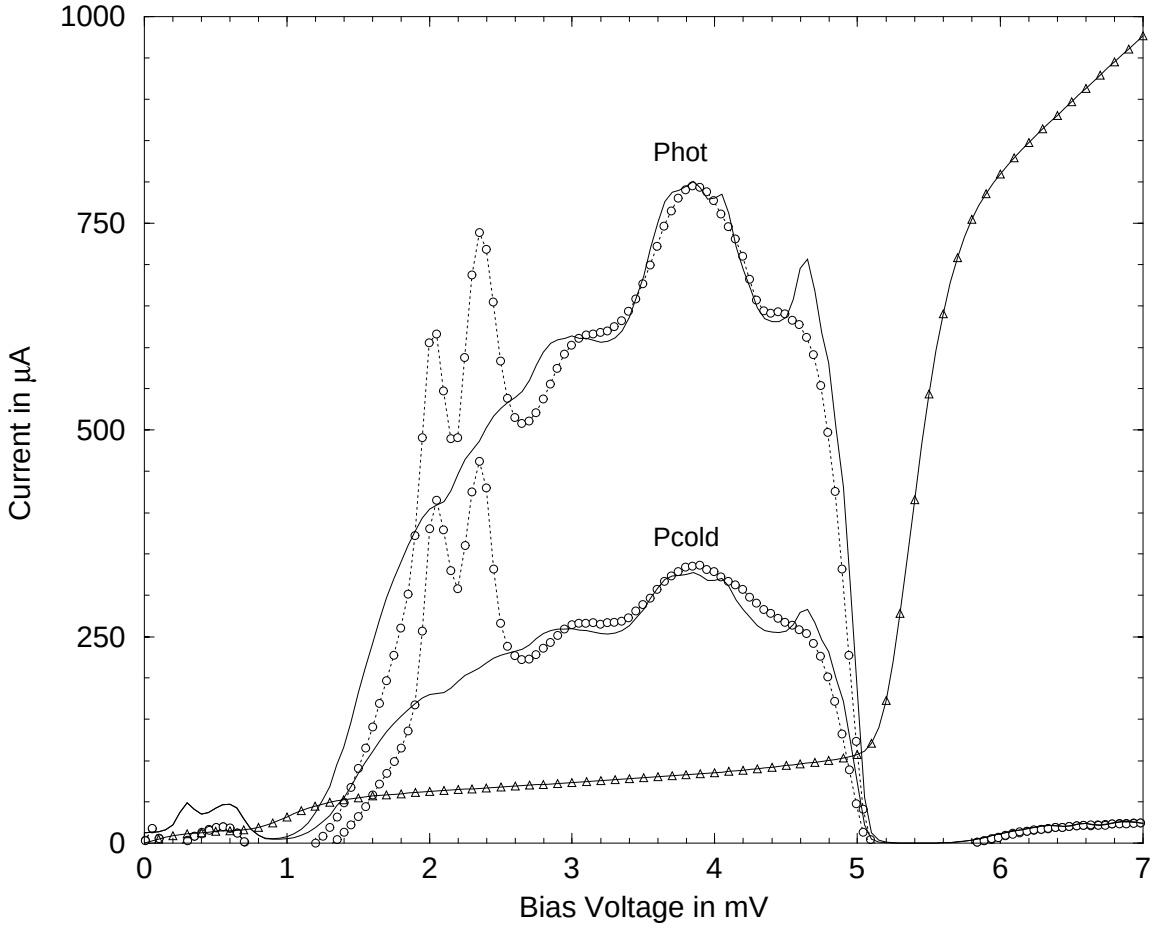

Figure 4.8 Plots showing the measured and the SuperMix simulated hot-cold load data. Circles with dotted lines are the measured data and the solid lines are the SuperMix simulation data. The measured pumped I-V curve is also shown. The hot-cold load total power curves are in arbitrary units. A loss of 0.7 dB (at 300 K) at the RF signal path was included in this simulation.

the C++ programs used for the SuperMix simulations, The C++ program listings are included in Appendix B. The balanced mixer model uses eight SIS junctions with 45 ports and two harmonics for SuperMix simulations. The 180° IF hybrid was included as part of the simulation.

Figure 4.7 shows the comparison between the measured and the SuperMix simulation data for the I-V match. A three parameter optimization program "matchiv.cc" was used to match the measured I-V data. The parameters optimized for this simulation were the junction capacitance, the LO frequency, and the LO power. Figure 4.7(b)

shows an enlarged view of the I-V match below the gap voltage of the junction, which clearly indicates excellent match between the measured and the simulated data. Figure 4.8 shows the measured and the simulated hot-cold load data. For this simulation an optical loss of 0.7 dB at 300 K was included in the model. A loss of 0.7 dB is reasonable, because it includes the quartz vacuum window, the transmission loss of the wire-grid, and the loss due to beam truncation. In addition, there are several sources of cold optical loss, including the 90% cross-slot beam efficiency, the reflection loss at the plastic lens, Zitex IR filter, and the AR-coated silicon lens, which were not accounted for. The LO was kept at 300 K, for the hot-cold load simulations, with the hot and cold load presented at the RF path only. It can be seen from Figure 4.8 that the match between the measured and the simulated data is very good – confirming again that SuperMix is indeed a very powerful tool, capable of simulating a complex mixer structure like the balanced mixer with as many as eight SIS junctions.

4.5 Conclusion

A balanced quasi-optical SIS mixer at 530 GHz using a cross-slot antenna [12] was designed, fabricated and measured. This is the first balanced mixer at this frequency range, and has excellent noise performance (105 K DSB). The RF optics and the IF circuits were not optimized, and it is believed that the performance could be improved further by optimizing the design. Wider IF bandwidth is also possible through the use of a more sophisticated 180° hybrid design, perhaps integrated on-chip.

References

[1] S. A. Maas, *Microwave Mixers*, Second Edition, Artech House, Boston, 1993.

[2] M. C. Gaidis, H. G. LeDuc, M. Bin, D. Miller, J. A. Stern, and J. Zmuidzinas, "Characterization of Low-Noise Quasi-Optical SIS Mixers for the Submillimeter Band," *IEEE Trans. Microwave Theory Tech.*, vol. MTT-44, no. 7, pp. 1130-1139, July 1996.

[3] Rogers Corporation, Microwave Circuit Materials Division, 100 S. Roosevelt Ave., Chandler, AZ 85226.

[4] Microtech, Inc., 1420 Conchester Hwy., Boothwyn, PA 19061.

[5] Litetak 3761 UV-curing adhesive, by Loctite Corp., Hartford, CT 06106.

[6] Janos Technology, Inc., HCR #33, Box 25, Route 35, Townshend, VT 05353-7702.

[7] A. R. Kerr, and S.-K. Pan, "Design of Planar Image Separating and Balanced SIS Mixers," *Proceedings of the Seventh International Symposium on Space Terahertz Technology*, Charlottesville, Virginia, pp. 207-219, March 12-14, 1996.

[8] J. W. Kooi, California Institute of Technology, Pasadena, CA, *private communication.*

[9] G. Chattopadhyay, D. Miller, H. G. LeDuc, and J. Zmuidzinas, "A 550-GHz Dual Polarized Quasi-Optical SIS Mixer," *Proceedings of the Tenth International Symposium on Space Terahertz Technology*, Charlottesville, Virginia, pp. 130-143, March 16-18, 1999.

[10] J. Ward, F. Rice, G. Chattopadhyay, and J. Zmuidzinas, "SuperMix: A Flexible Software Library for High-Frequency Circuit Simulation, Including SIS Mixers and Superconducting Elements," *Proceedings of the Tenth International Symposium on Space Terahertz Technology*, Charlottesville, Virginia, pp. 269–281, March 16–18, 1999.

[11] F. Rice, J. Ward, J. Zmuidzinas, and G. Chattopadhyay, "Fast Harmonic Balance of SIS Mixers with Multiple Junctions and Superconducting Circuits," *Proceedings of the Tenth International Symposium on Space Terahertz Technology*, Charlottesville, Virginia, pp. 282–297, March 16–18, 1999.

[12] G. Chattopadhyay, and J. Zmuidzinas, "A Dual-Polarized Slot Antenna for Millimeter Waves," *IEEE Trans. Antennas Propagat.*, vol. AP-46, no. 5, pp. 736-737, May 1998.

Chapter 5
Ortho-Mode Transducer for the Polatron

This chapter describes the design, simulation, fabrication, and performance of a 96 GHz Ortho-Mode Transducer (OMT) to be used for the *Polatron* - a bolometric receiver with polarization capability. The OMT has low loss, good isolation, moderately broad bandwidth, and its performance closely resembles simulation results.

5.1 The Polatron and the Cosmic Microwave Background (CMB)

The Polatron is a bolometric receiver with polarization capability, designed for use at the Owens Valley Radio Observatory (OVRO) 5.5 meter radio telescope. It will measure the polarization angular power spectrum of the cosmic microwave background (CMB) with high sensitivity and high angular resolution. The polarization of the cosmic microwave background has never been detected [1]. Current models used to describe the intensity variations in the CMB predict a polarization level as high as 10% of the intensity variations. Many experiments, like the Polatron, are being designed and assembled in the hopes of detecting CMB polarization; such measurements will help in understanding the origin of CMB anisotropies and will eventually advance the understanding of the geometry and history of the universe.

The Polatron receiver is designed to project a single 2.5 arc-minute beam on the sky, measuring the difference in signals between two orthogonal linear polarizations. The focal plane of the Polatron, shown in Figure 5.1, consists of a single mode scalar feed horn, an orthomode transducer to separate orthogonal polarizations of the incoming signal, and cooled spider-web bolometers placed in an AC-bridge for stable readout.

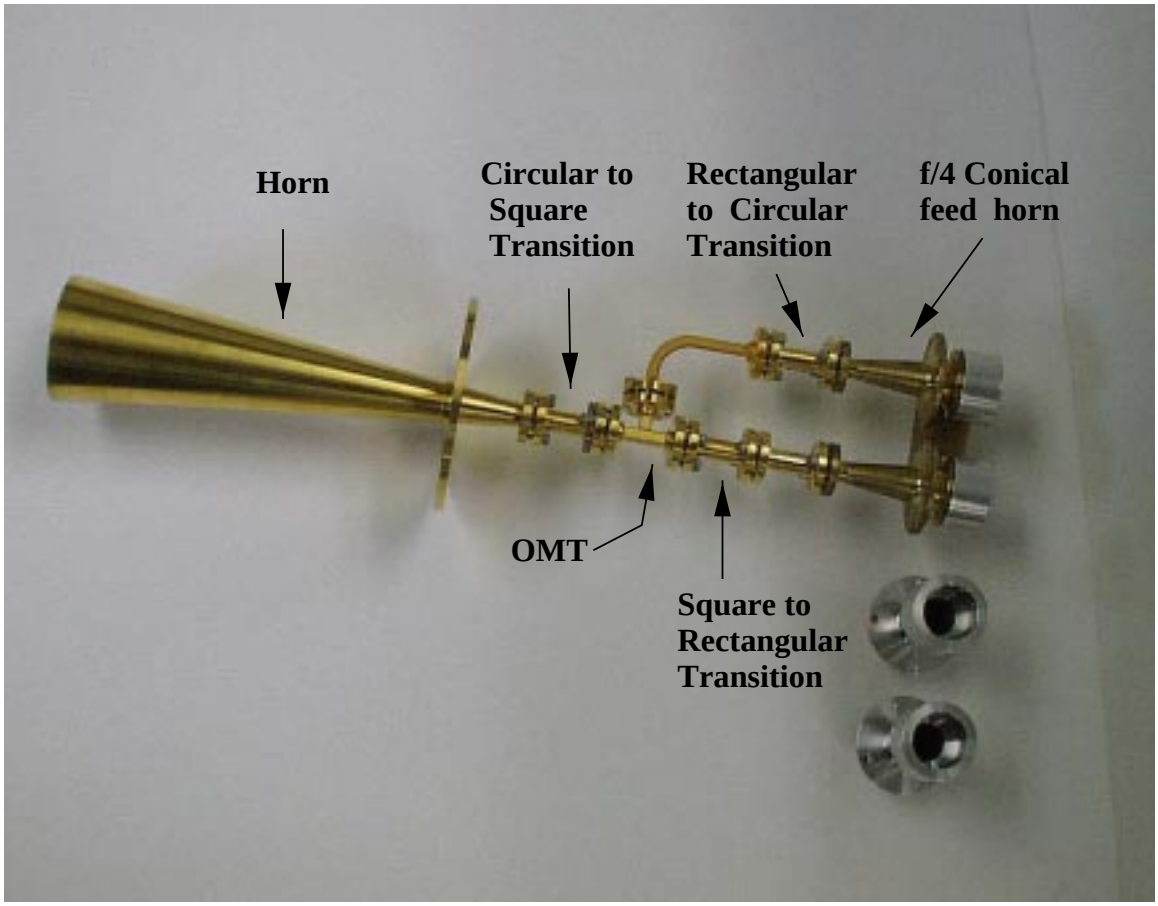

Figure 5.1 A picture of the Polatron focal plane. The OMT outputs are fed to f/4 conical feed horns and lenses which form collimated beams. The beams pass through quasi-optical filters and are coupled to bolometers in integrating cavities through another set of horns and lenses.

The entire instrument will be cooled by a mechanical cryo-cooler, and the bolometers will operate at 250 mK, cooled by a multi-stage sorption fridge. The center frequency of operation of the instrument was chosen at 96 GHz on the basis of the transmission characteristics at the OVRO site, and also to minimize confusion from polarized astrophysical foreground sources, such as galactic synchrotron radiation.

5.2 The Polatron OMT

The focal plane of the Polatron, shown in Figure 5.1, uses an orthomode transducer to separate orthogonal polarizations of the incoming signal within the same frequency

band. Since the primary objective of the Polatron is to measure the polarization angular power spectrum of CMB, the OMT plays a major role in design of the instrument. The OMT specification required for the Polatron depends on a few factors like bandwidth requirement, transmission loss that can be tolerated, isolation between two polarization channels, and the reflection performance; all of these will dictate the choice of the specific OMT design. The following specifications were adopted for the Polatron OMT.

- Center frequency of operation 96 GHz.
- Return loss $\sim$ 20 dB or better over 20% bandwidth for both polarization channels.
- Isolation better than 30 dB.
- Low insertion loss for both polarizations.

5.2.1 OMT Design

There are a few different classes of OMT [2] one could design for the Polatron. The particular choice depends on the performance requirements and fabrication complexity. For the Polatron, the requirement is a moderately broadband OMT with good matching and isolation characteristics, as listed in the previous section. From a performance point of view, a "*class IIb*" OMT described by Bøifot [2] would be ideal. This OMT can be thought of as a turnstile junction [3], where two of the ports are folded parallel to the common port. A thin septum is used to separate the two polarizations, and bring out one polarization through the straight arm. For the other polarization, the septum forms a pair of back-to-back mitered bends which feed the symmetric side arm ports. Pins are used at the side arms for compensating discontinuities. However, at 100 GHz, the fabrication of such a device is extremely difficult, because the waveguide dimensions are small and the tolerances are extremely critical. Commercially available OMTs, like Millitech's W-band OMT [4], offer $5-10\%$

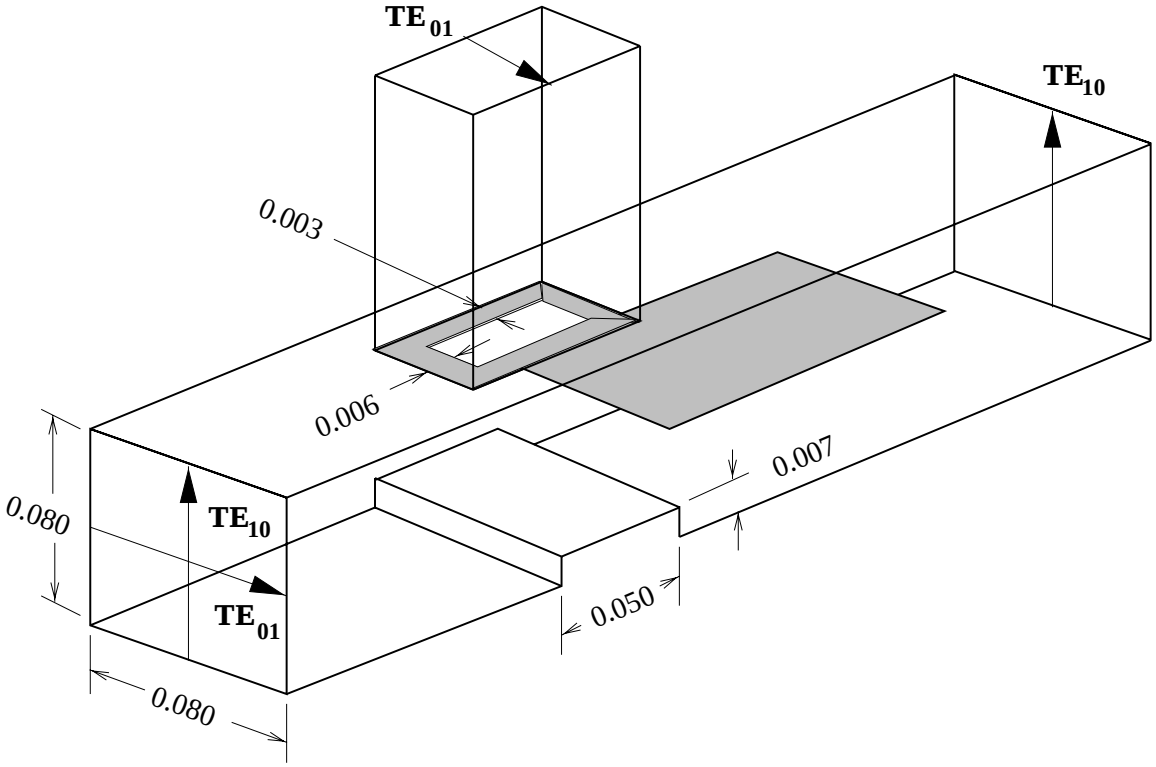

Figure 5.2 Detailed sketch of the Orthomode transducer. The dimensions are in inches.

bandwidth, which is clearly inadequate for the Polatron instrument. Instead, it was decided to design the OMT shown in Figure 5.2, which comes under Bøifot's "*class Ia*" design. The main arm of the OMT has an F-band square guide port with a thin septum insert bisecting the common guide. The septum region is partly overlapped by a rectangular waveguide branching, which is located in the center of a perpendicular side wall of the common waveguide with respect to the septum. The broad dimension of the branching waveguide is in line with the longitudinal axis of the common waveguide. The septum acts as a 3-dB power divider for the dominant $\mathbf{TE_{10}}$ mode input signal. At the end of the septum, the signals recombine in the succeeding stages of the waveguide. The orthogonal $\mathbf{TE_{01}}$ mode is evanescent within the septum region; thus, it is reflected back from the septum and is coupled to the orthogonal side arm waveguide. The side arm branching is inductive-iris coupled for the $\mathbf{TE_{01}}$ mode. The inductive iris yields a smaller rectangular aperture size and thus improves matching properties for the $\mathbf{TE_{10}}$ mode. A capacitive discontinuity in the form of a

small step at the bottom wall of the common guide, opposite to the side arm branch, is used to compensate for the influence of the side arm aperture. A standard square to rectangular stepped waveguide transformer is used at the output of the straight $\mathbf{TE_{10}}$ port.

5.2.2 Simulation and Fabrication

The design parameters for this OMT are the thickness, length, and location of the septum; the thickness and dimensions of the iris; and the width of the capacitive step. Hewlett Packard's High Frequency Structure Simulator (HFSS) [5] was used to simulate and optimize the design. Ideally, the iris and the septum should be as thin as possible; a thickness of 0.001-in (0.025 mm) was chosen for both of them, though a slightly thicker septum will also work for this design. The septum region must possess a nearly constant short circuit reference plane for the $\mathbf{TE_{01}}$ mode within the desired frequency band. The rejection of the $\mathbf{TE_{01}}$ mode across the septum region should exceed a value of 50 dB to avoid any impairment by weakly coupled resonances of the waveguide after the septum [6]. Keeping that in mind and also to avoid making the OMT too long, the septum length was chosen to be 0.150-in (3.81 mm). In the HFSS simulation, all the metals were treated as perfect conductors and under that assumption, the optimum location of the septum was found to be 0.033-in (0.838 mm) away from the center of the side arm rectangular guide. The capacitive step and the iris dimensions are shown in Figure 5.2. The OMT was fabricated by Hi-Tech Microwaves, Inc. [7], from electroformed copper. There is a groove on the side wall of the guide for inserting the septum, which gives some flexibility to fine tune the septum location.

5.3 Measurements and Results

The performance of the OMT was measured at the Jet Propulsion Laboratory [8] with an HP 8510C network analyzer and an F-band head. The network analyzer was calibrated with F-band waveguide TRL calibration standards. A square to rectangu-

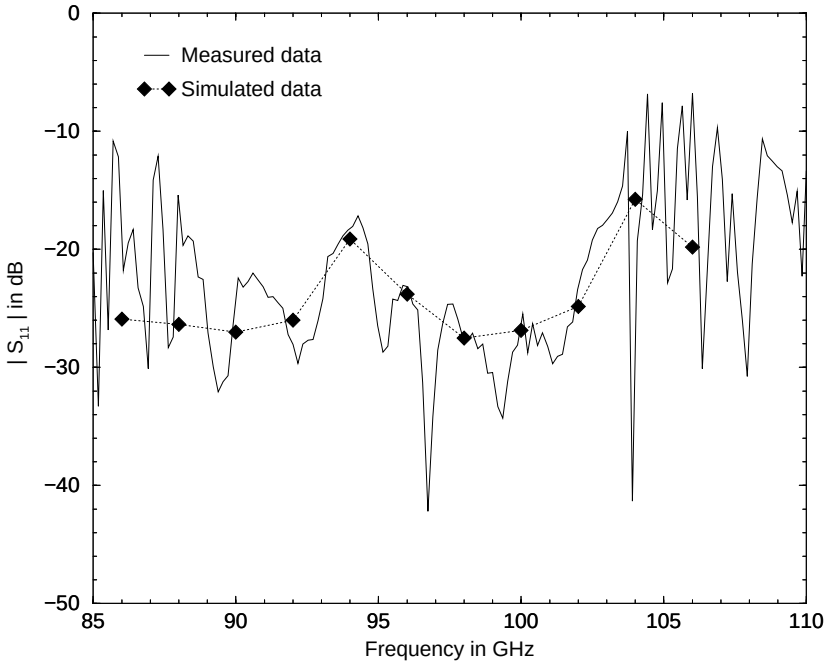

(a)

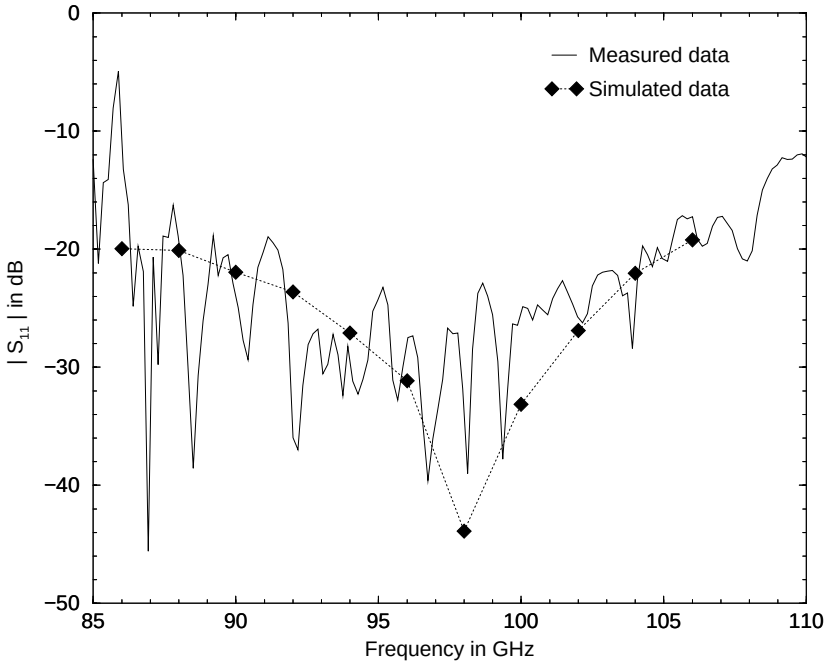

(b)

Figure 5.3 Return loss performance for the OMT: (a) for the $\mathbf{TE_{10}}$ polarization, (b) for the $\mathbf{TE_{01}}$ polarization.

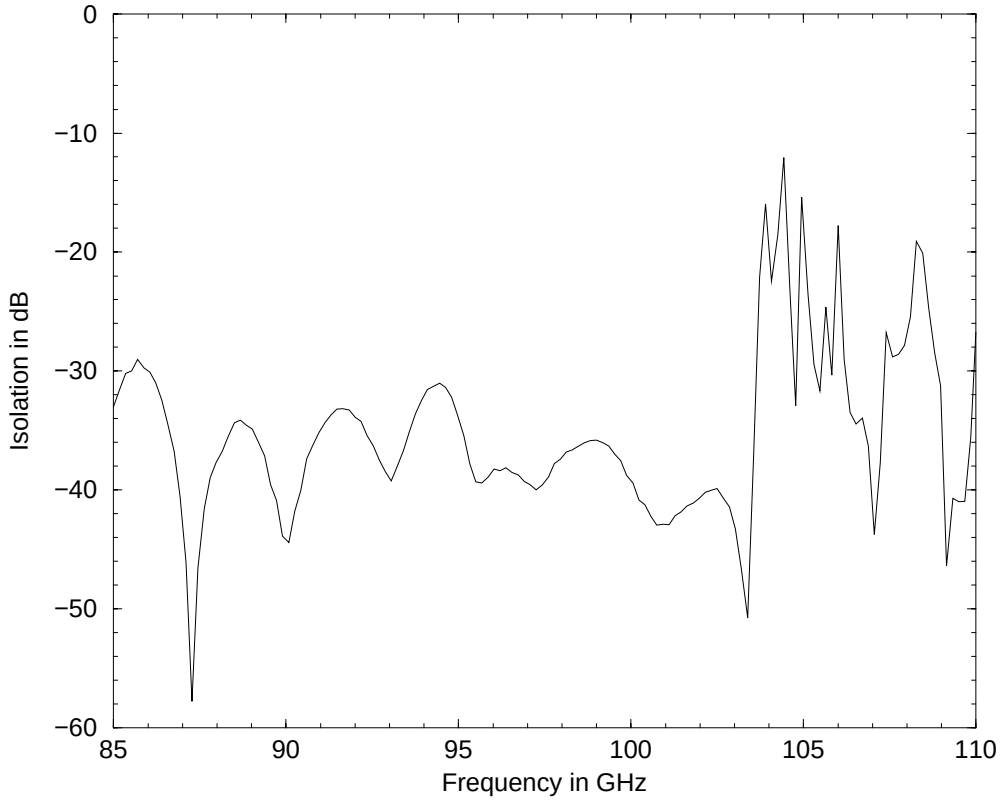

Figure 5.4 Isolation performance of the OMT. The input polarization was for the side arm port ($\mathbf{TE_{01}}$) and the output was measured at the straight port.

lar waveguide transition, which was also designed using HFSS, was used at the input port to mate with the network analyzer head and also to excite the required polarization. The straight port output ($\mathbf{TE_{10}}$ mode) also had a similar square to rectangular transition. The square to rectangular transitions were not part of the calibration process, and hence, the measurement results have the artifacts of the transitions. To obtain optimum performance, the position of the septum was adjusted; the best performance was obtained with the septum at 0.042-in (1.067 mm) away from the center of the side arm guide. Figure 5.3(a) shows the simulated and measured return loss performance for $\mathbf{TE_{10}}$ mode and Figure 5.3(b) shows the same for $\mathbf{TE_{01}}$ mode. Figure 5.4 shows straight port isolation, meaning the input polarization was for the side arm port ($\mathbf{TE_{01}}$ mode) and the output was measured at the straight port. Overall, it was found that the measurements closely follow the simulation results. The OMT has low loss for both polarizations; however, since the OMT will be operated

at cryogenic temperatures, ohmic loss was not a great concern here.

5.4 Conclusion

The orthomode transducer presented here has excellent matching and isolation characteristics over a broadband for both senses of linear polarization. The achieved return loss is less than -20 dB over 20% bandwidth for both polarization channels, and the isolation is better than 30 dB, meeting the requirements for the Polatron instrument.

References

[1] W. Hu, and M. White, "A CMB Polarization Primer," *New Astronomy*, vol. 2, no. 4, pp. 323-344, June 1997.

[2] A.M. Bøifot, "Classification of Ortho-Mode Transducers," *European Trans. Telecommunications and Related Technologies*, vol. 2, no. 5, pp. 503-510, September 1991.

[3] C. G. Montgomery, R. H. Dicke, E. M. Purcell, *Principles of Microwave Circuits*, 1987, IEE Electromagnetic Waves Series, vol. 25, Peter Peregrinus, London, chapter 12. (First published 1948, MIT Radiation Laboratory Series, vol. 8, McGraw-Hill, New York.)

[4] Millitech Corporation, 20 Industrial Drive East, PO Box 109, South Deerfield, MA 01373 USA, chapter 1, page 45, 1995 catalog.

[5] High Frequency Structure Simulator (HFSS), version A.04.01, Hewlett Packard Company, Test and measurement organization, P. O. Box 50637, Palo Alto, CA 94303-9512, USA.

[6] J. Uher, J. Bornemann, and U. Rosenberg, *Waveguide Components for Antenna Feed Systems: Theory and CAD*, 1993, Artech House, Boston, USA, chapter 3.8.

[7] Hi-Tech Microwaves, Inc., 7511 Sears Blvd., Pensacola, FL 32514, USA.

[8] Jet Propulsion Laboratory, *California Institute of Technology*, Pasadena, CA 91109, USA.

Chapter 6

Finline Ortho-Mode Transducer

In this chapter finline orthomode transducers (OMT) are looked into as possible choice for use in dual polarized waveguide receivers at millimeter wavelengths. A finline OMT has low loss, low cross-polarization and good return loss over a full waveguide band. Compared to other broadband OMTs, like Bøifot's "*class IIb*" OMT [1], it is believed that a finline OMT will be easier to fabricate at millimeter wavelengths. In the following sections, a novel finline OMT structure is evaluated for possible use at millimeter wavelengths and scalar model results at X–band are presented.

6.1 Ortho-Mode Transducers at Millimeter Wavelengths

At millimeter wavelengths, waveguide receivers with cryogenically cooled superconductor insulator superconductor (SIS) devices as mixing elements are the most sensitive receivers available today. For even higher sensitivity, millimeter wave receivers require dual-polarization operation. One of the major component for a waveguide based dual-polarization receiver is an orthomode transducer (OMT), which separates orthogonal polarizations within the same frequency band. The OMTs for millimeter wave bands need to be broadband to match the capabilities of available high performance dual polarized broadband corrugated feed horns. Also for dual polarization operation, it is desirable that the cross-polarization introduced by the OMT be less than that introduced by the horn and the related optics. OMT performance desired at millimeter wave receivers are:

- Return loss $\sim$ 20 dB or better over a full waveguide band ($\sim$ 40% bandwidth).

- Isolation better than 40 dB.
- Low cross-polarization, 20 dB or better.

6.1.1 OMT Types and Design Rules

Symmetry is of considerable importance for broadband operation of a waveguide device. Any discontinuity in a waveguide produces higher order modes. Though most of the higher order modes are evanescent modes and do not propagate, they store reactive energy and prevent broadband operation of the device. While designing a broadband device, it is almost impossible to avoid some form of discontinuity in the waveguide, but one can adopt a few simple guidelines to minimize the discontinuities by preventing some higher order mode generation. The bends and curves in the waveguide should possibly be in the E-plane, because, an E-plane bend generates only the even order modes, and hence, is easier to compensate.

An OMT in general will have a common arm where both the polarizations propagate, and then it branches out into two different arms carrying different polarizations. Nearly all kinds of OMTs have some form of symmetry. The bandwidth of the isolation and return loss are essentially determined by the higher order modes generated inside an OMT, and symmetrical and non-symmetrical transitions inside the OMT generate different kinds of modes. Since both polarizations must propagate in the common arm, the higher order mode's cutoff frequencies can be lower than the upper band edge. Most of the modes generated inside an OMT are evanescent and thus do not propagate; however, if excited, the resulting reactance must be compensated. The remaining modes can be controlled by the use of junction symmetry [1], and thus broadband operation can be achieved. For discontinuities which are symmetrical for both the polarizations inside the common arm of the OMT, the dominate mode of the guide can only excite a sum of the following terms:

$$\sum_{m=1}^{\infty}\sum_{n=0}^{\infty}\mathbf{TE}_{(2m-1)2n} \quad \text{and} \quad \sum_{m=1}^{\infty}\sum_{n=1}^{\infty}\mathbf{TM}_{(2m-1)2n}. \tag{6.1}$$

Similarly, if symmetry plane is for the horizontal polarization only, the following modes will be excited inside the OMT:

$$\sum_{m=1}^{\infty}\sum_{n=0}^{\infty}\mathbf{TE}_{m(2n)} \quad \text{and} \quad \sum_{m=1}^{\infty}\sum_{n=1}^{\infty}\mathbf{TM}_{m(2n)}; \tag{6.2}$$

while for a junction whose symmetry plane is for the vertical polarization only, the following modes will be present:

$$\sum_{m=1}^{\infty}\sum_{n=0}^{\infty}\mathbf{TE}_{(2m-1)n} \quad \text{and} \quad \sum_{m=1}^{\infty}\sum_{n=1}^{\infty}\mathbf{TM}_{(2m-1)n}. \tag{6.3}$$

It can be seen from the above equations that in the single mode limit, maintenance of the modal symmetry is the key to the design of a broad band OMT.

In view of the above maximal junction symmetry considerations, the modified turnstile [2] design with four-fold symmetry, described by Gehin and Tourneur [3], will be the obvious choice for a broadband OMT. But this design is complex and will be very difficult to realize at millimeter wavelengths. Another choice for a broadband OMT would be "*class IIb*" OMT described by Bøifot [1]. This OMT can be thought of as a turnstile junction where two ports have been folded parallel to the common port. To adopt this design for millimeter waves will not be easy because of the fabrication difficulties. At higher frequencies, the waveguide dimensions become too small and the tolerances become extremely critical. Wollack [4] reported such an OMT (*class IIb*) for K-band which works very well for the full waveguide band (18-27 GHz), but clearly indicates the machining challenge it will pose to fabricate such a device at higher frequencies. With currently available machining facilities, it is possible to fabricate Bøifot's *class IIb* OMT at frequencies up to W-band, but for frequencies beyond that, it does not appear to be a viable option. At frequencies beyond 100 GHz, one could build a septum OMT [5], which uses a septum to separate two polarizations, but has about 20% bandwidth, which falls short of the performance criteria listed in section 6.1. Instead, a finline OMT, which uses a finline guide to separate one polarization from the other could be a possible choice at millimeter wavelengths

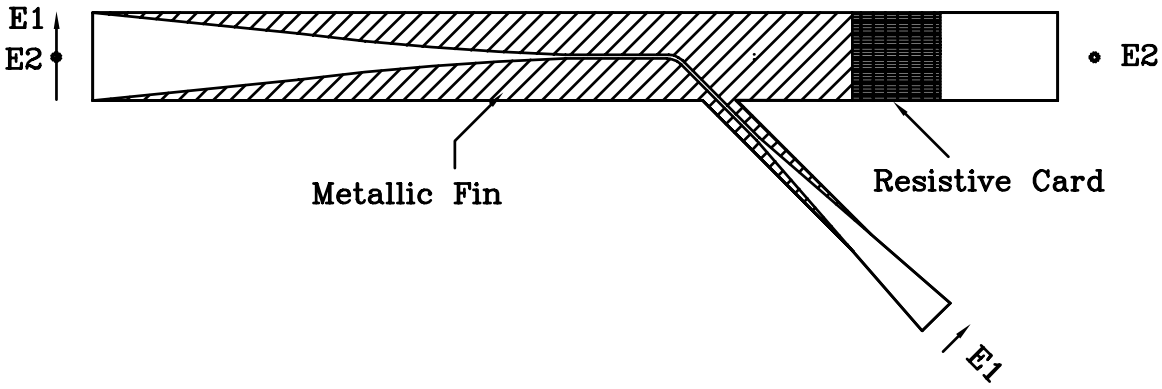

Figure 6.1 Sketch of the finline OMT showing the cross-sectional view.

and is investigated here.

6.2 Finline OMT

The basic concept of a finline OMT was discussed by Robertson [6] in 1956. Skinner *et al.* [7] looked into it in more detail for use on Radio Telescopes. A finline OMT consists of a square or circular waveguide fitted with diametrically opposite thin tapered metallic fins. The dominant mode electric field parallel to the fins is gradually transformed to a finline mode whose energy is essentially confined to the narrow gap between the fins in the center of the waveguide. This energy then can be removed from the waveguide by curving the finline and bringing it out through the side wall of the guide. The mode polarized orthogonal to the fins passes through the guide virtually unperturbed when the fins are sufficiently thin.

A new finline OMT, shown in Figure 6.1, is looked into as a viable design at millimeter wavelengths, and is believed that it could be fabricated at frequencies beyond W-band. The main arm of the OMT is a square waveguide and is assumed to be excited by two orthogonal polarizations **E1** and **E2**. Polarization **E1** is gradually transformed to a finline mode within a very small fin gap. This mode is then taken through a 45° bend and out through a narrow hole in the side wall of the guide. A

further transition from a finline to standard waveguide allows the **E1** polarization to be extracted from the system. The orthogonal polarization **E2** comes out from the other port through a square to rectangular transition. The resistive card is necessary, as in [6], to suppress the excitation of unwanted modes at the termination of the fin. In this design, the finline bend was chosen at 45° instead of 90° to improve cross-polarization performance of the OMT. However, due to the 45° bend, the opening on the side wall is larger and will have undesirable discontinuities for the **E2** polarization. To overcome this, a reduced height guide was used for the side arm to reduce the opening on the side wall. Although the waveguide bend for the **E1** polarization is in the E-plane, and will produce only the even order modes, the higher order modes will be generated at the finline bend and will degrade the cross-polarization performance. The usefulness of the 45° bend with a reduced height guide for the side arm towards improvement in the cross-polarization and isolation performance was supported by the simulations performed using Hewlett Packard's High Frequency Structure Simulator (HFSS) [8]. The side arm has a reduced height to a full height transition so that the OMT output can mate with a standard waveguide.

6.2.1 X–band Scalar Model Fabrication and Results

To evaluate the performance of the OMT, an X–band OMT, whose picture is shown in Figure 6.2, was fabricated. The OMT has a 22.86 mm x 22.86 mm square input guide, and a 6.35 mm high reduced height guide at 45° angle with the main arm. The fin is a 0.76 mm thick metal plate with 0.25 mm gap at the center. The profile of the tapered fins, both in the square waveguide and the reduced height guide, were designed using the equations given in [9], and in [10]; and was verified with HFSS simulations. A 25 mm x 25 mm square piece of $100\,\Omega$/sq. resistive card was used to suppress the resonances. A lower resistance value resistive card will also work fine for this finline OMT. The OMT was machined using aluminum blocks, split across the fin plane. The fins were machined in two separate pieces from aluminum plates, and the resistive card was glued to the fin using silver-loaded epoxy [11].

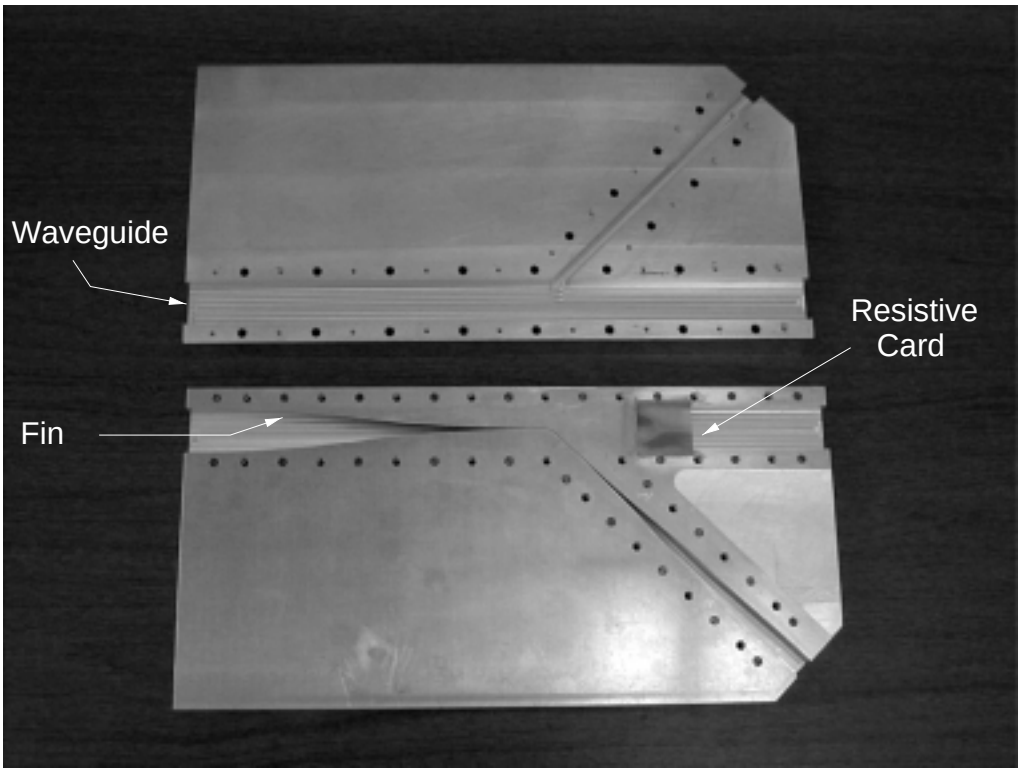

Figure 6.2 A picture of the X–band finline OMT. 22.86 mm X 22.86 mm square waveguide for the input, and 22.86 mm X 10.16 mm standard X–band rectangular waveguides for the outputs were used.

The performance of the OMT was measured with an Anritsu-Wiltron 37200B network analyzer [12] and X–band waveguide to coaxial transitions. The network analyzer was calibrated with X–band waveguide TRM calibration standards. A square to rectangular waveguide transition, designed using HFSS and fabricated with aluminum blocks, were used at the input port to mate with the coaxial to waveguide transitions and also to excite the specific polarization required for a particular measurement. A similar transition was used at the straight output port (**E2**). The square to rectangular transitions were not part of the calibration process, and hence, the measurement results have the artifacts of the transitions.

The return loss measured for the two polarizations **E1** and **E2** were found to be 20 dB or better for the entire waveguide band (Figure 6.3). Isolation between the two ports of the finline OMT was in excess of 40 dB over the band, as can be seen from

Figure 6.4(a). Figure 6.4(b) shows the cross-polarization performance at both the output ports. The bend of the fin in the waveguide generates unwanted higher order modes and that is mainly responsible for the cross-polarization degradation. Though the cross-polarization performance for this OMT is not as good as desired, it is better than 20 dB for the entire band. The insertion loss was found to be less than 0.3 dB for both the polarizations. In the envisioned application, the OMT will be operated at cryogenic temperatures at millimeter wavelengths, and thus, the ohmic loss of the OMT is not a great limitation.

6.2.2 Fabrication at Millimeter Waves

This finline OMT could be fabricated at millimeter wavelengths from electroformed copper with split block along the fin plane. The critical part would be the fabrication

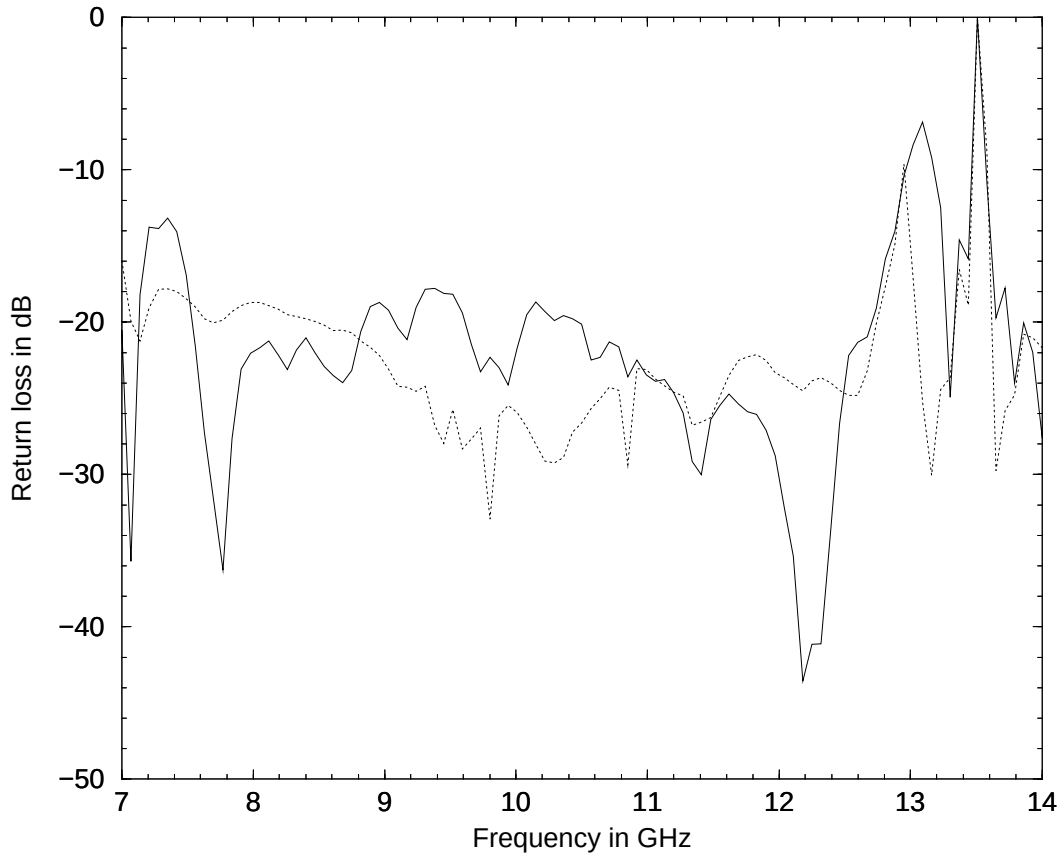

Figure 6.3 Measured return loss of the finline OMT. The solid line is for **E1** polarization and the dotted line is for **E2** polarization.

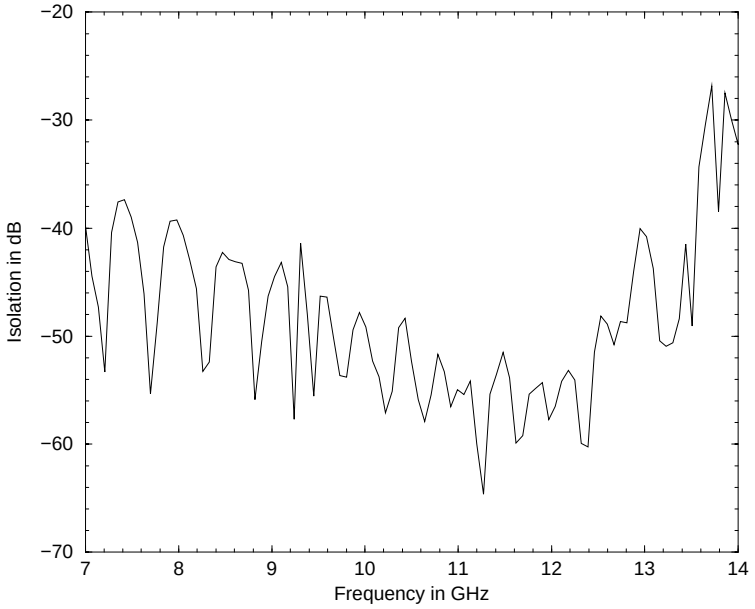

(a)

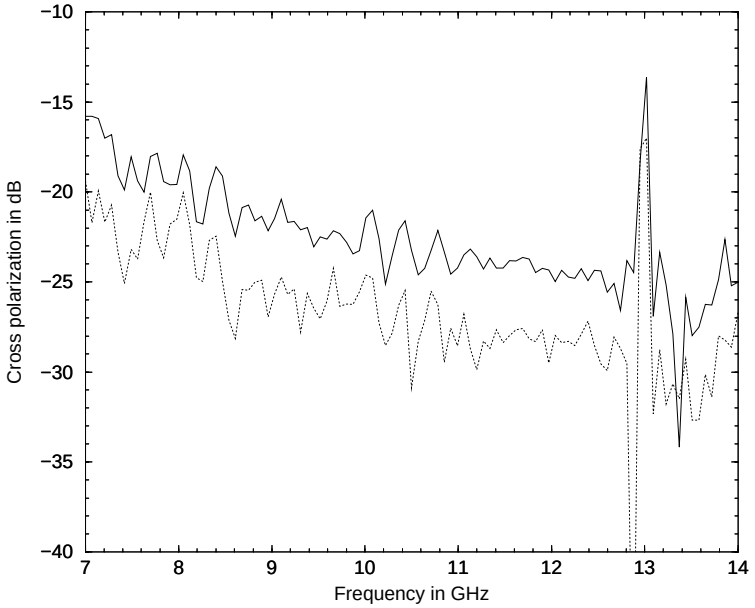

(b)

Figure 6.4 Isolation and cross-polarization measurements: (a) shows the measured isolation between the ports of the finline OMT, (b) shows the measured cross-polarization of the finline OMT. The solid line is for **E1** input polarization when the output is measured at **E2**, and the dotted line is for **E2** input polarization when the output is measured at **E1**.

of the fin and the resistive card. The fin could be fabricated using metal etching technique used by Vahldieck *et al.* [13]. The resistive card could be realized either by masking the fin and evaporating a thin ohmic film on the necessary area, or by using resistive card cut to the size and put in place by silver epoxy or glue.

6.3 Conclusion

The possibility of using a finline OMT at millimeter wavelengths has been evaluated and a new OMT structure has been proposed. The X–band scalar model measurement results show good performance over a full waveguide band. The 45° bend in the finline, instead of the 90° bend, has improved the cross-polarization and return loss performance of the OMT. The fabrication of such a device for frequencies up to 250-300 GHz is thought to be possible using the techniques described in this chapter. For frequencies beyond 300 GHz a dual polarized mixer [14] is much more practical because the fin gap for the finline OMT at these frequencies becomes very narrow and will be difficult to realize.

References

[1] A.M. Bøifot, "Classification of Ortho-Mode Transducers," *European Trans. Telecommunications and Related Technologies*, vol. 2, no. 5, pp. 503-510, September 1991.

[2] C. G. Montgomery, R. H. Dicke, and E. M. Purcell, *Principles of Microwave Circuits*, 1987, IEE Electromagnetic Waves Series, vol. 25, Peter Peregrinus, London, chapter 12. (First published 1948, MIT Radiation Laboratory Series, vol. 8, McGraw-Hill, New York.)

[3] C. Gehin, and J. Tourneur, "A Wideband Polarization Diplexer Device and an Antenna Associated with a Radar or a Counter-Measure," *UK Patent*, GB 2 175 145 A, 1986. 1991.

[4] E. Wollack, "A Full Waveguide Band Orthomode Junction," *Electronics Division Internal Report, National Radio Astronomy Observatory*, no. 303, Green Bank, West Virginia, May 1996.

[5] G. Chattopadhyay, B. Philhour, J. E. Carlstrom, S. Church, A. E. Lange, and J. Zmuidzinas, "A 96-GHz Ortho-Mode Transducer for the Polatron," *IEEE Microwave Guided Wave Lett.*, vol. 8, no. 12, pp. 421-423, December 1998.

[6] S. D. Robertson, "Recent Advances in Finline Circuits," *IRE Tans. Microwave Theory Tech.*, vol. MTT-4, pp. 263-267, 1956.

[7] S. J. Skinner, and G. L. James, "Wide-Band Orthomode Transducers," *IEEE Trans. Microwave Theory Tech.*, vol. MTT-39, no. 2, pp. 294-300, February 1991.

[8] High Frequency Structure Simulator (HFSS), version A.04.01, Hewlett Packard Company, Test and measurement organization, P. O. Box 50637, Palo Alto, CA 94303-9512, USA.

[9] W. J. R. Hoefer, and M. N. Burton, "Closed-Form Expressions for the Parameters of Finned and Ridged Waveguides," *IEEE Trans. Microwave Theory Tech.*, vol. MTT-30, no. 12, pp. 2190-2194, December 1982.

[10] A. Beyer, and I. Wolff, "Finline Taper Design Made Easy," in *1985 IEEE-MTT-S Int. Microwave Symp. Dig.*, pp. 493-496.

[11] Janos Technology, Inc., HCR #33, Box 25, Route 35, Townshend, VT 05353-7702.

[12] Anritsu Company, 1155 East Collins Blvd., Richardson, TX 75081, USA.

[13] R. Vahldieck, J. Bornemann, F. Arndt, and D. Grauerholz, "W-Band Low-Insertion-Loss E-plane Filter," *IEEE Trans. Microwave Theory Tech.*, vol. MTT-32, no. 1, pp. 133-135, January 1984.

[14] G. Chattopadhyay, D. Miller, H. G. LeDuc, and J. Zmuidzinas, "A 550-GHz Dual Polarized Quasi-Optical SIS Mixer," *Proceedings of the Tenth International Symposium of Space Terahertz Technology*, Charlottesville, Virginia, pp. 130-143, March 16-18, 1999.

Chapter 7
Summary

An expert is someone who knows some of the worst mistakes
that can be made in his subject and knows how to avoid them.

- Werner Heisenberg, *Physics and Beyond*

The objective of this thesis was to develop low-noise dual-polarized and balanced receivers and components at millimeter and submillimeter wavelengths, both in waveguide and quasi-optical configurations. This work culminated in the development of a quasi-optical dual-polarized SIS receiver at 550 GHz whose noise performance, for both the polarizations, is close to the best single-polarized SIS receiver available today; a balanced SIS mixer at 530 GHz, which is the *first* balanced mixer at this frequency; and also a moderately broadband septum ortho-mode transducer (OMT) for use in a dual-polarized waveguide receiver for CMB observations. It was also shown in this work that finline OMTs are probably the best available option as a broadband polarization separation component at millimeter wavelengths.

From numerical method of moments calculations, it was shown in chapter 2 that a cross-slot antenna has low impedance – required for matching with low impedance SIS devices, symmetric co-polarized radiation patterns – similar to a twin-slot antenna, and low cross-polarization levels. From the antenna characteristics derived in chapter 2, it became obvious that the cross-slot antenna on a hyperhemispherical silicon lens will be an ideal antenna structure for the development of dual-polarized

SIS receivers at millimeter and submillimeter wavelengths.

A dual-polarized quasi-optical SIS receiver was built at 550 GHz using a cross-slot antenna on a hyperhemispherical silicon lens and niobium trilayer tunnel junctions. The design and fabrication details and the performance of the mixer is described in chapter 3. The cross-slot antenna consists of an orthogonal pair of twin-slots which has four feed points, two for each polarization, and four IF outputs. The outputs are combined in two 180° lumped element/microstrip hybrid circuits to get the two IF outputs for two orthogonal polarizations. A dual-polarized mixer chip was designed and optimized with the integrated planar cross-slot antenna, and was fabricated at the Jet Propulsion Laboratory's (JPL) Center for Space Microelectronics Technology.

The performance of the dual-polarized mixer was excellent. Fourier transform spectrometer (FTS) measurements of the dual-polarized mixer frequency response for both the polarizations show good agreement with computer simulations. The measured co-polarized and cross-polarized antenna radiation patterns for both polarizations also agree well with the theoretical calculations carried out in chapter 2. The noise performance of this quasi-optical dual-polarized SIS mixer was excellent, giving uncorrected receiver noise temperature of 115 K (DSB) at 528 GHz for both the polarizations, which is close to the best reported noise temperature for a single-polarized receiver at this frequency.

In chapter 4, the design and performance of a balanced mixer at 530 GHz is reported. This quasi-optical SIS balanced mixer uses the dual-polarized mixer chip described in chapter 3, a wire-grid polarizer, and a 180° lumped element/microstrip IF hybrid circuit. The wire-grid polarizer is used to couple the LO and the RF signals to the SIS tunnel junctions at two orthogonal polarizations. This balanced mixer is the first of its kind at this frequency, and has excellent noise performance. The uncorrected noise temperature for the balanced mixer was found to be 105 K at 528 GHz.

The bolometric receiver project – the *Polatron* – needed a moderately broadband

ortho-mode transducer (OMT) to separate the two orthogonal polarizations of the incoming signal and measure the polarization angular power spectrum of the cosmic microwave background (CMB). A septum OMT was designed and built at 96 GHz for this purpose, and is described in chapter 5. The measured return loss for the OMT was better than 20 dB over 20% bandwidth for both polarization channels, and the isolation was found to be better than 30 dB, agreeing well with the 3-D finite element simulation results.

Finline OMTs have great potential as broadband polarizers at millimeter wavelengths for use in dual-polarized waveguide receivers. Return loss of 20 dB and isolation better than 40 dB is achievable with such an OMT over a full waveguide band ($\sim$ 40% bandwidth) at millimeter wavelengths. In chapter 6, a novel finline OMT structure is described. A scalar model finline OMT at X–band was fabricated, and the results were found to be very close to design criteria. The design and fabrication issues to realize such a finline OMT at millimeter wavelengths are also discussed in that chapter.

At this point, it won't be improper to say that the research objective that was targeted at the beginning of this thesis was successfully achieved. There are certainly some improvements possible, and the future direction for this research will be discussed now.

Improved noise temperature for the dual-polarized receiver and the balanced mixer is possible by optimization of SIS chip design. The junction parameters of the SIS device (R_nA product) can be optimized to get better performance from these mixers. The IF bandwidth of the dual-polarized receiver was limited to 500 MHz due to the 180° IF hybrid circuit. It is possible to get higher bandwidth by designing the 180° hybrid circuit with higher order lowpass–highpass filter combination. A more sophisticated hybrid design with superconducting spiral inductors, perhaps integrated on the mixer chip, is also possible. For the dual-polarized mixer, existing single-polarized mixer block was used with some modifications. A new mixer block should be fabricated and

the IF circuit board should be re-designed to improve performance. Also, with the new-chip alignment tool operational, the antenna radiation pattern will improve, and the coupling efficiency will be better.

A finline OMT should be fabricated at millimeter wavelength to prove that the design presented in this thesis is indeed the most promising solution at the millimeter wavelengths.

Appendix A: Pcircuit Programs

"Pcircuit" is a linear circuit analysis program with full noise analysis capability [1]. The program also has superconducting transmission line elements to simulate circuits with superconducting components.

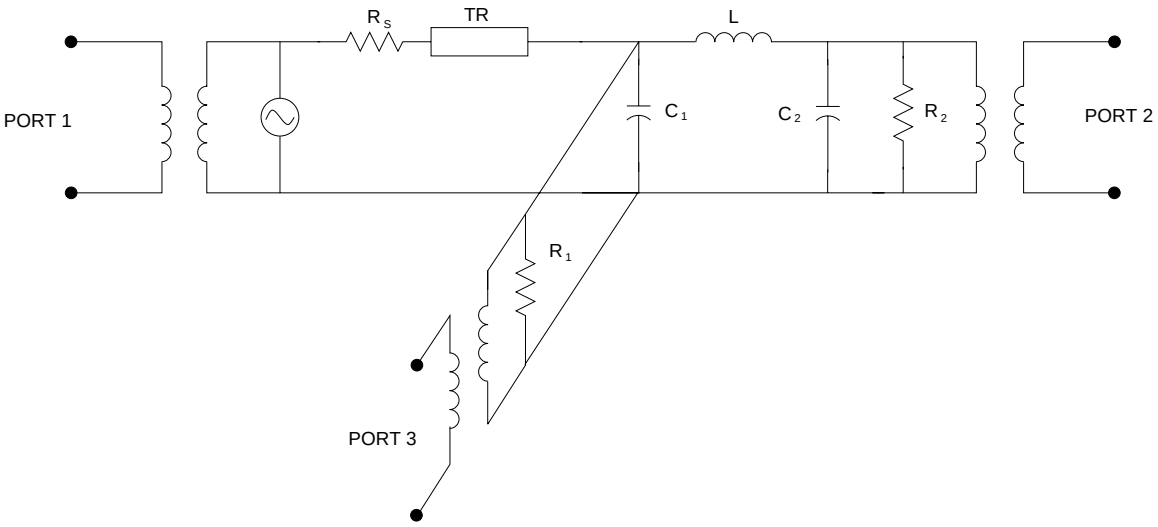

Figure 8.1 Schematic for the simulation set-up for two-junction SIS circuit. The antenna is connected at port 1 with antenna impedance $\mathbf{R_s}$. Two section microstrip transformer is denoted by **TR**, and is used to match the antenna impedance with the junctions, and the tuning inductance is denoted by **L**. Port 2 and port 3 are connected at the two junctions.

The dual-polarized mixer described in this thesis uses two-junction tuning circuits, and the junctions are fed from one end, as described in section 3.1 of chapter 3. To design and simulate such a mixer with Pcircuit is not straightforward. The reason is, since the two junctions are connected through a piece of inductance, the power absorbed by the two junctions will be different, and will vary as a function of fre-

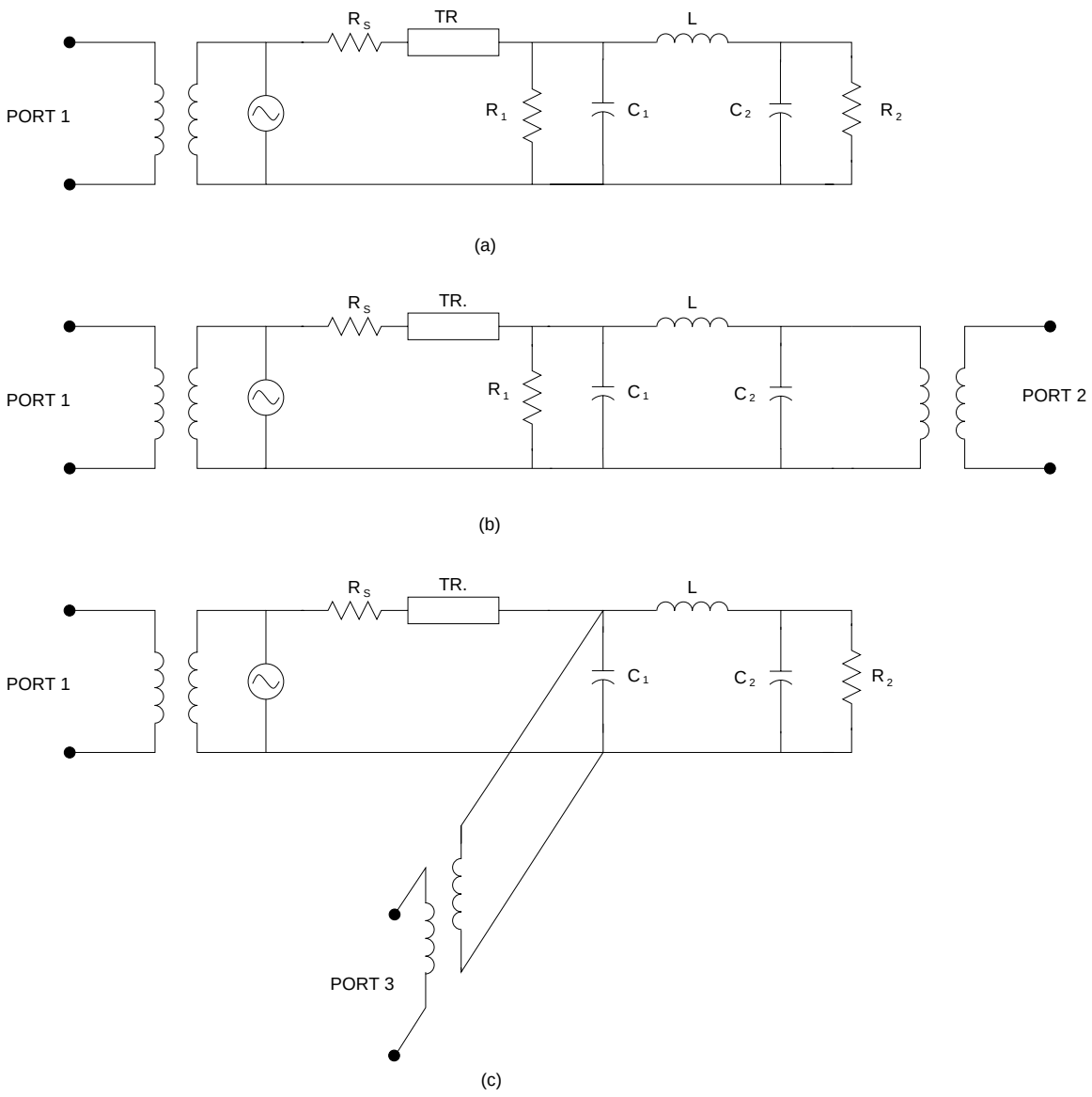

Figure 8.2 Schematics of actual configuration used for Pcircuit simulation: (a) is the circuit set up for one port optimization, (b) and (c) use the optimized parameters obtained from (a) to calculate power coupling to the junctions.

quency. Ideally, a three port circuit should be set up, as shown in the Figure 8.1, with the port 1 as the antenna port, and port 2 and port 3 connected to the two junctions. To optimize this design, the optimization criteria should be set to maximize $|S_{21}|^2 + |S_{31}|^2$. But Pcircuit does not allow more than two ports in a circuit, and also the optimization routine in Pcircuit can not handle such optimization criteria.

To circumvent this problem, the design circuit was set up as shown in Figure 8.2.

First, the circuit is set up as in Figure 8.2(a), where there is only one port connected to the antenna, and it is optimized for minimum input reflection S_{11}. The optimized values obtained from this simulation is used to calculate the power coupled to each of the junctions as function of frequency, using the set up shown in Figure 8.2(a), and Figure 8.2(b). The frequency response of the device was calculated by adding the power coupled to the junctions, $|S_{21}|^2 + |S_{31}|^2$. This simulation procedure is not ideal, but good enough to give sensible results. The Pcircuit programs used for the simulations are listed below.

Program listing for S_{11} optimization using Figure 8.2(a) circuit set up.

```
! Dual-Polarized SIS Mixer Design
! Goutam Chattopadhyay, 10.24.97.
! Frequency 550 GHz
! file: 1_3um_11.ckt
! Circuit layed out for JPL contact aligner.
! Nb/AlOx/Nb junctions with 2000A SiO (single layer), 2500A wiring layer,
! and 2000A Nb ground plane.
! Nominal juntions areas are: 1.2um, 1.3um, 1.4um.
! This circuit is designed for 1.3um x 1.3um with a RnA = 20 Ohm*um^2
! Resistivity of Nb is 5 uOhm-cm.
! Vphase = 0.32c. Tc = 9.2 K, V_gap = 2.9 mV
! This file will optimize the S11 part. The circuit is with one port.
! First, we will read in the antenna impedance file, calculated using
! method of moments analysis.
ONF AA IR ~/sis/p_circuit/dual_pol/Zslot/Zslot.550
XIN BB AA 100000  50.000
! Define surface impedance for ground plane and wiring layer
! Nb: 9.2 K Tc, 5 micro-ohm cm resistivity,  2.9 mV Vgap
! Ground plane is 2000 Angstroms thick.
LSI GP SE 0.2 5. 2.9 0.00001 550. 0.5
! Wiring is 2500 Angstroms thick
LSI WI SE 0.25 5. 2.9 0.00001 550. 0.5
! Use only one layer of 2000A SiO for transformers and tuning inductor.
SUB S1 SE 1. 0. 5.6 0. 0.2
! Define the microstrip two-section transformer, with one short
! microstrip section (2um wide, 1um long) connected between the
! antenna and the microstrip transformer, and a short microstrip
! section (5um wide, 1.5um long) between the transformer and the
! junctions. Inductance width is 5um, and hence, the last section
```

```
! used is 5um wide.
MSL QQ WI GP S1 2.0 1.0
MSL CC WI GP S1 -1.50 (1.5 10.0) -36.64 (5.0 70.0)
MSL DD WI GP S1 -4.17 (1.5 10.0) -44.05 (5.0 70.0)
MSL EE WI GP S1 5.0 1.5
! There is a short microstrip section between the antenna and the
! radial stub.
MSL RS WI GP S1 2.00 1.0
! Now, we shall put the quarter-wave stub. The small radial section
! is simulated in two sections of 3um and 5um widths and 1um long
! each, connecting to 6um width quarter-wave stub.
MSL RT WI GP S1 3 1.0
CAS RS RT
MSL RT WI GP S1 5 1.0
CAS RS RT
MSL RT WI GP S1 6 41.0
CAS RS RT
! The stub is connected to the CPW sections, used for filtering the RF
! signals.
TRL RT SE 53.59 10.03 550 0 0
CAS RS RT
TRL RT SE 80.56 90 550 0 0
CAS RS RT
TRL RT SE 39.2 90 550 0 0
CAS RS RT
! Junction capacitance, 85 fF/sq micron, * (1.3)^2  sq microns =
! 143.65 fF. Here, we will need two capacitances. One will have the
! junction capacitance in parallel with the Rn and the other we will
! have just the capacitance, and the Rn will come with the ideal
! transformer. Junction resistance is 20 Ohm-sq.micron / (1.3)^2
! sq.micron = 11.83 Ohm.
! The first one is the capacitor in parallel with the resistor. There
! will be two such pairs.
! The first pair.
PRC FF PA 11.83 143.85
! The second pair.
PRC HH PA 11.83 143.85
! Tuning inductor. Here, the inductor will be in series. Inductor
! width is 5um.
MSL GG WI GP S1 5.0  -14.65
! Now, we will hook them all up.
! First, we need to deal with the open circuit stub. Calculate the
! input impedance of the stub and convert to series element. CPW lines
! are terminated into 58 Ohms.
PBR RY RS 58.
PTS RZ RY
! Open ended quarter wave stub adds series impedance:
```

```
CAS BB RZ
! Rest of circuit...First the transformer
CAS BB QQ
CAS BB CC
CAS BB DD
CAS BB EE
! Now the parallel combination of resistor and capacitor.
CAS BB FF
! Tuning inductor.
CAS BB GG
! The second capacitor and resistor pair.
CAS BB HH
! One port calculation. Frequency sweep in three separate ranges.
! The first range is from 200 GHz to 490 GHz with 10 GHz step. At
! our frequency of interest, we want sweep with better resolution, and
! the range is 500 GHz to 600 GHz with 5 GHz step, and then from 610 GHz
! to 1000 GHz with 10 GHz step.
PRI BB IR 50.000 100000000.0
END
200 490 10
500 600 5
610 1000 10
END
0.0
0. 0. 0.
1. 0. 0.
0. 0. 0.
END
```

Program listing for calculating power coupled to the second junction S_{21} using Figure 8.2(b) circuit set up.

```
! Dual-Polarized SIS Mixer Design
! Goutam Chattopadhyay, 10.24.97.
! Frequency 550 GHz
! file: 1_3um_a.ckt
! Circuit layed out for JPL contact aligner.
! Nb/AlOx/Nb junctions with 2000A SiO (single layer), 2500A wiring layer,
! and 2000A Nb ground plane.
! Nominal juntions areas are: 1.2um, 1.3um, 1.4um.
! This circuit is designed for 1.3um x 1.3um with a RnA = 20 Ohm*um^2
! Resistivity of Nb is 5 uOhm-cm.
! Vphase = 0.32c. Tc = 9.2 K, V_gap = 2.9 mV
! This file calculates S21, where port 1 is the antenna and port 2 is
! connected at the second junction.
! First, we will read in the antenna impedance file, calculated using
! method of moments analysis.
ONF AA IR ~/sis/p_circuit/dual_pol/Zslot/Zslot.550
```

```
XIN BB AA 100000  50.000
! Define surface impedance for ground plane and wiring layer
! Nb: 9.2 K Tc, 5 micro-ohm cm resistivity,  2.9 mV Vgap
! Ground plane is 2000 Angstroms thick.
LSI GP SE 0.2 5. 2.9 0.00001 550. 0.5
! Wiring is 2500 Angstroms thick
LSI WI SE 0.25 5. 2.9 0.00001 550. 0.5
! Use only one layer of 2000A SiO for transformers and tuning inductor.
SUB S1 SE 1. 0. 5.6 0. 0.2
! Define the microstrip two-section transformer, with one short
! microstrip section (2um wide, 1um long) connected between the
! antenna and the microstrip transformer, and a short microstrip
! section (5um wide, 1.5um long) between the transformer and the
! junctions. Inductance width is 5um, and hence, the last section
! used is 5um wide.
MSL QQ WI GP S1 2.0 1.0
MSL CC WI GP S1 -1.50 (1.5 10.0) -36.64 (5.0 70.0)
MSL DD WI GP S1 -4.17 (1.5 10.0) -44.05 (5.0 70.0)
MSL EE WI GP S1 5.0 1.5
! There is a short microstrip section between the antenna and the
! radial stub.
MSL RS WI GP S1 2.00 1.0
! Now, we shall put the quarter-wave stub. The small radial section
! is simulated in two sections of 3um and 5um widths and 1um long
! each, connecting to 6um width quarter-wave stub.
MSL RT WI GP S1 3 1.0
CAS RS RT
MSL RT WI GP S1 5 1.0
CAS RS RT
MSL RT WI GP S1 6 41.0
CAS RS RT
! The stub is connected to the CPW sections, used for filtering the RF
! signals.
TRL RT SE 53.59 10.03 550 0 0
CAS RS RT
TRL RT SE 80.56 90 550 0 0
CAS RS RT
TRL RT SE 39.2 90 550 0 0
CAS RS RT
! Junction capacitance, 85 fF/sq micron, * (1.3)^2  sq microns =
! 143.65 fF. Here, we will need two capacitances. One will have the
! junction capacitance in parallel with the Rn and the other will
! have just the capacitance as before, and the Rn will come with the
! ideal transformer. Junction resistance is 20 Ohm-sq.micron / (1.3)^2
! sq.micron = 11.83 Ohm.
! The first one is the capacitor in parallel with the resistor and is
! connected in parallel with the rest of the circuit.
```

```
PRC FF PA 11.83 143.85
! Tuning inductor. Here, the inductor will be in series. Inductor
! width is 5um.
MSL GG WI GP S1 5.0  -14.65
! Since we are putting a port with the second junction, we will only
! put the capacitor of the junction, the resistor will come with the
! port.
CAP HH PA 143.65
! We will put the other junction resistance now.
XFM JJ SE 11.83  50.000
! Now, we will hook them all up.
! First, we need to deal with the open circuit stub. Calculate the
! input impedance of the stub and convert to series element. CPW lines
! are terminated into 58 Ohms.
PBR RY RS 58.
PTS RZ RY
! Open ended quarter wave stub adds series impedance:
CAS BB RZ
! Rest of circuit...First the transformer
CAS BB QQ
CAS BB CC
CAS BB DD
CAS BB EE
! Now the parallel combination of resistor and capacitor.
CAS BB FF
! Tuning inductor.
CAS BB GG
! The second capacitor and and the rest of the circuit.
CAS BB HH
CAS BB JJ
! Two port calculation. Frequency sweep in three separate ranges.
! The first range is from 200 GHz to 490 GHz with 10 GHz step. At
! our frequency of interest, we want sweep with better resolution, and
! the range is 500 GHz to 600 GHz with 5 GHz step, and then from 610 GHz
! to 1000 GHz with 10 GHz step.
PRI BB S1 50.000
END
200 490 10
500 600 5
610 1000 10
END
```

Program listing for calculating power coupled to the second junction S_{31} using Figure 8.2(c) circuit set up.

```
! Dual-Polarized SIS Mixer Design
! Goutam Chattopadhyay, 10.24.97.
! Frequency 550 GHz
```

```
! file: 1_3um_b.ckt
! Circuit layed out for JPL contact aligner.
! Nb/AlOx/Nb junctions with 2000A SiO (single layer), 2500A wiring layer,
! and 2000A Nb ground plane.
! Nominal juntions areas are: 1.2um, 1.3um, 1.4um.
! This circuit is designed for 1.3um x 1.3um with a RnA = 20 Ohm*um^2
! Resistivity of Nb is 5 uOhm-cm.
! Vphase = 0.32c. Tc = 9.2 K, V_gap = 2.9 mV
! This file calculates S31, where port 1 is the antenna and port 3 is
! connected at the second junction.
! First, we will read in the antenna impedance file, calculated using
! method of moments analysis.
ONF AA IR ~/sis/p_circuit/dual_pol/Zslot/Zslot.550
XIN BB AA 100000  50.000
! Define surface impedance for ground plane and wiring layer
! Nb: 9.2 K Tc, 5 micro-ohm cm resistivity,  2.9 mV Vgap
! Ground plane is 2000 Angstroms thick.
LSI GP SE 0.2 5. 2.9 0.00001 550. 0.5
! Wiring is 2500 Angstroms thick
LSI WI SE 0.25 5. 2.9 0.00001 550. 0.5
! Use only one layer of 2000A SiO for transformers and tuning inductor.
SUB S1 SE 1. 0. 5.6 0. 0.2
! Define the microstrip two-section transformer, with one short
! microstrip section (2um wide, 1um long) connected between the
! antenna and the microstrip transformer, and a short microstrip
! section (5um wide, 1.5um long) between the transformer and the
! junctions. Inductance width is 5um, and hence, the last section
! used is 5um wide.
MSL QQ WI GP S1 2.0 1.0
MSL CC WI GP S1 -1.50 (1.5 10.0) -36.64 (5.0 70.0)
MSL DD WI GP S1 -4.17 (1.5 10.0) -44.05 (5.0 70.0)
MSL EE WI GP S1 5.0 1.5
! There is a short microstrip section between the antenna and the
! radial stub.
MSL RS WI GP S1 2.00 1.0
! Now, we shall put the quarter-wave stub. The small radial section
! is simulated in two sections of 3um and 5um widths and 1um long
! each, connecting to 6um width quarter-wave stub.
MSL RT WI GP S1 3 1.0
CAS RS RT
MSL RT WI GP S1 5 1.0
CAS RS RT
MSL RT WI GP S1 6 41.0
CAS RS RT
! The stub is connected to the CPW sections, used for filtering the RF
! signals.
TRL RT SE 53.59 10.03 550 0 0
```

```
CAS RS RT
TRL RT SE 80.56 90 550 0 0
CAS RS RT
TRL RT SE 39.2 90 550 0 0
CAS RS RT
! Junction capacitance, 85 fF/sq micron, * (1.3)^2  sq microns =
! 143.65 fF. Here, we will need two capacitances. One will have the
! junction capacitance in parallel with the Rn and the other will
! have just the capacitance as before, and the Rn will come with the
! ideal transformer. Junction resistance is 20 Ohm-sq.micron / (1.3)^2
! sq.micron = 11.83 Ohm.
! The first one is the capacitor alone where the port will be
! connected. The resistor of the junction will be connected with the
! port.
CAP FF 143.85
! Tuning inductor. Here, the inductor will be in series. Inductor
! width is 5um.
MSL GG WI GP S1 5.0  -14.65
! Now the other capacitor.
CAP HH PA 143.65
! We will put the junction resistance now, but this will form a port.
XFM JJ SE 11.83  50.000
! Now, we will hook them all up.
! First, we need to deal with the open circuit stub. Calculate the
! input impedance of the stub and convert to series element. CPW lines
! are terminated into 58 Ohms.
PBR RY RS 58.
PTS RZ RY
! Open ended quarter wave stub adds series impedance:
CAS BB RZ
! Rest of circuit...First the transformer
CAS BB QQ
CAS BB CC
CAS BB DD
CAS BB EE
! Now the first capacitor.
CAS BB FF
! Now, we need to put the tuning inductor, the other capacitor, and
! the remaining resistor. But we will put the remaing resistor using a
! transformer.
CAS GG HH
PBR KK GG 11.83
CAS BB KK
! Now put the remaining resistance which will form a port.
CAS BB JJ
! Two port calculation. Frequency sweep in three separate ranges.
! The first range is from 200 GHz to 490 GHz with 10 GHz step. At
```

```
! our frequency of interest, we want sweep with better resolution, and
! the range is 500 GHz to 600 GHz with 5 GHz step, and then from 610 GHz
! to 1000 GHz with 10 GHz step.
PRI BB S1 50.000
END
200 490 10
500 600 5
610 1000 10
END
```

References

[1] M. Bin, "Low-Noise THz Niobium SIS Mixers," PhD Dissertation, California Institute of Technology, Pasadena, October 1996.

Appendix B: SuperMix Programs

"SuperMix" is software library written to aid in the calculation and optimization of the signal and noise performance of high frequency circuits, especially those including superconductors and superconducting tunnel junctions [1], [2]. Using the *SuperMix* library, C++ programs are written to simulate circuits of arbitrary size. *SuperMix* has the capability to calculate the signal and noise performance of SIS heterodyne receivers using Tucker's theory [3]. Following are the C++ programs used to simulate the single-polarized, the dual-polarized, and the balanced mixers reported in this thesis.

Program listing for single.h – which is used to specify a single polarization receiver using cross-slot antenna and four junctions

```
// Specification file for Single Polarization (4 junctions) receiver
// The superconductors used:
const sc_material & GP_MATERIAL  = nb;      // ground plane material
const sc_material & TOP_MATERIAL = nb;      // top strip material
// SIS junction parameters
parameter RNA  = 23.2*Ohm*Micron*Micron;    // normal resistance -
                                            // area product
parameter SCAP = 85.0*fFarad/Micron/Micron; // specific capacitance
parameter AREA = 1.36*1.36*Micron*Micron;   // effective junction area
parameter VGAP = 2.68*mVolt;                // SIS gap voltage
parameter VBIAS = 3.9*mVolt;                // SIS bias voltage
const char * const IDC_FILE = "singleiv.dat";  // DC IV characteristic
                                           // (normalized to Vgap and Rn)
const char * const IKK_FILE = "singleikk.dat"; // Kramers-Kronig
                                           //transform of the DC IV curve
// layer thicknesses:
parameter GP_THICKNESS   = 2000.*Angstrom;  // ground plane
parameter TOP_THICKNESS  = 2500.*Angstrom;  // top strip
parameter MS_THICKNESS   = 2000.*Angstrom;  // SiO layer generally
parameter TUNE_THICKNESS = & MS_THICKNESS;  // SiO in tuning inductor
// Microstrip dimensions (width,length) (each entry is a parameter):
wl RF_0 = { 2.0*Micron,  1.0*Micron };     // tiny rf section near antenna
wl RF_1 = { 1.5*Micron, 38.8*Micron };      // rf transformer section 1
```

```
                                          // (antenna end)
wl RF_3 = { 4.3*Micron, 44.1*Micron };    // rf transformer section 3
                                          //(following taper)
wl IF_0 = { 2.0*Micron,  1.0*Micron };    // tiny if section near antenna
wl IF_1 = { 3.0*Micron,  1.0*Micron };    // transition 1
wl IF_1A = { 5.0*Micron,  1.0*Micron };   // transition 2
wl IF_2 = { 6.0*Micron, 41.0*Micron };    // if section 2 (near IF output)
wl T_1  = { 5.0*Micron, 1.5*Micron };     // tuning inductor bit between
                                          // transformer and SIS
wl T_2  = { 5.0*Micron, 14.54*Micron };   // length of tuning inductor
                                          // between junctions
// Local Oscillator and IF output parameters:
parameter LO_POWER = 230*Nano*Watt;       // the LO power at the antenna
parameter LO_FREQ  = 527.0*GHz;           // the LO frequency
parameter LO_TEMP  = 0.0*Kelvin;          // thermal noise source
                                          // temperature at input
parameter IF_FREQ  = 1.5*GHz;             // the IF frequency
complex_parameter IF_TERM = complex(50*Ohm);// the input impedance of the
                                          // IF amplifier
// The antenna impedance information (these cannot change during runtime):
const char * const ANT_FILE = "Zant.550"; // antenna impedance file name
const double ANT_FILE_FREQ  = 550.0*GHz;  // the antenna frequency used
                                          // in the file data
const double ANT_TUNE_FREQ  = 550.0*GHz;
// Mixer calculations:
int HARMONICS = 2;
// The receiver temperature (remains constant during runtime):
const double TEMPERATURE = 4.2*Kelvin;
```

Program listing for main.basic.inc.cc – which builds the single-polarized mixer circuitry.

```
// include this in main(){ }: it actually builds the circuitry
  // set up global variables:
  device::T = TEMPERATURE;
  device::f = & IF_FREQ;
  // the junctions and the junction current calculator:
  sis_parameter_class sis_parms(RNA, SCAP, AREA, VGAP, IDC_FILE, IKK_FILE);
  init_sis sis1(sis_parms), sis2(sis_parms), sis3(sis_parms), sis4(sis_parms);
  current.n = 2; current.p[0] = &sis1; current.p[1] = &sis2;
// ***
// set Rn and Cap of Junctions directly:
  parameter Rn, Cj;
  sis1.Rn = &Rn; sis1.Cap = &Cj;
  sis2.Rn = &Rn; sis2.Cap = &Cj;
  sis3.Rn = &Rn; sis3.Cap = &Cj;
  sis4.Rn = &Rn; sis4.Cap = &Cj;
  Rn = 12.54*Ohm;
```

```
  Cj = 170*fFarad;
// ***
//  device::Z0 = sis1.Rn*.5;
  // the materials:
  film gp(GP_MATERIAL,&GP_THICKNESS), top(TOP_MATERIAL,&TOP_THICKNESS);
//  opt_film gp(GP_MATERIAL,&GP_THICKNESS), top(TOP_MATERIAL,&TOP_THICKNESS);
  sio_diel    sio;
  vacuum_diel vacuum;
  ms_material ms_matl = {gp,sio,top,vacuum};
  // some common circuit elements:
  branch b1, b2;
  open_term  Open;
  short_term Short;
  series_tee tee;
  splitter srf;
  // the microstrips
  ms rf_0(ms_matl, RF_0, MS_THICKNESS),     // the transformer section 0
     rf_1(ms_matl, RF_1, MS_THICKNESS),     // the transformer section 1
     rf_3(ms_matl, RF_3, MS_THICKNESS),     // the transformer section 3

     t_1(ms_matl, T_1, TUNE_THICKNESS),     // the tuning inductor, toward rf
     t_2(ms_matl, T_2, TUNE_THICKNESS),     // the tuning inductor, between sis
     t_3(ms_matl, T_1, TUNE_THICKNESS),     // the tuning inductor, at open

     if_0(ms_matl, IF_0, MS_THICKNESS),     // the if output section 0
     if_1(ms_matl, IF_1, MS_THICKNESS),     // the if output section 1
     if_1a(ms_matl, IF_1A, MS_THICKNESS),   // the if output section 1a
     if_2(ms_matl, IF_2, MS_THICKNESS);     // the if output section 2
  // the antenna at RF freqs:
  transformer ant;                  // port 1: RF signal; port 2: receiver
  complex_interp Za(device::f);
  {
    // we use brackets here to have a temporary variable "dat"
    real_matrix dat = *(datafile(ANT_FILE).table());
    scalerow(1,dat,ANT_TUNE_FREQ/ANT_FILE_FREQ*GHz);
    scalerow(2,dat,Ohm);
    scalerow(3,dat,Ohm);
    Za.table(dat,1,2,3);
  }
  ant.Z2 = & Za;
  ant.Z1 = device::Z0;
  // the rf and if matching circuits:
  cascade rf_match;
  rf_match.a(rf_0).a(rf_1).a(rf_3);          // port 1: ant; port 2:
                                             // sis tune ckt
  cascade if_match;
  if_match.a(if_0).a(if_1).a(if_1a).a(if_2); // port 1: ant; port 2:
```

```
                                        // if output
// tuning circuit:
circuit tune;
tune.add_port(b1,3);               // port 1: sis nearest antenna
tune.add_port(b2,3);               // port 2: other sis
tune.add_port(t_1,1);              // port 3: to rf matching network
tune.connect(t_1,2, b1,2);
tune.connect(b1,1, t_2,1);
tune.connect(b2,1, t_2,2);
tune.connect(b2,2, t_3,1);
tune.connect(t_3,2, Open,1);
// the RF frequency complete linear circuits for one antenna:
circuit rf_circuit_L;
zterm cpw(58*Ohm);
rf_circuit_L.connect(cpw,1,if_match,2);
rf_circuit_L.connect(if_match,1,tee,1);
rf_circuit_L.connect(tee,2,ant,2);
rf_circuit_L.connect(tee,3,rf_match,1);
rf_circuit_L.connect(rf_match,2,tune,3);
rf_circuit_L.add_port(tune,1);          // port 1: sis nearest antenna
rf_circuit_L.add_port(tune,2);          // port 2: other sis
rf_circuit_L.add_port(ant,1);           // port 3: rf signal
circuit rf_circuit_R(rf_circuit_L);     // copy for the other half
// the IF frequency complete linear circuits for one antenna:
circuit if_circuit_L;
if_circuit_L.connect(if_match,1,rf_match,1);
if_circuit_L.connect(rf_match,2,tune,3);
if_circuit_L.add_port(tune,1);          // port 1: sis nearest antenna
if_circuit_L.add_port(tune,2);          // port 2: other sis
if_circuit_L.add_port(if_match,2);      // port 3: if output signal
circuit if_circuit_R(if_circuit_L);     // copy for the other half
// connect RF circuit halves using splitter
circuit rf_circuit;
rf_circuit.add_port(rf_circuit_L, 1);    // port 1: sis1
rf_circuit.add_port(rf_circuit_L, 2);    // port 2: sis2
rf_circuit.add_port(rf_circuit_R, 1);    // port 3: sis3
rf_circuit.add_port(rf_circuit_R, 2);    // port 4: sis4
int lo_term_port = rf_circuit.add_port(srf, 1); // port 5: rf signal
rf_circuit.connect(srf, 2, rf_circuit_L, 3);
rf_circuit.connect(srf, 3, rf_circuit_R, 3);
// build IF circuit from halves; include real combiner circuitry
circuit if_circuit;
transformer if_load;
if_load.Z2 = & IF_TERM;
if_load.Z1 = device::Z0;
trline L1;
L1.zchar = 112.4*Ohm;
```

```
L1.freq = 1.5*GHz;
L1.theta = 51.4*Degree;
trline L2(L1);
L2.theta = 28.4*Degree;
capacitor C1(2*Pico*Farad), C2(1.2*Pico*Farad);
C1.series(); C2.parallel();
circuit sif;
sif.add_port(b1,1);     // to if load
sif.connect(b1,2,C1,1);
sif.connect(C1,2,b2,1);
sif.connect(b2,3,L1,1);
sif.connect(L1,2,Short,1);
sif.add_port(b2,2);     // to if_circuit_L
sif.connect(b1,3,L2,1);
sif.connect(L2,2,C2,1);
sif.add_port(C2,2);     // to if_circuit_R
if_circuit.add_port(if_circuit_L, 1);     // port 1: sis1
if_circuit.add_port(if_circuit_L, 2);     // port 2: sis2
if_circuit.add_port(if_circuit_R, 1);     // port 3: sis3
if_circuit.add_port(if_circuit_R, 2);     // port 4: sis4
if_circuit.connect(if_circuit_L, 3, sif, 2);
if_circuit.connect(if_circuit_R, 3, sif, 3);
if_circuit.connect(sif, 1, if_load, 2);
int if_out = if_circuit.add_port(if_load, 1); // port 5: if output
// the LO source:
generator LO;
LO.R = device::Z0;
LO.Temp = & LO_TEMP;
LO.source_f = & LO_FREQ;
LO.source_width = 1*Hertz;
LO.source_power = & LO_POWER;
// the bias circuit:
circuit bias_circuit;
voltage_source batt;
batt.source_voltage = & VBIAS;
bias_circuit.connect(batt,1,tee,1);
bias_circuit.connect(tee,3,b1,1);
bias_circuit.add_port(b1,2);          // port 1: sis nearest L antenna
bias_circuit.add_port(b1,3);          // port 2: other sis on L circuit
bias_circuit.connect(tee,2,b2,1);
bias_circuit.add_port(b2,2);          // port 3: sis nearest R antenna
bias_circuit.add_port(b2,3);          // port 4: other sis on R circuit
// the mixer
mixer mix;
mix.harmonics(HARMONICS).add_junction(sis1).add_junction(sis2).
add_junction(sis3).add_junction(sis4);
mix.set_LO(&LO_FREQ);
```

```
  mix.set_bias(bias_circuit).set_if(if_circuit).set_rf(rf_circuit);
  mix.set_balance_terminator(LO,lo_term_port);
  int rf_port = mix.port(lo_term_port,1);
  int if_port = mix.port(if_out,0);
```

Program listing for matchivfts.cc – which is used for simultaneous match of the IV and the FTS data for the single-polarized mixer.

```
#define SPEC_FILE "single.h"
#include "supermix.h"
#include <fstream.h>
#include "materials.h"
#include SPEC_FILE
// offset errors in the measured iv data:
parameter i_offset = 0;
parameter v_offset = 0;
class iv_match : public error_term {
public:
  mixer *m;
  interpolation *p;
  double get(state_tag)
    { m->balance(); return norm(current()+i_offset - (*p)(VBIAS+v_offset)); }
} et_iv;
parameter FTS_FREQ;  // the frequency for FTS sweeps
parameter FTS_BIAS;  // the fts bias voltage
class my_fts_match : public scaled_match_error_term {
public:
  mixer *m;
  interpolation *f;    // measured fts data
  double power;        // LO pumping power
  parameter pwr_save;  // save LO power
  parameter frq_save;  // save LO frequency
  parameter bias_save; // save VBIAS
  double get_a(state_tag) { return (*f)(FTS_FREQ)/4.19e-5; }
  double get_b(state_tag)
    {
      pwr_save = LO_POWER; frq_save = LO_FREQ; bias_save = VBIAS;
      LO_FREQ = FTS_FREQ; VBIAS = FTS_BIAS;
      double response;
      LO_POWER = 0; m->balance(); response = -current();
      LO_POWER = power; m->balance(); response += current();
      LO_FREQ = frq_save; LO_POWER = pwr_save; VBIAS = bias_save;
      return response*FTS_FREQ;
    }
} et_fts;
main(int argc, char** argv)
{
  if (argc != 5) {
```

```
    error::fatal("Usage: matchivfts <ivdatafile> <ftsdatafile>
    <ivout> <ftsout>");
  }
  ofstream ivout(argv[3]);
  ofstream ftsout(argv[4]);
#ifdef BALANCED
#  include "main.balanced.inc.cc"
#else
#  ifdef DUAL
#    include "main.dual.inc.cc"
#  else
#    include "main.basic.inc.cc"
#  endif
#endif
  // ************************************************************
  // Use optimizer to match an iv curve
  // read in iv curve data:
  const char * iv_file = argv[1];
  real_interp iv_data(VBIAS);
  real_matrix D = *(datafile(iv_file).table());
  scalerow(1,D,mVolt);
  scalerow(2,D,Micro*Amp);
  iv_data.table(D,1,2);
  iv_data.linear().build();
  iv_data.no_extrapolation_warning(1);
  // read in fts data:
  const char * fts_file = argv[2];
  real_interp fts_data(FTS_FREQ);
  real_matrix F = *(datafile(fts_file).table());
  scalerow(1,F,GHz);
  scalerow(2,F,1.0);
  real_vector fts_freqs = row(1,F);
  fts_data.table(F,1,2);
  fts_data.linear().build();
  fts_data.no_extrapolation_warning(1);
  // set up error terms:
  et_iv.m = &mix; et_iv.p = &iv_data;
  et_fts.m = &mix; et_fts.f = &fts_data; et_fts.power = .001*Nano*Watt;
  parameter Rho; Rho = 5*Micro*Ohm*Centi*Meter;
  gp.uf.rho_normal = &Rho; top.uf.rho_normal = &Rho;
  // set up sweepers:
  sweeper sw_fts;
  sw_fts.sweep(FTS_FREQ, fts_freqs);
  sweeper step;
  step.sweep(VBIAS, 0.4*mVolt, 1.6*mVolt, .05*mVolt);
  sweeper gap;
  gap.sweep(VBIAS, 4.5*mVolt, 6.5*mVolt, .05*mVolt);
```

```
  sweeper bgap;
  bgap.sweep(VBIAS, 1.0*mVolt, 5.0*mVolt, .4*mVolt);
  sweeper agap;
  agap.sweep(VBIAS, 6.0*mVolt, 7.5*mVolt, .4*mVolt);
  sweeper step_b;
  step_b.sweep(VBIAS, -0.4*mVolt, -1.6*mVolt, -.05*mVolt);
  sweeper gap_b;
  gap_b.sweep(VBIAS, -4.5*mVolt, -6.5*mVolt, -.05*mVolt);
  sweeper bgap_b;
  bgap_b.sweep(VBIAS, -1.0*mVolt, -5.0*mVolt, -.4*mVolt);
  sweeper agap_b;
  agap_b.sweep(VBIAS, -6.0*mVolt, -7.5*mVolt, -.4*mVolt);
  // set up error functions
  error_func ef_Cj;
  ef_Cj.add_term(5000,bgap,et_iv);
  ef_Cj.add_term(5000,step,et_iv);
  ef_Cj.add_term(5000,agap,et_iv);
  ef_Cj.add_term(1.5,sw_fts,et_fts);
// error functions just used to get relative weighting of the iv and fts:
  VGAP     = 2.68365*mVolt;
  Rn       = 12.5513*Ohm;
  i_offset = -0.4*Micro*Amp;
  v_offset = 0.00183*mVolt;
  FTS_BIAS = 4.41*mVolt;
  error_func ef_iv, ef_fts;
  ef_iv.add_term(5000,bgap,et_iv);
  ef_iv.add_term(5000,step,et_iv);
  ef_iv.add_term(5000,agap,et_iv);
  LO_FREQ  = ef_iv.vary(526, 528, 529,GHz);
  Cj       = ef_iv.vary(150, 150, 200,fFarad);
  Rho          = ef_iv.vary(4, 5.15, 8,Micro*Ohm*Centi*Meter);
  MS_THICKNESS = ef_iv.vary(1600, 2400, 2400,Angstrom);
  sio.eps      = ef_iv.vary(4, 5.74, 6);
  LO_POWER     = ef_iv.vary(220, 220, 310,Nano*Watt);
  error::stream() << "\nIV curve ef val: " << ef_iv() << endl;
  ef_fts.add_term(1.5,sw_fts,et_fts);
  LO_FREQ  = ef_fts.vary(526, 528, 529,GHz);
  Cj       = ef_fts.vary(150, 150, 200,fFarad);
  Rho          = ef_fts.vary(4, 5.15, 8,Micro*Ohm*Centi*Meter);
  MS_THICKNESS = ef_fts.vary(1600, 2400, 2400,Angstrom);
  sio.eps      = ef_fts.vary(4, 5.74, 6);
  LO_POWER     = ef_fts.vary(220, 220, 310,Nano*Watt);
  error::stream() << "FTS curve ef val: " << ef_fts() << endl << endl;
  // the optimizers
  powell opt_Cj(ef_Cj);
  opt_Cj.FTOL = 0.0001;
  Rho = 5*Micro*Ohm*Centi*Meter;
```

```
VGAP     = 2.68365*mVolt;
Rn       = 12.5513*Ohm;
i_offset = -0.4*Micro*Amp;
v_offset = 0.00183*mVolt;
FTS_BIAS = 4.41*mVolt;
LO_FREQ  = ef_Cj.vary(527, 528, 528.5,GHz);
Cj       = ef_Cj.vary(120, 150, 200,fFarad);
Rho          = ef_Cj.vary(4, 5.15, 8,Micro*Ohm*Centi*Meter);
MS_THICKNESS = ef_Cj.vary(1600, 2400, 2600,Angstrom);
sio.eps      = ef_Cj.vary(4, 5.74, 7);
LO_POWER     = ef_Cj.vary(200, 220, 310,Nano*Watt);
opt_Cj.very_verbose();
opt_Cj.FOCUS = 0.4;
opt_Cj.ITMAX = 40;
opt_Cj.CLOSENESS = 3;
opt_Cj.minimize();
error::stream() << "opt_Cj solution:" << endl
                << ef_Cj.get_parms_user() << endl;
error::stream() << "\nFinal parameter values:" << endl;
error::stream() << "VGAP (mV): " << VGAP/mVolt << " ;
                    Rn (Ohm): " << Rn/Ohm << endl;
error::stream() << "LO_FREQ (GHz): " << LO_FREQ/GHz
                << " ; LO_POWER (nW): " << LO_POWER/(Nano*Watt)
                << " ; Cj (fFarad): " << Cj/fFarad << endl
                << " ; Rho (uOhm cm): "
                << Rho/(Micro*Ohm*Centi*Meter) << endl
                << " ; T (Angstrom): " << MS_THICKNESS/Angstrom << endl
                << " ; Eps: " << sio.eps << endl
                << endl;

// output an iv curve using the optimized parameters (including offsets):
for(double v = -8; v <= 8; v += .05) {
  VBIAS = v * mVolt;
  ivout << (VBIAS+v_offset)/mVolt;
  mix.balance();
  ivout << "\t" << (current()+i_offset)/(Micro*Amp);
  ivout << endl;
}
// output the fts response
double power = et_fts.power;
VBIAS = FTS_BIAS;
for(double f = 200*GHz; f <= 800*GHz; f += 6*GHz) {
  LO_FREQ = f;
  ftsout << f/GHz;
  double response;
  LO_POWER = power;
  mix.balance();
```

```
    response = current()*f;
    LO_POWER = 0;
    mix.balance();
    response -= current()*f;
    ftsout << "\t" << response/(.000104*.0105) << endl;
  }
}
```

Program listing for unpump.cc – which is used to obtain VGAP, Rn, i_offset, and v_offset for the balanced mixer by matching unpumped IV data.

```
#define SPEC_FILE "balanced.h"
#include "supermix.h"
#include "materials.h"
#include SPEC_FILE
// offset errors in the measured iv data:
parameter i_offset = 0;
parameter v_offset = 0;
class iv_match : public error_term {
public:
  mixer *m;
  interpolation *p;
  double get(state_tag)
    { m->balance(); return 1000*norm(current()+i_offset -
      (*p)(VBIAS+v_offset)); }
} et;
main(int argc, char** argv)
{

  if (argc != 2) {
    error::fatal("Usage: unpump <ivdatafile>\n"
                 "match an unpumped IV, giving Vgap and Rn");
  }
HARMONICS = 1;
#ifdef BALANCED
#  include "main.balanced.inc.cc"
#else
#  ifdef DUAL
#    include "main.dual.inc.cc"
#  else
#    include "main.basic.inc.cc"
#  endif
#endif
  // ************************************************************
  // Use optimizer to match an unpumped iv curve, giving Vgap and Rn
  // read in iv curve data:
  const char * iv_file = argv[1];
```

```
real_interp iv_data(VBIAS);
real_matrix D = *(datafile(iv_file).table());
scalerow(1,D,mVolt);
scalerow(2,D,Micro*Amp);
iv_data.table(D,1,2);
iv_data.linear().build();
iv_data.no_extrapolation_warning(1);
real_vector voltages = row(1,D);
// set up error term
et.m = &mix; et.p = &iv_data;
// set up sweeper
sweeper sw_bias;
sw_bias.sweep(VBIAS, -1.6*mVolt, 1.6*mVolt, .02*mVolt);
sweeper sw_gap_p;
sw_gap_p.sweep(VBIAS, 1*mVolt, 5*mVolt, .5*mVolt);
sweeper sw_gap_n;
sw_gap_n.sweep(VBIAS, -1*mVolt, -5*mVolt, -.5*mVolt);
sweeper sw_agap_p;
sw_agap_p.sweep(VBIAS, 6*mVolt, 7.5*mVolt, .1*mVolt);
sweeper sw_agap_n;
sw_agap_n.sweep(VBIAS, -6*mVolt, -7.5*mVolt, -.1*mVolt);
// set up error function and parameters to optimize:
error_func ef;
ef.add_term(1, sw_bias, et);
ef.add_term(1, sw_gap_p, et);
ef.add_term(1, sw_gap_n, et);
ef.add_term(1, sw_agap_p, et);
ef.add_term(1, sw_agap_n, et);
VGAP     = ef.vary(2.4,2.68,2.9,mVolt);
Rn       = ef.vary(9,11.66,14,Ohm);
i_offset = ef.vary(-10,0.0357,10,Micro*Amp);
v_offset = ef.vary(-.05,0.0077,.05,mVolt);
// the optimizer
powell opt(ef);
opt.FTOL = 0.0001;
opt.verbose();
// run the optimization:
LO_POWER = 0.0;
opt.minimize();
error::stream() << "opt solution:" << endl << ef.get_parms_user()
                << endl;
error::stream() << "\nFinal parameter values:" << endl;
error::stream() << "VGAP (mV): " << VGAP/mVolt << " ; Rn (Ohm): "
                << Rn/Ohm << endl;
error::stream() << "I offset(uA): " << i_offset/(Micro*Amp)
                << " ; V offset(mV): " << v_offset/mVolt
                << endl;
```

```
  // output the unpumped iv curve using the optimized parameters and
  // offsets:
  for(double v = iv_data.x(0); v <= iv_data.x(iv_data.size()-1);
      v += .05*mVolt) {
    VBIAS = v;
    cout << (VBIAS+v_offset)/mVolt;
    mix.balance();
    cout << "\t" << (current()+i_offset)/(Micro*Amp);
    cout << endl;
  }
}
```

Program listing for main.balanced.cc – which details the balanced mixer circuitry.

```
// BALANCED MIXER
// include this in main(){ }: it actually builds the circuitry
  // set up global variables:
  device::T = TEMPERATURE;
  device::f = & IF_FREQ;
  // the junctions and the junction current calculator:
  sis_parameter_class sis_parms(RNA, SCAP, AREA, VGAP, IDC_FILE, IKK_FILE);
  init_sis sis1(sis_parms), sis2(sis_parms), sis3(sis_parms), sis4(sis_parms);
  init_sis sis5(sis_parms), sis6(sis_parms), sis7(sis_parms), sis8(sis_parms);
  current.n = 4;
  current.p[0] = &sis1; current.p[1] = &sis2; current.p[2] =
  &sis5; current.p[3] = &sis6;
// ***
// set Rn and Cap of Junctions directly:
  parameter Rn, Cj;
  sis1.Rn = &Rn; sis1.Cap = &Cj;
  sis2.Rn = &Rn; sis2.Cap = &Cj;
  sis3.Rn = &Rn; sis3.Cap = &Cj;
  sis4.Rn = &Rn; sis4.Cap = &Cj;
  sis5.Rn = &Rn; sis5.Cap = &Cj;
  sis6.Rn = &Rn; sis6.Cap = &Cj;
  sis7.Rn = &Rn; sis7.Cap = &Cj;
  sis8.Rn = &Rn; sis8.Cap = &Cj;
  Rn = 11.7254*Ohm;
  Cj = 165*fFarad;
// ***
//  device::Z0 = sis1.Rn*.5;
// the materials:
  film gp(GP_MATERIAL,&GP_THICKNESS), top(TOP_MATERIAL,&TOP_THICKNESS);
  sio_diel    sio;
  vacuum_diel vacuum;
  ms_material ms_matl = {gp,sio,top,vacuum};
  // some common circuit elements:
```

```
branch b1, b2;
open_term  Open;
short_term Short;
series_tee tee;
splitter   srf;
combiner   grid;
attenuator window;
window.dB = & WINDOW_LOSS;
window.Temp = & WINDOW_TEMP;
// the microstrips
ms rf_0(ms_matl, RF_0, MS_THICKNESS),     // the transformer section 0
   rf_1(ms_matl, RF_1, MS_THICKNESS),     // the transformer section 1
   rf_3(ms_matl, RF_3, MS_THICKNESS),     // the transformer section 3

   t_1(ms_matl, T_1, TUNE_THICKNESS),  // the tuning inductor, toward rf
   t_2(ms_matl, T_2, TUNE_THICKNESS), // the tuning inductor, between sis
   t_3(ms_matl, T_1, TUNE_THICKNESS),     // the tuning inductor, at open

   if_0(ms_matl, IF_0, MS_THICKNESS),     // the if output section 0
   if_1(ms_matl, IF_1, MS_THICKNESS),     // the if output section 1
   if_1a(ms_matl, IF_1A, MS_THICKNESS),   // the if output section 1a
   if_2(ms_matl, IF_2, MS_THICKNESS);     // the if output section 2
// the antenna at RF freqs:
transformer ant;                  // port 1: RF signal; port 2: receiver
complex_interp Za(device::f);
{
  // we use brackets here to have a temporary variable "dat"
  real_matrix dat = *(datafile(ANT_FILE).table());
  scalerow(1,dat,ANT_TUNE_FREQ/ANT_FILE_FREQ*GHz);
  scalerow(2,dat,Ohm);
  scalerow(3,dat,Ohm);
  Za.table(dat,1,2,3);
}
ant.Z2 = & Za;
ant.Z1 = device::Z0;
// the rf and if matching circuits:
cascade rf_match;
rf_match.a(rf_0).a(rf_1).a(rf_3);    // port 1: ant; port 2: sis tune ckt
cascade if_match;
if_match.a(if_0).a(if_1).a(if_1a).a(if_2);  // port 1: ant; port 2:
if output
// tuning circuit:
circuit tune;
tune.add_port(b1,3);               // port 1: sis nearest antenna
tune.add_port(b2,3);               // port 2: other sis
tune.add_port(t_1,1);              // port 3: to rf matching network
tune.connect(t_1,2, b1,2);
```

```
tune.connect(b1,1, t_2,1);
tune.connect(b2,1, t_2,2);
tune.connect(b2,2, t_3,1);
tune.connect(t_3,2, Open,1);
// the LO source:
generator LO;
LO.R = device::Z0;
LO.Temp = 300*Kelvin;
LO.source_f = & LO_FREQ;
LO.source_width = 1*Hertz;
LO.source_power = & LO_POWER;
// the RF balance terminator (just a resistor)
zterm RF_terminator;
RF_terminator.Z = device::Z0;
RF_terminator.Temp = &LO_TEMP;
// the RF frequency complete linear circuits for one antenna:
circuit rf_circuit_HL;
zterm cpw(58*Ohm);
rf_circuit_HL.connect(cpw,1,if_match,2);
rf_circuit_HL.connect(if_match,1,tee,1);
rf_circuit_HL.connect(tee,2,ant,2);
rf_circuit_HL.connect(tee,3,rf_match,1);
rf_circuit_HL.connect(rf_match,2,tune,3);
rf_circuit_HL.add_port(tune,1);            // port 1: sis nearest antenna
rf_circuit_HL.add_port(tune,2);            // port 2: other sis
rf_circuit_HL.add_port(ant,1);             // port 3: rf signal
circuit rf_circuit_HR(rf_circuit_HL);      // copy for the other half of H
circuit rf_circuit_VL(rf_circuit_HL);      // copy for the L half of V
circuit rf_circuit_VR(rf_circuit_HL);      // copy for the other half of V
// connect RF circuit parts using combiner
circuit rf_circuit;
rf_circuit.connect(grid,3,rf_circuit_HL,3);
rf_circuit.connect(grid,4,rf_circuit_VR,3);
rf_circuit.connect(grid,5,rf_circuit_VL,3);
rf_circuit.connect(grid,6,rf_circuit_HR,3);
rf_circuit.connect(grid,2,LO,1);
rf_circuit.add_port(rf_circuit_HL,1); // port 1: sis1: H pol;
                                      // nearest L antenna
rf_circuit.add_port(rf_circuit_HL,2); // port 2: sis2: H pol;
                                      // other sis on L circuit
rf_circuit.add_port(rf_circuit_HR,1); // port 3: sis3: H pol;
                                      // nearest R antenna
rf_circuit.add_port(rf_circuit_HR,2); // port 4: sis4: H pol;
                                      // other sis on R circuit
rf_circuit.add_port(rf_circuit_VL,1); // port 5: sis5: V pol;
                                      // nearest L antenna
rf_circuit.add_port(rf_circuit_VL,2); // port 6: sis6: V pol;
```

```
                                    // other sis on L circuit
rf_circuit.add_port(rf_circuit_VR,1); // port 7: sis7: V pol;
                                    // nearest R antenna
rf_circuit.add_port(rf_circuit_VR,2); // port 8: sis8: V pol;
                                    // other sis on R circuit
rf_circuit.connect(window,2,grid,1);
int rf_term_port = rf_circuit.add_port(window,1);  // port 9: RF input
// the IF frequency complete linear circuits for one antenna:
circuit if_circuit_HL;
if_circuit_HL.connect(if_match,1,rf_match,1);
if_circuit_HL.connect(rf_match,2,tune,3);
if_circuit_HL.add_port(tune,1);           // port 1: sis nearest antenna
if_circuit_HL.add_port(tune,2);           // port 2: other sis
if_circuit_HL.add_port(if_match,2);       // port 3: if output signal
circuit if_circuit_HR(if_circuit_HL);     // copy for the others
circuit if_circuit_VR(if_circuit_HL);     // copy for the other
circuit if_circuit_VL(if_circuit_HL);     // copy for the other
// 180 hybrid construction
circuit sif;
transformer if_load;
if_load.Z2 = & IF_TERM;
if_load.Z1 = device::Z0;
trline L1;
L1.zchar = 112.4*Ohm;
L1.freq = 1.5*GHz;
L1.theta = 51.4*Degree;
trline L2(L1);
L2.theta = 28.4*Degree;
capacitor C1(2*Pico*Farad), C2(1.2*Pico*Farad);
C1.series(); C2.parallel();
sif.connect(b1,1,if_load,2);
sif.add_port(if_load,1);     // port 1: to if load
sif.connect(b1,2,C1,1);
sif.connect(C1,2,b2,1);
sif.connect(b2,3,L1,1);
sif.connect(L1,2,Short,1);
sif.add_port(b2,2);          // port 2: to HR+VL
sif.connect(b1,3,L2,1);
sif.connect(L2,2,C2,1);
sif.add_port(C2,2);          // port 3: to HL+VR
// DC blocking caps + branch:
circuit dcblock1;
capacitor Cdc1(150*Pico*Farad); Cdc1.series();
capacitor Cdc2(Cdc1);
dcblock1.connect(b1,1,Cdc1,1);
dcblock1.connect(b1,2,Cdc2,1);
dcblock1.add_port(Cdc1,2);     // port 1: to one IF out
```

```
dcblock1.add_port(Cdc2,2);     // port 2: to other IF out
dcblock1.add_port(b1,3);       // port 3: to hybrid
circuit dcblock2(dcblock1);
// build IF circuit from 4 parts; include real combiner circuitry
circuit if_circuit;
if_circuit.add_port(if_circuit_HL,1); // port 1: sis1: H pol;
                                      // nearest L antenna
if_circuit.add_port(if_circuit_HL,2); // port 2: sis2: H pol;
                                      // other sis on L circuit
if_circuit.add_port(if_circuit_HR,1); // port 3: sis3: H pol;
                                      // nearest R antenna
if_circuit.add_port(if_circuit_HR,2); // port 4: sis4: H pol;
                                      // other sis on R circuit
if_circuit.add_port(if_circuit_VL,1); // port 5: sis5: V pol;
                                      // nearest L antenna
if_circuit.add_port(if_circuit_VL,2); // port 6: sis6: V pol;
                                      // other sis on L circuit
if_circuit.add_port(if_circuit_VR,1); // port 7: sis7: V pol;
                                      // nearest R antenna
if_circuit.add_port(if_circuit_VR,2); // port 8: sis8: V pol;
                                      // other sis on R circuit
if_circuit.connect(dcblock1,1,if_circuit_VL,3);
if_circuit.connect(dcblock1,2,if_circuit_HR,3);
if_circuit.connect(dcblock1,3,sif,2);
if_circuit.connect(dcblock2,1,if_circuit_HL,3);
if_circuit.connect(dcblock2,2,if_circuit_VR,3);
if_circuit.connect(dcblock2,3,sif,3);
int if_out = if_circuit.add_port(sif,1); // port 9: IF output
// the bias circuit:
circuit bias_circuit, bias_circuit_H, bias_circuit_V;
voltage_source batt;
batt.source_voltage = & VBIAS;
bias_circuit_H.connect(tee,3,b1,1);
bias_circuit_H.add_port(b1,2);       // port 1: sis nearest L antenna
bias_circuit_H.add_port(b1,3);       // port 2: other sis on L circuit
bias_circuit_H.connect(tee,2,b2,1);
bias_circuit_H.add_port(b2,2);       // port 3: sis nearest R antenna
bias_circuit_H.add_port(b2,3);       // port 4: other sis on R circuit
bias_circuit_H.add_port(tee,1);      // port 5: to bias source
bias_circuit_V = bias_circuit_H;     // a copy for the other polarization
bias_circuit.connect(batt,1,b1,1);   // the complete bias circuitry
bias_circuit.connect(bias_circuit_H,5,b1,2);
bias_circuit.connect(bias_circuit_V,5,b1,3);
bias_circuit.add_port(bias_circuit_H,1); // port 1: sis1: H pol;
                                         // nearest L antenna
bias_circuit.add_port(bias_circuit_H,2); // port 2: sis2: H pol;
                                         // other sis on L circuit
```

```
  bias_circuit.add_port(bias_circuit_H,3); // port 3: sis3: H pol;
                                           // nearest R antenna
  bias_circuit.add_port(bias_circuit_H,4); // port 4: sis4: H pol;
                                           // other sis on R circuit
  bias_circuit.add_port(bias_circuit_V,1); // port 5: sis5: V pol;
                                           // nearest L antenna
  bias_circuit.add_port(bias_circuit_V,2); // port 6: sis6: V pol;
                                           // other sis on L circuit
  bias_circuit.add_port(bias_circuit_V,3); // port 7: sis7: V pol;
                                           // nearest R antenna
  bias_circuit.add_port(bias_circuit_V,4); // port 8: sis8: V pol;
                                           // other sis on R circuit
  // the mixer
  mixer mix;
  mix.harmonics(HARMONICS);
  mix.add_junction(sis1).add_junction(sis2).add_junction(sis3).
  add_junction(sis4);
  mix.add_junction(sis5).add_junction(sis6).add_junction(sis7).
  add_junction(sis8);
  mix.set_LO(&LO_FREQ);
  mix.set_bias(bias_circuit).set_if(if_circuit).set_rf(rf_circuit);
  mix.set_balance_terminator(RF_terminator,rf_term_port);
  int rf_port = mix.port(rf_term_port,1);
  int if_port = mix.port(if_out,0);
```

Program listing for hc.cc – which is used to match hot-cold load data for the balanced mixer.

```
#define SPEC_FILE "balanced.h"
#include "supermix.h"
#include "materials.h"
#include SPEC_FILE
// offset errors in the measured iv data:
parameter i_offset = 0.0357*Micro*Amp;
parameter v_offset = 0.00722*mVolt;
main(int argc, char** argv)
{
#ifdef BALANCED
#  include "main.balanced.inc.cc"
#else
#  ifdef DUAL
#    include "main.dual.inc.cc"
#  else
#    include "main.basic.inc.cc"
#  endif
#endif
  // ************************************************************
  // try to generate a pumped IV and hot/cold load curves:
```

```
  IF_FREQ = 1.5*GHz;
  parameter Rho;
  gp.uf.rho_normal = &Rho; top.uf.rho_normal = &Rho;
  VGAP     = 2.69882*mVolt;
  Rn       = 11.7254*Ohm;
  Cj = 165*fFarad;
  LO_FREQ  = 525.812*GHz;
  LO_POWER = 367.003*Nano*Watt;
  MS_THICKNESS = 2425.18*Angstrom;
  Rho = 5.12688*Micro*Ohm*Centi*Meter;
  sio.eps = 5.68229;
  WINDOW_LOSS = 0.7;
  double power = LO_POWER;
  double hot = 300*Kelvin, cold = 80*Kelvin;
  for(double v = 0; v <= 8; v += .05) {
    VBIAS = v * mVolt;
    cout << VBIAS/mVolt;
    LO_POWER = 0.0;
    mix.balance();
    cout << "\t" << current()/(Micro*Amp);
    LO_POWER = power;
    mix.balance();
    cout << "\t" << current()/(Micro*Amp);
    LO_TEMP = cold;
    cout << "\t" << mix.get_term_data().C[if_port][if_port].
    real*(1000/205.9)/Kelvin;
    LO_TEMP = hot;
    cout << "\t" << mix.get_term_data().C[if_port][if_port].
    real*(1000/205.9)/Kelvin;
    cout << endl;
  }
}
```

References

[1] J. Ward, F. Rice, G. Chattopadhyay, and J. Zmuidzinas, "SuperMix: A Flexible Software Library for High-Frequency Circuit Simulation, Including SIS Mixers and Superconducting Elements," *Proceedings of the Tenth International Symposium on Space Terahertz Technology*, Charlottesville, Virginia, pp. 269–281, March 16–18, 1999.

[2] F. Rice, J. Ward, J. Zmuidzinas, and G. Chattopadhyay, "Fast Harmonic Balance of SIS Mixers with Multiple Junctions and Superconducting Circuits," *Proceedings of the Tenth International Symposium on Space Terahertz Technology*, Charlottesville, Virginia, pp. 282–297, March 16–18, 1999.

[3] J. R. Tucker, "Quantum limited detection in tunnel junction mixers," *IEEE J. Quantum Electron.*, vol. 15, pp. 1234–1258, November 1979.